

**Fast Prediction of Transonic Aeroelasticity
Using Computational Fluid Dynamics**
by
Mark Woodgate BSc.

A thesis submitted in partial
fulfillment of the requirements for
the degree of Doctor of Philosophy
University of Glasgow
Department of Aerospace Engineering
September 2008

© 2008
Mark Woodgate

Declaration

I hereby declare that this dissertation is a record of work carried out in the Department of Aerospace Engineering at the University of Glasgow during the period from October 1999 to September 2008. The dissertation is original in content except where otherwise indicated.

September 2008

.....

(Mark Andrew Woodgate)

Abstract

The exploitation of computational fluid dynamics for non linear aeroelastic simulations is mainly based on time domain simulations of the Euler and Navier-Stokes equations coupled with structural models. Current industrial practice relies heavily on linear methods which can lead to conservative design and flight envelope restrictions. The significant aeroelastic effects caused by nonlinear aerodynamics include the transonic flutter dip and limit cycle oscillations. An intensive research effort is underway to account for aerodynamic nonlinearity at a practical computational cost. To achieve this a large reduction in the numbers of degrees of freedoms is required and leads to the construction of reduced order models which provide compared with CFD simulations an accurate description of the dynamical system at much lower cost.

In this thesis we consider limit cycle oscillations as local bifurcations of equilibria which are associated with degenerate behaviour of a system of linearised aeroelastic equations. This extra information can be used to formulate a method for the augmented solve of the onset point of instability - the flutter point. This method contains all the fidelity of the original aeroelastic equations at much lower cost as the stability calculation has been reduced from multiple unsteady computations to a single steady state one. Once the flutter point has been found, the centre manifold theory is used to reduce the full order system to two degrees of freedom. The thesis describes three methods for finding stability boundaries, the calculation of a reduced order models for damping and for limit cycle oscillations predictions. Results are shown for aerofoils, and the AGARD, Goland, and a supercritical transport wing.

It is shown that the methods presented allow results comparable to the full order system predictions to be obtained with CPU time reductions of between one and three orders of magnitude.

Acknowledgements

I am grateful to BAE SYSTEMS, Engineering and Physical Sciences Research Council, MoD and DERA for funding this work as part of the programme of the Partnership for Unsteady Methods in Aerodynamics (PUMA) Defence and Aerospace Research Partnership (DARP).

I would like to thank my supervisor Professor Ken Badcock for this support, encouragement, guidance and patience over the past 8 years.

I would also like to thank all the members of the CFD Lab, past and present, for creating a stimulating working environment which is has been a privilege to work at over the years. I especially like to thank Professor Bryan Richards for this support during my early years at Glasgow University and Dr George Barakos for motivating me to get this work written up.

I am grateful to Professor Michael Henshaw and all the aerodynamicists at BAE SYSTEM Brough that made my years secondment there so productive and opened my eyes between practises used in the worlds of academia and business in the field of aeroelastics.

List of Most Relevant Publications

M.A. Woodgate and K.J. Badcock. Fast prediction of transonic aeroelastic stability and limit cycles. *AIAA Journal*, vol 45(6):1370-1381, 2007.

M.A. Woodgate and K.J. Badcock. A reduced order model for damping derived from CFD based aeroelastic simulations. In *47th AIAA/ASME/ASCE/AHS/ASC Structures, Structural Dynamics, and Materials Conference*, Newport, Rhode Island, 1-4 May 2006. AIAA-2006-2021.

K.J. Badcock and M.A. Woodgate. Aeroelastic damping model derived from discrete Euler equations. *AIAA Journal*, vol 44(11):2601-2611, 2006.

M.A. Woodgate, K.J. Badcock, A.M. Rampurawala, B.E. Richards, D. Nardini, and M.J. Henshaw. Aeroelastic calculations for the Hawk aircraft using the Euler equations. *Journal of Aircraft*, vol 42(4):1005-1012, 2005.

K.J. Badcock, M.A. Woodgate, and B.E. Richards. Direct aeroelastic bifurcation analysis of a symmetric wing based on the Euler equations. *Journal of Aircraft*, vol 42(3):731-737, 2005.

K.J. Badcock, M.A. Woodgate, and B.E. Richards. Hopf bifurcation calculations for a symmetric airfoil in transonic flow. *AIAA Journal*, vol 42(5):883-892, 2004.

G.S.L. Goura, K.J. Badcock, M.A. Woodgate, and B.E. Richards. Extrapolation effects on coupled computational fluid dynamics/computational structural dynamics simulations. *AIAA Journal*, vol 41(2):312-314, 2003.

G.S.L. Goura, K.J. Badcock, M.A. Woodgate, and B.E. Richards. Implicit method for the time marching analysis of flutter. *Aeronautical Journal*, vol 105:199-214, 2001.

G.S.L. Goura, K.J. Badcock, M.A. Woodgate, and B.E. Richards. Evaluation of methods for the time marching analysis of transonic aeroelasticity. In *19th AIAA Applied Aerodynamics Conference*, Anaheim, CA, 11-14 June 11-14 2001. AIAA-2001-2457.

K.J. Badcock, B.E. Richards, and M.A. Woodgate. Elements of computational fluid dynamics on block structured grids using implicit solvers. *Progress in Aerospace Sciences*, vol 36:351-392, 2000.

M.A. Woodgate, K.J. Badcock, B.E. Richards, and J. Anderson. Towards the direct calculation of non-linear transonic flutter characteristics. *RAeSoc Aerodynamics Conference 2000*, London, 17-18 April 2000.

Contents

Abstract	iii
Acknowledgements	iv
List of Most Relevant Publications	v
Table of Contents	vi
List of Figures	ix
List of Tables	xii
Nomenclature	xiii
1 Introduction	1
1.1 Aeroelastic Prediction	3
1.2 Computational Aeroelasticity	4
1.3 Reduced Order Modelling	7
1.3.1 The Eigenmode Methodology	7
1.3.2 Proper Orthogonal Decomposition	9
1.3.3 Harmonic Balance Method	11
1.4 Dynamical Systems Based Methods	13
1.4.1 Numerical Analysis of Bifurcations Points	13
1.4.2 Calculation of Bifurcation Points	14
1.4.3 Normal Forms for Bifurcations	15
1.5 Thesis Outline	15
2 Calculation of Hopf Bifurcation Points	17
2.1 Introduction	17
2.2 One Parameter Bifurcation Equilibria	18
2.3 Classes of Hopf Bifurcation	19
2.4 Numerical Methods for Calculating Equilibrium Solutions	22
2.4.1 Newton's Method	22
2.4.2 Relaxed Newton's Method	23
2.4.3 Modified Newton's Methods	23
2.5 Numerical Methods for Calculating Hopf Bifurcations	25
2.5.1 Indirect Calculation	25

2.5.2	Direct calculation	27
2.5.3	Evaluation	28
2.6	Model Problem	29
2.7	Conclusions	35
3	Model Reduction	36
3.1	Background	36
3.2	Centre Manifold Theorems	36
3.3	Change of Coordinates	38
3.4	Method of Projection	40
3.5	Centre manifolds with one parameter dependent systems	43
3.6	Computational Cost of the Method of Projection	44
3.7	Model Problem	45
3.8	Conclusions	46
4	Two Degree of Freedom Aeroelastic System	50
4.1	Aerodynamic and Structural Simulations	51
4.2	Formulation of Augmented System	53
4.3	Calculation of the Jacobian Matrix	55
4.4	Solution of the Linear System	58
4.5	Iteration scheme for flutter boundaries	62
4.6	Results for Symmetric Problem	65
4.7	Conclusions	68
5	Aeroelastic Stability Prediction for Wings	77
5.1	Introduction	77
5.2	Aerodynamic and Structural Simulations	77
5.2.1	Aerodynamics	77
5.2.2	Structural Dynamics, Inter-grid Transformation and Mesh Movement	78
5.3	Formulation of Augmented Solver	81
5.4	Results for Symmetric Problem	82
5.4.1	Test Case	82
5.4.2	Time Marching Solutions	83
5.4.3	Augmented Solver Results	85
5.5	Formulation of a Dedicated Linear Solver	86
5.5.1	Generalized Conjugate Residual	88
5.5.2	Block Incomplete Lower Upper Factorisation	89
5.5.3	Real and Complex Variable Formulations	90
5.5.4	Results	91
5.6	Symmetric case: AGARD Wing	93
5.7	Asymmetric case: MDO Wing	93
5.8	Conclusions	94

6	Prediction of Aeroelastic Limit Cycle Oscillations	108
6.1	Introduction	108
6.2	Model Reduction for LCO Calculation	109
6.3	Calculation of First, Second and Third Jacobians	111
6.4	Results	113
6.4.1	Evaluation of Cost	117
6.5	Conclusions	119
7	Conclusions	124
	References	126

List of Figures

1.1	Collar diagram - The aeroelastic triangle of forces	1
2.1	A supercritical Hopf bifurcation in the plane	21
2.2	A subcritical Hopf bifurcation in the plane	22
2.3	The grid convergence of the y solution with a first order treatment of the boundary condition at $x = 0$	31
2.4	The grid convergence of the y solution with a second order treat- ment of the boundary condition at $x = 0$	31
2.5	The equilibrium solution as mapped out by a continuation method varying the bifurcation parameter μ	32
2.6	The time history of Θ at $x = 1$ with $\mu = 0.1648$	32
2.7	The time history of Θ at $x = 1$ with $\mu = 0.1668$	33
2.8	Convergence of the Log of the residual against iteration number . .	34
2.9	Convergence of the bifurcation parameter against iteration number .	34
3.1	Comparison of the time history computed with full and reduced models of y at $x = 1$ with $\mu = 0.16508$ and an initial deflection of $\delta\Theta = 0.01$	45
3.2	Comparison of the time history computed with full and reduced models of y at $x = 1$ with $\mu = 0.16508$ and an initial deflection of $\delta\Theta = 0.001$	46
3.3	The correspondence of amplitudes for the full and reduced models. The comparison of time histories at point A is shown in Figure 3.4 and in Figure 3.5 for point B	47
3.4	Comparison of time histories close to the bifurcation point $\mu_0 +$ 0.00007	47
3.5	Comparison of time histories far from the bifurcation point $\mu_0 +$ 0.00075 . The full model was used to compute the solid line and the dot dashed line for the reduced model	48
3.6	Comparison of time histories close to the bifurcation point $\mu_0 +$ 0.00007	48
3.7	Comparison of time histories far from the bifurcation point $\mu_0 +$ 0.00075 . The full model was used to compute the solid line and the dot dashed line for the reduced model	49
4.1	Sparsity patterns for various orderings of the augmented matrix . . .	60
4.2	Convergence histories for TFQMR solution of augmented system using several preconditioning options	62

4.3	Comparison of convergence rate for retaining various combinations of $I\omega$ terms in augmented Jacobian matrix	65
4.4	Fine mesh for NACA0012 aerofoil	70
4.5	Comparison of pressure distribution for NACA0012 aerofoil at zero incidence and $M_\infty = 0.8$ on the coarse and fine grids	70
4.6	Eigenspectrum for quoted values of \bar{U} , the bifurcation parameter, on a very coarse grid at a Mach number of 0.5	71
4.7	Comparison of stability boundaries for the light case on the coarse and medium grids	72
4.8	Convergence at different Mach numbers for the light case on the medium grid	73
4.9	Comparison of stability boundary for the light case on the medium grids with time marching results	74
4.10	Comparison of stability boundaries for the heavy case on the coarse and medium grids	75
4.11	Comparison of stability boundary for the heavy case on the medium grids with time marching results	76
5.1	Grid topology (above) and medium surface mesh (below). Note that only the inner blocks above the wing are shown on the symmetry plane	96
5.2	The variation of flutter speed index with the structural damping applied at Mach 0.96. The line indicates the measurement	97
5.3	Comparison with measurements of the stability boundaries calculated on the medium grid using time marching and the bifurcation solver	98
5.4	The convergence of the bifurcation parameter with the bifurcation solver iteration number at Mach 0.96. The flutter speed index is shown against the right hand axes and the augmented residual against the left hand axes	99
5.5	Number of linear solver steps per bifurcation solver iteration. The solid line indicates the average number of steps for an aerofoil calculation	100
5.6	Comparison of the real and complex formulations for methods 1 and 2 with a modified order Jacobian	101
5.7	Comparison of the real and complex formulations for methods 1 and 2 with a second-order Jacobian	102
5.8	Comparison of complex formulations for all the methods with a second-order Jacobian	103
5.9	Convergence of flutter speed index for AGARD wing at Mach 0.97 .	104
5.10	Tracking of eigenvalues for AGARD wing at Mach 0.97. Each line corresponds to one aeroelastic mode and the symbols are consistent between the graphs for the real and imaginary parts	105

5.11	Tracking of eigenvalues for MDO wing with no initial aerostatic solution at Mach 0.85. Each line corresponds to one aeroelastic mode and the symbols are consistent between the graphs for the real and imaginary parts	106
5.12	Surface pressure distribution and tip aerofoil section for rigid and static deformed positions of MDO wing at Mach 0.85	107
6.1	Structural Modes for Goland wing.	114
6.2	Behaviour of the damping of modes 2 and 4 for Goland wing at Mach 0.92. Here dynamic pressure is in units of $kg/(msec^2)$	118
6.3	Convergence of bifurcation parameter for Goland wing at Mach 0.92.	119
6.4	Comparison between the full and reduced predictions of damping for Goland wing at Mach 0.92.	120
6.5	Comparison between the full and reduced predictions of LCO at 125% of the critical dynamic pressure for Goland wing at Mach 0.92. The symbols are from the simulation of the full system, and the lines are from the reduced model.	121
6.6	Growth of the LCO amplitude in the first and second modes at Mach 0.92 for the Goland wing. The filled squares are from the simulation of the full system, and the line is from the reduced model.	122
6.7	Response at extremes of the wing at 1.35 times the critical value of dynamic pressure using the reduced and full models. The undeflected tip position of the wing is indicated by the blue line joining 2 dots at the wing tip, and the surface contours shown are for change of pressure from the equilibrium value. These results are for the Goland wing at Mach 0.92.	123

List of Tables

2.1	Classification of two dimensional hyperbolic equilibrium points . . .	19
2.2	Grid convergence for the solution of the Augmented System	35
4.1	Structural model parameters	66
5.1	Grid Refinement Influence on Flutter Speed Index at Mach 0.96 . . .	87
5.2	Average calculation cost using the PMB code for the first two rows and the augmented solver for the bottom two rows in the table. The relative costs have been scaled by the time for a steady-state calculation with the appropriate code	87
5.3	Table of the number of non zero in the preconditioner for the modified order Jacobian	91
5.4	Table of the number of non zero in the preconditioner for the second order Jacobian	92
6.1	Convergence of reduced order model coefficient real parts under h refinement. The behaviour of the real and imaginary parts not shown is identical. Note that all columns include 2nd Jacobian-vector products except the column for G_{21} which contains a 3rd Jacobian-vector product. The abbreviations d-d and q-d stand for double-double and quad-double respectively	115
6.2	Summary of the costs expressed in multiples of the steady state solution.	119

Nomenclature

Acronyms	Definition
AIC(s)	Aerodynamic Influence Coefficient(s).
BEM	Boundary Element Method.
BILU(k)	k th Order block incomplete lower upper.
CAE	Computational Aeroelasticity.
CFD	Computational Fluid Dynamics.
CFD/CSD	(coupled) Computational Fluid Dynamics/Computational Structural Dynamics.
CGS	Conjugate Gradients Squared.
CPU	Central Processing Unit.
CSD	Computational Structural Dynamics.
DES	Detached Eddy Simulation.
DLM	Doublet-Lattice Method.
FEM	Finite Element Method.
GBU	Guided Bomb Unit.
GE	Gaussian Elimination.
GMRES	Generalized Minimal Residual.
HARV	High Angle of Attack Research Vehicle.
HB	Harmonic Balance.
HDHB	High Dimensional Harmonic Balance.
HOHB	High Order Harmonic Balance.
ILU	Incomplete Lower Upper.
LCOs	Limit Cycle Oscillations.

LES	Large Eddy Simulation.
LEX	Leading-Edge Extensions.
LU	Lower upper.
NLR	Nationaal Lucht- en Ruimtevaartlaboratorium (National Aerospace Laboratory of the Netherlands).
NS	Navier-Stokes (equations).
ODE	Ordinary differential equation.
PIDS	Pylon Internal Dispenser System.
PMB	Parallel Multiblock Code.
POD	Proper Orthogonal Decomposition.
RANS	Reynolds-averaged Navier-Stokes (equations).
RCM	Reverse Cuthill McGee.
ROM	Reduced Order Model.
TFQMR	Transpose Free Quasi Minimal Residual.
ZTAIC	ZAERO's Transonic Aerodynamic Influence Coefficients.

Symbols

Definition

\bar{U}	Reduced velocity = $\frac{V_\infty}{b\omega_\alpha}$.
\mathbf{w}	Solution vector.
\mathbb{C}	Set of complex numbers.
ω_α	Frequency of pitching.
ω_h	Frequency of plunging.
\mathbb{R}	Set of real numbers.
A	Jacobian matrix.
B	Second Jacobian matrix.
C	Third Jacobian matrix.
i	$i = \sqrt{-1}$.
M_∞	Mach number.

P	Matrix whose columns are the right eigenvectors of A .
Q	Matrix whose rows are the left eigenvectors of A .
q	Dynamic pressure = $\frac{1}{2}\rho V^2$.
R	Residual vector.
t	Time.
W^c	Centre manifold.
\mathbf{p}	$\mathbf{p} = \mathbf{p}_r + i\mathbf{p}_i$ The right eigenvector of a matrix.
\mathbf{q}	$\mathbf{q} = \mathbf{q}_r + i\mathbf{q}_i$ The left eigenvector of a matrix.

Greek Symbols

Λ	Eigenvalues of a matrix A .
λ_i	The i^{th} eigenvalue of the system.
μ	Bifurcation parameter.
ω	Frequency of the critical eigenvalue.

Subscripts

f	Fluid model.
i	Imaginary part of a complex number.
r	Real part of a complex number.
s	Structural model.
d	Dynamic solution.
qs	Quasi-steady solution.

Superscripts

\bar{z}	Complex conjugate.
n	Dimension of space.
T	Transpose.
t	Time level.

Definition

Definition

Definition

Chapter 1

Introduction

Aeroelasticity is the science concerned with the mutual interaction between inertial, elastic and aerodynamic forces^[1-3]. Static aeroelasticity arises from the interaction between the inertial and aerodynamic forces, while dynamic aeroelasticity comprises all three as shown in Figure 1.1 which is called the Collar diagram. The first

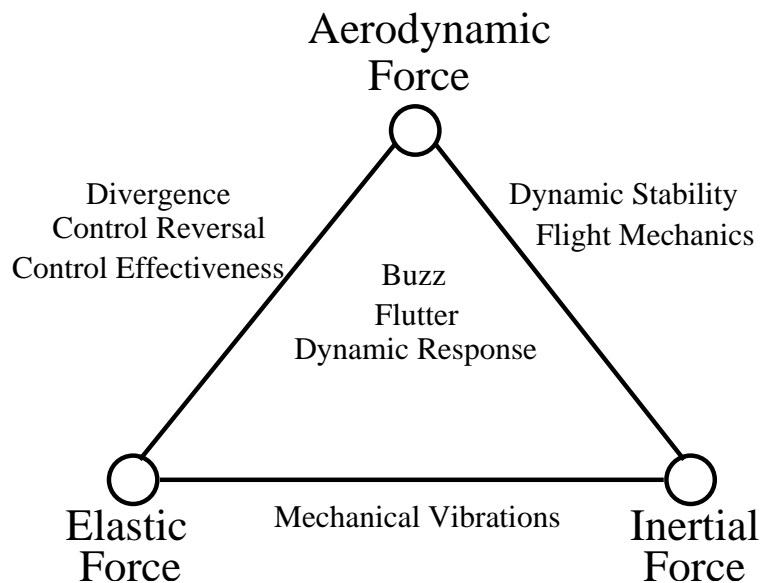


FIGURE 1.1: *Collar diagram - The aeroelastic triangle of forces*

recorded flutter incident was on a Handley Page O/400 twin engine biplane bomber in 1916^[4]. The flutter mechanism consisted of a coupling of the fuselage torsion mode with an antisymmetric elevator rotation mode. The elevators on this aeroplane were independently actuated and the solution was to interconnect them with a torque tube. Aeroelastic instability (flutter or divergence) can potentially lead to structural failure. This has led in the aircraft industry to the aeroelastic penalty.

Solutions to aeroelastic problems generally involve increasing the structural stiffness or mass balance, which increases weight while decreasing the performance. The development of aeroelasticity and its effect on design is described in the review articles^[5,6] with a survey of more recent applications given by Friedmann^[7], Bhatia^[8] and Livne^[9].

It is argued in Henshaw *et al.*^[10] that more sophisticated aeroelastic modelling and prediction will be required in the future compared with the linear methods used today. For example lighter and more structurally efficient designs will reduce stiffness increasing the chances of encountering aeroelastic phenomena. At present flight test programs are used to expand or contract the flight envelope. Problems identified this late in the development cycle may be very expensive to fix. Recently several incidents were reported of cracks in the tail section of the Guided Bomb Unit (GBU) 10 mounted on a Pylon Internal Dispenser System (PIDS) pylon on a F-16. The Royal Netherlands Air Force together with Air Force Seek Eagle Office and National Aerospace Laboratory NLR executed a flight test program to find the cause of the problem^[11] which turned out to be high vibration levels in the GBU 10 tail at transonic Mach numbers. The configurations were re-certified with limitations to minimise operation in the transonic regime while the manufacturer was informed of the finding in order to redesign the GBU 10 tail assembly. This is an examine of a limit cycle oscillation (LCO) which is a self sustaining limited amplitude oscillation produced by fluid structure interactions. Both the F-16^[12, 13] and F/A-18^[14] have encountered LCO at high subsonic and transonic speeds for store configurations with AIM-9 missiles on the wingtips and heavy stores on the outboard pylons.

It is clear that prediction of aeroelastic instability in the transonic regime plays an important role in the definition of the flight envelope for many high performance aircraft. Computational Fluid Dynamics (CFD) has matured to become an effective tool for simulating transonic aerodynamics. However, the use of multiple time domain calculations for each aircraft state is computationally expensive and provides limited insight into the dependence of the parameters on the type of response in the vicinity of the instability boundary. This is of particular importance when trying to reconcile anomalous aeroelastic bifurcation phenomena associated with aerodynamic nonlinearities. Consequently there is a need for a systematic and efficient methodology to predict flutter boundaries in the transonic regime, sub-

sequent LCO responses, and to relate design and operating parameter variations quantitatively to the response characteristics. The methods presented in this thesis are intended to address these points.

1.1 Aeroelastic Prediction

Since the 1950's^[1,2] aerodynamic strip theory was used in flutter predictions with corrections added to account for compressibility, aspect ratio effects and loss of lift at the wing tips^[15]. Aerodynamic strip theory assumes that the strips have no effect on each other, which is valid if the wing is thin and beam like. The inclusion of T-tails required a more advanced method and this was provided via panel methods^[16].

The doublet-lattice method (DLM) is a method for modelling the aerodynamics of oscillating lifting surfaces. The DLM reduces to the vortex-lattice method at zero reduced frequency. Since it is based on potential flow theory, the DLM cannot describe nonlinear compressible or viscous aerodynamic effects. Industrial flutter analysis^[10], using MSC NASTRAN for example, tends to use the DLM, and the linear predictions have been successful as part of an overall process for predicting flutter, despite the theoretical limitations. As such they provide an essential point of reference for more sophisticated methods, such as those based on the Euler equations. The output from the DLM is a set of aerodynamic influence coefficients (AICs). The structural model is determined using the finite element method (FEM) with a combination of beam and shell elements. The aerodynamic loads are then coupled to all the structural nodes via spline functions which interpolate the loads onto the structure.

To help improve the capability of the method in the transonic regime it is possible to correct the AICs with unsteady aerodynamic forces. The commercial package ZAERO has the non linear option ZTAIC^[17]. The transonic effects are included via a set of steady pressures supplied by the user. These pressures can be from experiments or CFD codes. These pressures are utilised to inverse design an aerofoil shape using the transonic small disturbance equation. The final aerofoil sections then match the user-supplied pressures. Unsteady pressure coefficients on the aerofoil section are then computed by solving the unsteady transonic small disturbance equation.

Linear methods have served the industry well over the last 50 years but they

cannot predict non-linear effects due to shock waves. As industry moves forward to increasingly lighter designs the risks of flutter and LCO's playing an important effect increases and this motivates the development of non-linear methods.

1.2 Computational Aeroelasticity

The term computational aeroelasticity (CAE) refers to the coupling of a computational fluid dynamics (CFD) method with a structural dynamics model to perform aeroelastic analysis [7]. The advances in CFD over the last 40 years are well documented. Usable models have increased in fidelity through the transonic small disturbance and full potential in the 1970's, Euler equations in the 1980's, Reynolds-averaged Navier-Stokes equations (RANS) in the 1990's and more recently to detached eddy simulations (DES) and large eddy simulation (LES). A review of the last 30 years in CFD can be found in Shang^[18].

A flutter boundary was obtained for the AGARD wing by solving the unsteady Euler equations of motion coupled to the normal modes of the structure in Lee-Rausch and Batina^[19,20]. The inclusion of viscous effects in the form of the thin layer approximation of the Navier-Stokes (NS) equations was made by the same authors^[21] and showed that the inclusion of the viscous terms improved the capture of the transonic dip. Liu *et al.*^[22] presented a coupled code for flutter calculations based on a parallel multiblock, multigrid flow solver for the NS equations. The solver was strongly coupled with the structural modal dynamics. This strong coupling allowed for a dual time stepping scheme to be used without a sequencing error. The cost of this type of time domain simulation is not prohibitive when the intention is to examine behaviour at previously identified problem conditions and there are several recent impressive demonstrations of this kind for complete F-16 aircraft configurations (e.g. Farhat *et al.*^[23] and Melville^[24]).

CAE has been used to examine a wide range of aeroelastic phenomena. Buffeting is an instability caused by vortical flow, separation, or shock motions from one part of the aircraft interacting with another part producing a random forced vibration. The F-18 high angle of attack research vehicle (HARV) uses wing leading-edge extensions (LEX) to generate vortices which increase wing lift and two vertical tail fins which interact with these vortices to enhance maneuverability. At high angles of attack the vortices break down before the tail fins resulting in tail fin

buffet^[25]. Gee *et al.* used RANS and an overset grid method to calculate the flow around the HARV at high angle of attack^[26]. Grid refinement around the fore-body and LEX region improved the prediction of vortex breakdown from previous work. Morton *et al.*^[27] used the commercial version of Cobalt with different turbulence models to predict the position of the vortex breakdown and examined the frequency content at points on the vertical tail. The choice of turbulence model is critical for the prediction of these types of flow with the DES version of Spalart-Almaras comparing well against the flight-test data. These works were carried out with rigid tail fins and hence no aeroelastic coupling was taken into consideration. Sheta^[28] used a multidisciplinary approach to solve the coupled aeroelastic problem to examine the effect of the LEX fences to alleviate tail fin buffet. RANS was used to solve the aerodynamic flowfield and the dynamical response of the tail fin was solved using a direct finite element analysis. The LEX fences shifted the onset of the maximum buffet condition to higher angles and the results compared well to both full scale wing tunnel experiments and flight tests.

Buzz is normally associated with an oscillating control surface in the presents of an oscillating shock. Transonic buzz responses were reported in flight tests on the T45 Goshawk trainer aircraft in the U.S.A.^[29] The oscillations were attributed to a shock induced instability and were removed via the use of 2 shock strips. Fuglsang *et al.*^[29] predicted the location of the shock on the vertical tail fin through steady-state NS calculations with the wings removed. Rampurawala^[30] carried out a detailed aeroelastic study of this case and found the inclusions of the wings weakened the shock on the vertical tail and hence reduced the buzz. Aileron buzz has also been simulated on the supersonic transport (SST) designed for the National Aerospace Laboratory of Japan. Yang *et al.* used the thin-layer Navier-Stokes equations coupled with the structural equations of motion expressed in modal form to examine the aileron behaviour of two different structural model. The SST structural model which was weakened by reducing the hinge stiffness exhibits aileron oscillations between Mach 0.98 and Mach 1.05.

Divergence is a static aeroelastic phenomena which occurs when the aerodynamic forces on the wing exceed the elastic restoring forces. Hollowell and Dugundjin investigated the effects of wing bending-torsion stiffness coupling on the divergence speed of unswept lifting surface in incompressible flow^[31]. The divergence speed was obtained from the V-g method^[1] when both the structural

damping and frequency abruptly go to zero. The results were in good agreement to low speed wind tunnel tests. They showed that wings with negative stiffness coupling exhibited divergence in the first bending mode. Balakrishnan^[32] presented an analytical solution to the transonic small disturbance potential equation with the Kutta-Joukowski boundary conditions for a zero thickness aerofoil at non-zero angle of attack. The resulting equation for the divergence speed showed explicitly a transonic dip dependant on the angle of attack.

If the flow about a lifting surface becomes partial or completely separated during any part of the periodic oscillation then the instability is called stall flutter. Stall flutter is normally associated with compressor cascades in turbojets and helicopter rotor blades. Datta and Chopra used a loosely coupled RANS code and structural model on a single UH-60A blade to show the first stall cycle was caused by high trim angles in the retreating blade while the second stall cycle was caused by the elastic twist^[33].

There has been recent interest in the LCO behaviour of wing store configurations. Store induced LCOs have been simulated for the rectangular Goland⁺ wing^[34,35]. The aeroelastic solver was developed by integrating a modal structural model from MSC/NASTRAN with the commercial CFD solver FLUENT. A spline matrix was used to transfer data from the non matching aerodynamic grid and structural grid. Store aerodynamics were found to affect the LCOs in two ways first by adding loads to the structure and secondly by interfering with the flow over the wing.

As a prelude to the work reported in this these, the parallel multiblock code^[36] (PMB) was extended to allow CAE computations. A number of considerations were required

- (a) The movement of the CFD grid by transfinite interpolation.^[19,37]
- (b) Sequencing in time between the CFD/CSD solutions.^[38,39]
- (c) The intergrid transfer of data.^[40,41]

Time domain flutter predictions have been obtained with PMB for problems ranging from model wings^[42] to in production aircraft^[43].

Time-domain methods are general and have been shown to accurately predict non linear effects. Despite the significant gains in algorithm efficiency and raw computing power, which has reduced the computational cost of time response calculations of complete aircraft down to a few hours^[43], they remain too costly for

routine prediction of flutter boundaries and LCO amplitude prediction. Multiple calculations must be undertaken across the flight envelope to find the flutter point and the LCO behaviour. This has motivated a research effort to search for methods which account for nonlinear effects but at a much reduced computational cost.

1.3 Reduced Order Modelling

Reduced order model (ROM) or low dimensional approximations to a large system of equations greatly reduces both the central processing unit (CPU) cost and storage requirements of aeroelastic calculations. These models are vital for parametric studies, optimisation of structures and control problems. However, to be useful, they must be capable of reproducing the important linear and non-linear behaviour of the full system.

There are two approaches to model reduction. System identification methods take the response of the system to inputs and use this information to build a low order model. The second method is to manipulate the full order system to reduce the cost of calculations. In this thesis the second class of method will be considered. More comprehensively, the review papers of Dowell and Hall^[44] and Lucia, Beran and Silva^[45] examine a number of techniques which include proper orthogonal decomposition (POD), Volterra series, the harmonic balance method, and an eigenmode method.

1.3.1 The Eigenmode Methodology

Hall^[46] constructed ROM's using an unsteady vortex lattice method which assumes the flow to be incompressible, inviscid and irrotational. Consider the iterative scheme

$$Aw^{t+1} + Bw^t = R^{t+1} \quad (1.1)$$

where w is the solution, t is the time level and R is the residual. Consider the homogeneous part of (1.1) then the generalised eigenvalue problem is

$$A\Lambda + B\Lambda = 0 \quad (1.2)$$

where Λ is a diagonal matrix of order N containing the eigenvalues and P is an $N \times N$ matrix whose columns are the right eigenvectors. Analogously

$$A^T Q\Lambda + B^T Q = 0 \quad (1.3)$$

where Q is a $N \times N$ matrix whose rows are the left eigenvectors. These eigenvectors can be scaled to satisfy the following orthogonality conditions

$$Q^T AP = I, \quad Q^T BP + \Lambda = 0. \quad (1.4)$$

Then the dynamic behaviour of the system can be determined by using the mode superposition method by representing the response as the sum of all the eigenvectors

$$w = Pc \quad (1.5)$$

where c is the vector of normal mode coordinates for the eigenmodes. Substituting equation (1.5) into (1.1) and using the orthogonality conditions equation (1.4) yields N uncoupled equations

$$c^{t+1} - \Lambda c^t = Q^T R^{t+1}. \quad (1.6)$$

The ROM is now constructed by keeping only a few of the original modes. A static correction technique is often required to improve the ROM to give satisfactory results^[46,47].

Static correction is applied by decomposing the unsteady solution into the response of the system if the disturbance is quasi-steady, and the dynamic part

$$w^t = w_{qs}^t + w_d^t = w_{qs}^t + P\hat{c}^t. \quad (1.7)$$

The quasi-steady part w_{qs}^t is given by

$$(A + B)w_{qs}^t = R^t \quad (1.8)$$

and hence the corrected ROM is

$$\hat{c}^{t+1} - \Lambda \hat{c}^t = Q^T R^{t+1} - Q^T (Aw_{qs}^{t+1} + Bw_{qs}^t). \quad (1.9)$$

Hall used this model on a rectangular wing of aspect ratio 5 to reduce the number of degrees of freedom from 480 to 40. He showed that without the static correction 40 modes is not adequate to capture the behaviour at high reduced frequencies. For fluid models where the dimension of the eigenvalue matrix is of the order 10^4 it is possible to use a standard eigensolver package to obtain the eigenvalues. Romanowski and Dowell^[48], applied this ROM to subsonic unsteady flows around the NACA 0012 aerofoil, based on the Euler equations. The eigenvalue problem was solved using the Lanczos method^[49]. It has been shown that the existence of zero eigenvalues in the eigensystem is the main reason for needing to apply

a static correction technique. Hence Shahverdi *et al.* [50] constructed a reduced-order model based only on the wake eigenmodes with, the body quasi-static eigenmodes removed. They applied this technique for unsteady flow computations based on the boundary element method (BEM). When the Prandtl-Glauert compressibility correction is used to consider linear compressibility effects the results were in good agreement to the Euler solutions^[48].

This methodology cannot easily be extended to the three dimensional Euler equations since it is very expensive to calculate eigenvalues when the order of the matrix is above 10^4 .

1.3.2 Proper Orthogonal Decomposition

Proper orthogonal decomposition (POD) is a modal method applicable to systems for which multiple measurements are simultaneously available. Early application was to the analysis of experimental data with a view to extracting trends and dominant features^[51]. In the aeroelastic context POD is applied to a matrix of multiple measurement locations sampled through time. POD can help determine the number of active modes in an oscillatory system and can be used as an optimal representation of the form of the modes and hence is used to construct reduced order models^[52]. This method has been successfully applied to a wide range of problems including complete aircraft configurations^[53,54].

A POD basis, $\Phi = [e_1, e_2, e_3, \dots, e_j]$ is orthogonal and can be used in a modal decomposition

$$w(t) \approx W_0 + \sum_{j=1}^M \hat{w}_j(t) e_j = W_0 + \Phi \hat{w}(t) \quad (1.10)$$

where \hat{w} is the vector of modal amplitudes, W_0 is some baseline solution and M is the number of modes.

For dynamical problems the POD modes are constructed by first computing a number of snapshots of the full order system response in time,

$$S = [W^1, W^2, W^3, \dots, W^n] \quad (1.11)$$

A new basis is formed from the linear transformation of the snapshot matrix S

$$\Phi = SV \quad (1.12)$$

and maximising the projection of the snapshot matrix onto the POD basis yields the following eigenvalue problem

$$S^T S V = V \Lambda. \quad (1.13)$$

The eigenvalues satisfy $\lambda_i \geq 0$ since $S^T S$ is symmetric positive semi-definite. The eigenvectors V are normalised so that $V^T V = I$, and then scaling e_i by $\lambda_i^{-1/2}$ gives an orthonormal set of modes, i.e. $\Phi^T \Phi = I$.

In practise fewer than M modes are retained. This is done by limiting the set to only the eigenvectors corresponding to sufficiently large eigenvalues. A property of this decomposition is that it minimises the approximation error when a member of the class S is approximated through a linear projection onto M basis vectors^[51].

There are a number of different techniques for obtaining a set of reduced order equations for $w(t)$ with different projections. These have recently been reviewed in Lucia *et al.* ^[45]. The data samples for a POD are collected over a small region of state space, this focused sampling allows for very accurate ROM at the training point. However a ROM is not usually robust with respect to changes in the model parameter^[55]. Ideally the ROM should be reconstructed whenever the model parameter is changed. To avoid this CPU intensive effect recently ROM adaptation techniques have been used. There are at least 4 different techniques used in aerospace problems:

(1) The global POD (GPOD)^[56] which has only been demonstrated to be effective at low free stream Mach numbers.

(2) The method of direct interpolation of the reduced order basis vectors^[57] which has delivered poor results in the transonic regime because the vectors vary non linearly with Mach number and angle of attack.

(3) The subspace angle interpolation^[57,58] adapts two ROMs associated with two different sets of model parameters to a third set by interpolating between the basis rather than the vectors of the basis. Lieu showed that the principal angles between subspaces of 2 ROMs appear to vary linearly for subsonic Mach numbers for intervals of 0.2 of a Mach number, this interval is halved in the transonic regime. Hence the adapted ROMs do a reasonable job of predicting transonic flow if there is enough ROMs throughout the Mach number range.

(4) The final interpolation method based on the Grassmann manifold, its tangent space at a point and the computation of geodesic paths ^[59]. The Grassmann manifold $\mathcal{G}(k, n)$ is a space which parameterises all linear k -dimensional subspaces

of an n -dimensional vector space i.e. $\mathcal{G}(2,3)$ is the space of all planes that pass through the origin. The last two methods are closely linked as a two point Grassmann manifold corresponds to a subspace angle interpolation.

The generation of the training data is still costly as unsteady CFD computations must be undertaken. More importantly it is also very difficult to produce a ROM and at present there are no POD aeroelastic results for viscous full order models.

1.3.3 Harmonic Balance Method

The formulation of the harmonic balance (HB) method of Hall *et al.* ^[60], yields an efficient method for the calculation of time periodic solutions of large non linear systems of equations. The semi-discrete form of the system of ordinary differential equations is

$$I(t) = \frac{dw(t)}{dt} + R(t) = 0. \quad (1.14)$$

Assume that the solution and residual are periodic in time with frequency ω . Then they can be expanded in a Fourier series which is truncated to N_H terms as

$$w(t) \approx \hat{w}_0 + \sum_{n=1}^{N_H} (\hat{w}_{a_n} \cos(\omega n t) + \hat{w}_{b_n} \sin(\omega n t)) \quad (1.15)$$

$$R(t) \approx \hat{R}_0 + \sum_{n=1}^{N_H} (\hat{R}_{a_n} \cos(\omega n t) + \hat{R}_{b_n} \sin(\omega n t)) \quad (1.16)$$

The expansions (1.15) and (1.16) are then substituted into the the original governing equations (1.14) to give a system of equations for the unknown harmonic terms,

$$\begin{aligned} \hat{R}_0 &= 0 \\ \omega n \hat{w}_{b_n} + \hat{R}_{a_n} &= 0 \\ -\omega n \hat{w}_{a_n} + \hat{R}_{b_n} &= 0 \end{aligned} \quad (1.17)$$

The difficulty in solving the system of equations (1.17) is in finding a relationship between the solution and residual in the frequency domain. To avoid this problem the system is converted back into the time domain. The solution is split into $2N_H + 1$ discrete equally spaced sub-intervals

$$\mathbf{W} = \begin{pmatrix} w(t_0 + \Delta t) \\ w(t_0 + 2\Delta t) \\ \vdots \\ w(t_0 + T) \end{pmatrix} \quad \mathbf{R} = \begin{pmatrix} R(t_0 + \Delta t) \\ R(t_0 + 2\Delta t) \\ \vdots \\ R(t_0 + T) \end{pmatrix} \quad (1.18)$$

where $\Delta t = 2\pi/(\omega(2N_H + 1))$. There exists a transformation matrix E such that

$$\hat{\mathbf{W}} = E\mathbf{W} \quad \text{and} \quad \hat{\mathbf{R}} = E\mathbf{R}. \quad (1.19)$$

and then the system of equations (1.17) can be written as

$$\omega D\mathbf{W} + \mathbf{R} = \mathbf{0} \quad (1.20)$$

where D is a $2N_H + 1 \times 2N_H + 1$ matrix of the form

$$D_{i,j} = \frac{2}{2N_H + 1} \sum_{k=1}^{N_H} k \sin(2\pi k(j-i)/(2N_H + 1)) \quad (1.21)$$

The standard pseudo-time steady-state approach to solving the HB equation (1.20) can be applied. So, in effect, by using the truncated periodic solution the unsteady problem has been converted into a $2N + 1$ steady state problem. Good results have been claimed with even a small number of modes when modelling the LCO behaviour of the F-16^[61]. This method is closely related to the non-linear frequency domain methods of McMullen *et al.* ^[62,63]. They employ a very similar approach but solve the system of equations (1.17) in the frequency domain. Assuming \hat{W} is known, the time domain solution can be constructed. The steady-state residual operator R is then applied to each of these time instances and these are converted back into the frequency domain via a fast Fourier transform. McMullen *et al.* also derive a gradient approach for the class of problems where the time period is not known a priori^[63]. An iterative approach is used which adjusts the time period at each iteration by using the derivate of the square of the residual in the frequency domain with respect to T as the correction.

Two HB formulations have been analysed in detail for Duffing's oscillator in Liu *et al.* ^[64], the formulation by Hall was denoted as the high-dimensional harmonic balance (HDHB) method due to its applicability for high-dimensional dynamical systems. It was shown that the HDHB system always contains more terms than the classical HB system for the same number of harmonics. These extra terms have the effect of producing non physical solutions and may increase the number of harmonics required for a given accuracy. Maple *et al.* introduced an adaptive harmonic balance^[65,66] to reduce the computational cost further. Each cell was examined to see what fraction of spectral energy contained in the highest computed Fourier frequency and refined if they exceed a threshold value. It was shown to

work well for supersonic/subsonic diverging nozzle where the periodic solution is mostly continuous and low frequency but with a shocked region.

The cost of mapping a stability boundary by the HB could be substantial. If it is not known a priori which modes interact, then there is no estimate of what frequency ω is required in (1.15) and (1.16). So a number of calculations will be required to explore the frequency domain. A flow containing highly non-linear features that need to be resolved accurately, e.g. shocks, will require a large number of modes for each calculation at added further computational cost.

1.4 Dynamical Systems Based Methods

In CAE the partial differential equations are turned into a system of ordinary differential equations, making it logical to appeal to dynamical systems theory in order to calculate flutter boundaries and predict LCOs. The goal of this thesis is to take these standard ideas and turn them into practical methods that can be used to solve large aeroelastic systems.

1.4.1 Numerical Analysis of Bifurcations Points

Bifurcation theory is the study of changes in the qualitative behaviour or topological structure of a given problem. A bifurcation occurs when a small smooth change in a parameter(s) leads to a sudden topological change in system behaviour. Given a set of ordinary differential equations depending on a set of parameters the idea is to obtain its bifurcation diagram. These diagrams divide the parameter space into regions within which the system has topologically equivalent behaviour. Dynamic pressure vs Mach number and flutter speed index vs Mach number are two common diagrams in aeroelastics. These regions for aeroelastic systems include: stable - all modes are damped, unstable - there is at least one divergent mode, or LCOs. All these regions have been shown on the rectangular Goland wing model with tip store^[67]. For a fixed Mach number as the velocity is increased the wing passes from being stable to being unstable at around 650 ft/sec. However between Mach 0.92 and Mach 0.94 there is a small pocket of LCOs at a velocity of 450 ft/sec. Mapping the boundaries where the system flips from one region to another is important. Other information of interest is how fast the modes are damped in the

stable regions and the amplitude of any LCOs. All these questions can be answered with time marching CAE, but at the expense of significant computer time.

1.4.2 Calculation of Bifurcation Points

The first part of mapping out the behaviour of a system of ODEs is to calculate the equilibrium points where the system switches behaviour. Consider the system of non-linear ordinary differential equations

$$\dot{\mathbf{x}} = f(\mathbf{x}, \mu) \quad \mathbf{x} \in \mathbb{R}^n \quad \mu \in \mathbb{R} \quad (1.22)$$

where μ is the bifurcation parameter. The equilibrium points of equation (1.22) satisfies

$$f(\mathbf{x}, \mu) = 0. \quad (1.23)$$

The system switching behaviour is characterised by a change in the eigenvalues of the Jacobian matrix

$$A = f_{\mathbf{x}}(\mathbf{x}, \mu). \quad (1.24)$$

For example if all the eigenvalues of A have negative real part then the equilibrium point is stable. In the case of a simple LCO the Jacobian matrix has a complex pair of eigenvalues values $\lambda = \lambda_r + i\lambda_i$ with $\lambda_r > 0$ and $\lambda_i \neq 0$ with all other eigenvalues having negative real part. The boundary for the change in behaviour between a stable equilibrium point and an LCO is when a complex pair of eigenvalues crosses the real axis. This bifurcation point is called a Hopf bifurcation. Seydel^[68] divided methods for locating bifurcation points into two classes indirect and direct methods. For indirect methods a bifurcation point is calculated by solving equation (1.23) repeatedly for different values of μ and detecting a change of sign of a test function which classifies the bifurcation point. For the Hopf bifurcation one possible test is to calculate all the eigenvalues of (1.24) and see when one pair crosses the real axis^[68]. When the crossing has been detected the secant method can be used to solve for the real part of λ is zero^[69]. The direct methods solve the system of equations (1.23) augmented by additional equations that characterise the bifurcation point. Roose^[70] proposed a direct method for the computation of Hopf bifurcations which was to solve a augmented system of dimension $2n + 2$. Griewank and Reddien^[71] developed a similar method which solves a system of dimension $3n + 2$. Holdniok and Kubiček^[72] compared 4 different methods two of

which required the evaluation of the coefficients of the characteristic polynomial of the Jacobian matrix.

1.4.3 Normal Forms for Bifurcations

The normal form of a bifurcation is a simplified system of equations that approximates the dynamics of the system in the vicinity of a bifurcation point. The simplification can be obtained by using a number of methods, i.e. centre manifold reduction^[73], the Lyapunov-Schmidt method^[74] and the method of multiple scales^[75,76]. The dimension of the normal form is generally much lower than the dimension of the full system of equations. For a Hopf bifurcation the normal form is a two-dimensional system.^[77] Dessi and Mastroddi^[78] have used the method of multiple scales to examine a three degree of freedom airfoil flap configuration with two non-linear torsional springs (cubic) in two-dimensional incompressible flow. Vio *et al.*^[79] applied a number of bifurcation analysis techniques to the transverse galloping of a square sectioned beam in a normal steady flow. The aerodynamic force was expressed as a seventh order polynomial function of velocity and the structure as a mass with linear stiffness and non-linear damping. The methods used in the study included centre manifold^[80], normal form^[81], numerical continuation^[82] and higher order harmonic balance^[83] (HOHB). Only two of the methods examined, namely HOHB and Numerical continuation were able to fully and accurately characterise the problem.

1.5 Thesis Outline

This thesis is concerned with the development of fast methods for the prediction of flutter boundaries and LCO responses in transonic flow. To this end the Euler equations are used to capture the changing behaviour of shocks in response to the motion of the aircraft. An a priori assumption is made on the dynamics of the flutter, namely that it is a Hopf Bifurcation which signals a change from stable steady motion to periodic motion.

Chapter 2 summarises the theory of Hopf bifurcations and methods that can detect when such a bifurcation has been encountered. The formulation is extended and used to calculate the value of a single parameter for which an eigenvalue of the

system Jacobian matrix crosses the imaginary axis. The chapter concludes with a model example of a 1D tubular reactor.

Whilst knowledge of the onset of the instability is important more information is required in practice. For example the fast comparison of predictions and flight test damping data is required to inform decisions about future test points during flight testing. If the stability boundary is crossed in flight, knowledge of the LCO amplitude is required. Chapter 3 contains the theory of centre manifold projections and highlights some of the difficulties involved in using such a method when the system of equations is of the order 10^6 . The chapter concludes again with a model example of a 1D tubular reactor.

In chapter 4 the method outlined in chapter 2 is developed into a scheme that is applicable to the two dimensional Euler equations coupled with a pitch-plunge dynamics model. The method shows a two orders of magnitude reduction in CPU time to calculate a flutter boundary compared with time-marching.

Chapter 5 takes the method of chapter 4 and demonstrates it on three dimensional test cases. It is shown that the method has reached a sufficient level of maturity that it has been used on real aircraft problems within the research activities of industry^[10].

In chapter 6 the theory outlined in chapter 3 is turned into a practical method for calculating the damping and limit cycle oscillations for wings. The method uses information obtained from the approach of chapter 5 to reduce the system of equations down to 2 degrees of freedom. This allows for near instantaneous calculation of LCO responses once the model is formed.

The methods presented in chapters 4-6 provide a unique and powerful set of tools for exploiting the modelling capability of CAE. An important feature of the work is the demonstration of the methods that can be applied to problems of realistic size. These methods have all been published in journal papers listed at the start of the thesis.

Chapter 2

Calculation of Hopf Bifurcation Points

2.1 Introduction

Recent studies by Morton and Beran^[84,85] suggest that, for a large class of transonic aeroelastic problems, a more direct evaluation of the critical stability boundary is feasible, based on numerical path following techniques^[68] and the augmented system of Griewank and Reddien^[71]. Here, the parameterised aeroelastic equations of motion are expressed notionally in semi-discrete form. Local bifurcations of equilibria are associated with degenerate behaviour of the linearised aeroelastic equations in which one or more of the eigenvalues of the Jacobian matrix (1.24) has zero real part. For example, the onset of LCO, at which a steady-state solution transitions to an oscillatory solution with zero amplitude under the influence of a single parameter, can be identified with a simple Hopf bifurcation in which the Jacobian matrix possesses a conjugate pair of pure imaginary eigenvalues with non-zero frequency. These are the critical eigenvalues.

Under the variation of multiple parameters, more complex degeneracies are possible. The degree of degeneracy (or co-dimension) of a critical point is defined by the minimum number of parameters required to fully explore the qualitatively distinct solution behaviour in the vicinity of the critical point. Numerical path following (continuation) techniques enable particular degeneracies of steady state solutions of prescribed co-dimension to be tracked with respect to the free-stream and structural parameters, thereby identifying directly critical stability boundaries

in parameter space. From a knowledge of the type of degeneracy at criticality it is possible to infer qualitatively generic local bifurcation characteristics^[86]. In addition, the critical eigensolutions associated with the degenerate Jacobian matrix are automatically determined as an integral part of the procedure, thereby providing insight into the composition of the critical aeroelastic modes. This modal information also forms the basis of quantitative model reduction procedures^[87] which can be used to explore sub- and post-critical behaviour in the neighbourhood of the critical bifurcation parameters.

Of practical importance, direct path-following methods generally demand less computational effort than existing time-integration procedures for the evaluation of stability boundaries whilst offering additional information in the sub- and post-critical aeroelastic behaviour over a range of parameters in the vicinity of criticality. The approach operates directly on the semi-discrete CFD/CSD representation of the aeroelastic system. Moreover, the direct approach is not limited to the prediction of simple nonlinear flutter phenomena but can incorporate aeroelastic behaviour associated with higher-order degeneracies and multiple critical eigenvalues such as the double Hopf bifurcation which has been observed on a single degree of freedom bluff body with a tuned mass damper^[88].

2.2 One Parameter Bifurcation Equilibria

Consider a continuous time system depending on a parameter μ

$$\dot{\mathbf{w}} = f(\mathbf{w}, \mu), \quad \mathbf{w} \in \mathbb{R}^n, \quad \mu \in \mathbb{R}, \quad (2.1)$$

where f is smooth with respect to both \mathbf{w} and μ . The eigenvalues of the Jacobian matrix $\partial f / \partial \mathbf{w}$, are important for determining the stability characteristics of the equilibria of the system. Let $\mathbf{x} = \mathbf{x}_0$ be a hyperbolic equilibrium¹ point of the system for $\mu = \mu_0$. Consider the two dimensional $n = 2$ system then the Jacobian matrix has either two real eigenvalues λ_1 and λ_2 or one complex conjugate pair $\lambda_{1,2} = \lambda_r \pm i\lambda_i$. There are 3 topological classes of hyperbolic equilibrium for this system,^[87] namely nodes, saddles and foci. These are distinguished by the positive and negative real parts of the eigenvalues, see Table 2.1.

¹ i.e. there are no eigenvalues of $\partial \mathbf{f} / \partial \mathbf{w}$ on the imaginary axis

Real/Complex	Eigenvalues	Class	Stability
Real	$\lambda_1 \leq \lambda_2 < 0$	Node	stable
Real	$0 < \lambda_1 \leq \lambda_2$	Node	unstable
Real	$\lambda_1 < 0 < \lambda_2$	Saddle	unstable
Complex	$\lambda_r < 0$	Focus	stable
Complex	$\lambda_r > 0$	Focus	unstable

TABLE 2.1: Classification of two dimensional hyperbolic equilibrium points

There are only two ways in which the hyperbolicity condition can be violated. Either a simple real eigenvalue approaches zero hence $\lambda_1 = 0$, or a pair of simple complex eigenvalues reach the imaginary axis and $\lambda_{1,2} = \pm i\omega_0$, $\omega_0 > 0$ for some value of the parameter. It can be shown that more than one parameter is required to allocate extra eigenvalues on the imaginary axis.^[87]

For one parameter bifurcations only two of these types are possible. The first is called a fold and is associated with the appearance of a zero eigenvalue. This is also referred to as a limit point or a turning point. The one-dimensional system

$$f(w, \mu) = \mu + w^2$$

is the simplest possible system that has an equilibrium point at $(0, 0)$ and satisfies the fold bifurcation condition $f_x(0, 0) = 0$. The second type is the Hopf bifurcation which is associated with the appearance of a purely imaginary eigenvalue.

2.3 Classes of Hopf Bifurcation

Consider the following system of two differential equations depending on one parameter μ

$$\begin{aligned} \dot{w}_1 &= \mu w_1 - w_2 - w_1(w_1^2 + w_2^2), \\ \dot{w}_2 &= w_1 + \mu w_2 - w_2(w_1^2 + w_2^2). \end{aligned} \tag{2.2}$$

This system is the simplest possible that exhibits a Hopf bifurcation. This system has the equilibrium $w_1 = w_2 = 0$ for all μ with the Jacobian matrix

$$A = \begin{pmatrix} \mu & -1 \\ 1 & \mu \end{pmatrix}$$

having eigenvalues $\lambda_{1,2} = \mu \pm i$. If the complex variable $z = w_1 + iw_2$ is introduced, then the complex conjugate is given by $\bar{z} = w_1 - iw_2$, and the magnitude $|z|^2 = z\bar{z} = x_1^2 + x_2^2$. This variable satisfies the differential equation

$$\dot{z} = \dot{w}_1 + i\dot{w}_2 = \mu(w_1 + iw_2) + i(w_1 + iw_2) - (w_1 + iw_2)(w_1^2 + w_2^2),$$

and equation (2.2) can be rewritten in the complex form

$$\dot{z} = (\mu + i)z - z|z|^2.$$

With the change of variable $z = re^{i\theta}$ then

$$\dot{z} = \dot{r}e^{i\theta} + ri\dot{\theta}e^{i\theta} = re^{i\theta}(\mu + i - r^2).$$

which gives the *polar* form of equation (2.2).

$$\begin{aligned} \dot{r} &= r(\mu - r^2) \\ \dot{\theta} &= 1. \end{aligned} \tag{2.3}$$

Bifurcations of the phase portrait of the system as μ passes through zero can easily be analysed using this polar form since the equations for r and θ decouple. Since $r \geq 0$ the first equation has the equilibrium point $r = 0$ for all values of μ . The equilibrium is linearly stable if $\mu < 0$, nonlinearly stable for $\mu = 0$, and linearly unstable for $\mu > 0$. There is an additional stable point $r_0(\mu) = \sqrt{\mu}$ for $\mu > 0$. The second equation describes a rotation with constant speed. Taking these two pieces of information the following description of the bifurcation behaviour can be obtained.

The behaviour of the system can be seen in Figure 2.1. The system always has an equilibrium point at the origin. This is a stable focus for $\mu < 0$ and an unstable focus for $\mu > 0$. At the critical value of $\mu = 0$ the equilibrium is nonlinearly stable and topologically equivalent to the focus. This equilibrium at the origin is surrounded by an isolated closed orbit (*limit cycle*) that is unique and stable if $\mu > 0$. The cycle is a circle of radius $r_0(\mu) = \sqrt{\mu}$. All orbits starting outside or inside the circle (with the exception of the origin) tend to this cycle as $t \rightarrow +\infty$. There is a Hopf bifurcation at $\mu = 0$.

A system having nonlinear terms with the opposite sign to equation (2.2)

$$\begin{aligned} \dot{w}_1 &= \mu w_1 - w_2 + w_1(w_1^2 + w_2^2), \\ \dot{w}_2 &= w_1 + \mu w_2 + w_2(w_1^2 + w_2^2) \end{aligned} \tag{2.4}$$

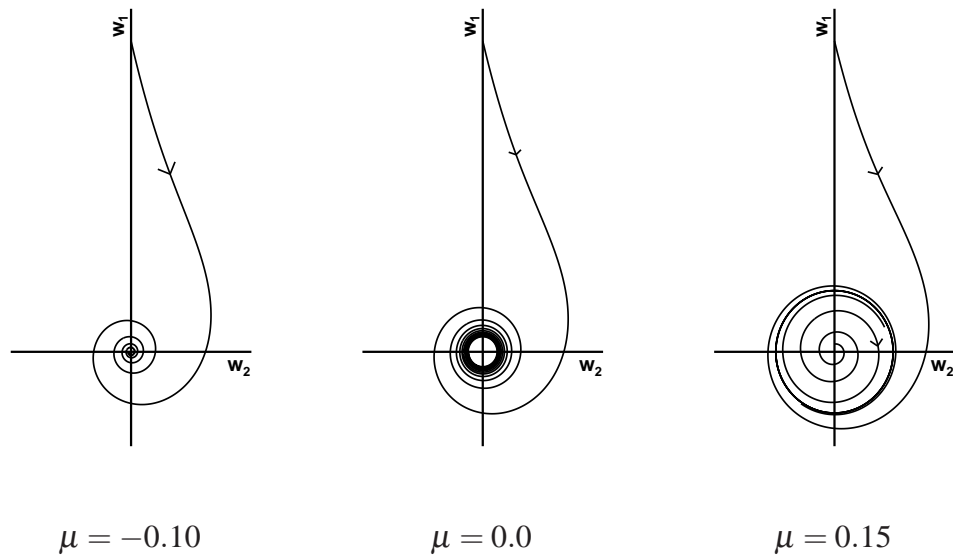


FIGURE 2.1: A supercritical Hopf bifurcation in the plane

has the following complex form

$$\dot{z} = (\mu + i)z + z|z|^2.$$

which can be analysed as above. The system passes through a Hopf bifurcation at $\mu = 0$. Since the nonlinear terms are of opposite sign to equation (2.2) there is an unstable limit cycle in equation (2.4) as can be seen in Figure 2.2.

There are two types of Hopf bifurcation. The bifurcation in system (2.2) is called a supercritical bifurcation because a stable equilibrium exists before bifurcation and a stable limit cycle after. The bifurcation in system (2.4) is called a subcritical bifurcation because an unstable limit cycle exists before the bifurcation and an unstable equilibrium solution after.

If higher order terms are added to equation (2.2) and written in a vector form then

$$\begin{pmatrix} \dot{w}_1 \\ \dot{w}_2 \end{pmatrix} = \begin{pmatrix} \mu & -1 \\ 1 & \mu \end{pmatrix} \begin{pmatrix} w_1 \\ w_2 \end{pmatrix} - (w_1^2 + w_2^2) \begin{pmatrix} w_1 \\ w_2 \end{pmatrix} + \mathcal{O}(\|\mathbf{w}\|^4) \quad (2.5)$$

where $\mathbf{w} = (w_1, w_2)^T$, $\|\mathbf{w}\|^2 = w_1^2 + w_2^2$, and $\mathcal{O}(\|\mathbf{w}\|^4)$ terms can smoothly depend on μ . The system (2.5) is locally topologically equivalent near the origin to system (2.2) and the higher order terms do not effect the bifurcation behaviour of the system.

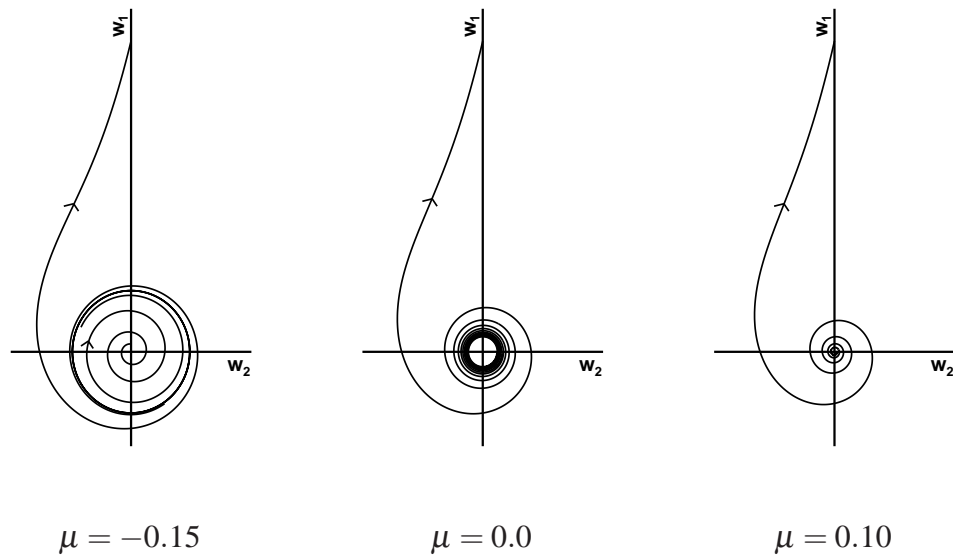


FIGURE 2.2: A subcritical Hopf bifurcation in the plane

2.4 Numerical Methods for Calculating Equilibrium Solutions

The calculation of an equilibrium solution requires the solution of a nonlinear system of algebraic equations (2.1) for a given μ . An attractive method for achieving this is Newton's method, or a variant. For clarity μ has been dropped in the methods are outlined below.

2.4.1 Newton's Method

Let $A(\mathbf{w}) = \partial f / \partial \mathbf{w}$ denote the Jacobian matrix of f evaluated at a point \mathbf{w} . Suppose \mathbf{w}^t is the current approximation to the solution of equation (2.1). If we linearise the left hand side of equation (2.1) near \mathbf{w}^t then

$$f(\mathbf{w}^t) + A(\mathbf{w}^t)(\mathbf{w}^{t+1} - \mathbf{w}^t) \approx 0.$$

If the matrix $A(\mathbf{w}^t)$ is invertible this linear system will have the solution

$$\mathbf{w}^{t+1} = \mathbf{w}^t - A^{-1}(\mathbf{w}^t)f(\mathbf{w}^t), \quad (2.6)$$

which should be closer to \mathbf{w}_0 than \mathbf{w}^t . Let \mathbf{w}^0 be a given initial point near the equilibrium point \mathbf{w} . Then Newton's iteration is defined by the recurrence relation

(2.6). It should be noted that matrix $A(\mathbf{w}^t)$ need not be inverted to compute \mathbf{w}^{t+1} but equation (2.6) must be solved. If the Jacobian has a special structure, for example sparse, it is very useful to take this into account.

Suppose the system (2.1) is smooth and has an equilibrium \mathbf{w}_0 at which no eigenvalue is zero in the Jacobian matrix. Then there is a neighbourhood \mathcal{W} of \mathbf{w}_0 so that the Newton iterations converge to \mathbf{w}_0 from any initial point $\mathbf{w}^0 \in \mathcal{W}$ and

$$\|\mathbf{w}^{t+1} - \mathbf{w}_0\| \leq \kappa_0 \|\mathbf{w}^t - \mathbf{w}_0\|^2, \quad t = 0, 1, 2, \dots \quad (2.7)$$

for some $\kappa_0 > 0$. A practical method is however needed to obtain an initial guess which is within \mathcal{W} . The convergence of this method is independent of the stability of the equilibrium since the no zero eigenvalues in the Jacobian matrix is equivalent to equation (2.6) having a solution. The estimate above means that the error is approximately squared from one iteration to the next, giving the famous quadratic convergence.

2.4.2 Relaxed Newton's Method

Newton's method requires that the initial guess \mathbf{w}^0 is close, in some sense, to the equilibrium solution \mathbf{w}_0 . Newton's method can be modified to increase this domain of convergence at the expense of reducing the rate of convergence by adding a time-like term onto the diagonal of the Jacobian matrix so that

$$\left(\frac{1}{\Delta T}I + A(\mathbf{w}^t)\right)(\mathbf{w}^{t+1} - \mathbf{w}^t) = -f(\mathbf{w}^t). \quad (2.8)$$

The term ΔT can be a physical time step or can be adjusted locally to accelerate convergence. As the time step is increased the pure Newton's method, and quadratic convergence, is recovered.

2.4.3 Modified Newton's Methods

If no analytical formula for the Jacobian matrix is available then an expensive evaluation by numerical differentiation is required. Some approximations may be possible to reduce the required cost, as for example is done in some CFD codes^[89].

One possible simplification is to freeze the Jacobian matrix at the initial value. This is called the Newton chord method. This simple idea gives rise to the iteration

$$\mathbf{w}^{t+1} = \mathbf{w}^t + \delta \mathbf{w}^t, \quad t = 0, 1, 2, 3, \dots$$

where $\delta \mathbf{w}^t$ is now given by

$$A(\mathbf{w}^0)\delta \mathbf{w}^t = -f(\mathbf{w}^t). \quad (2.9)$$

This also converges to \mathbf{w}_0 but at a rate given by

$$\|\mathbf{w}^{t+1} - \mathbf{w}_0\| \leq \kappa_1 \|\mathbf{w}^t - \mathbf{w}_0\|, \quad t = 0, 1, 2, \dots \quad (2.10)$$

for some $0 < \kappa_1 < 1$. Hence the convergence is only linear.^[90]

The Broyden^[91] update is a member of a family of methods which use rank one updates, that is $A^{t+1} - A^t$ is a matrix of only one linearly independent row. The idea is that two successive iterates and the corresponding function values are used to update the matrix involved in the computation of $\delta \mathbf{w}$. Broyden's method is a generalisation of the secant method when applied to the Jacobian matrix A

$$A^{t+1}(\mathbf{w}^{t+1} - \mathbf{w}^t) \approx F(\mathbf{w}^{t+1}) - F(\mathbf{w}^t). \quad (2.11)$$

Unless the dimension of \mathbf{w} is one this equation is under determined. Broyden suggested using a rank one update of A^t to calculate A^{t+1}

$$A^{t+1} = A^t + \mathbf{u}\mathbf{v}^T \quad (2.12)$$

where $\mathbf{u}, \mathbf{v} \in \mathbb{R}^n$. Requiring that $A^{t+1}\mathbf{r} = A^t\mathbf{r}$ for all \mathbf{r} orthogonal to $\mathbf{w}^{t+1} - \mathbf{w}^t$ and using equation (2.11) implies

$$\mathbf{v} = \mathbf{w}^{t+1} - \mathbf{w}^t \quad \mathbf{u} = \frac{F(\mathbf{w}^{t+1}) - F(\mathbf{w}^t) - A^t(\mathbf{w}^{t+1} - \mathbf{w}^t)}{(\mathbf{w}^{t+1} - \mathbf{w}^t) \cdot (\mathbf{w}^{t+1} - \mathbf{w}^t)}.$$

This gives rise to the following algorithm, starting with an initial guess \mathbf{w}^0 and an estimate of the Jacobian matrix A^0 then

$$\begin{aligned} \mathbf{w}^{t+1} &= \mathbf{w}^t - (A^t)^{-1}F(\mathbf{w}^t) \\ \mathbf{s}^t &= \mathbf{w}^{t+1} - \mathbf{w}^t \\ \mathbf{y}^t &= F(\mathbf{w}^{t+1}) - F(\mathbf{w}^t) \\ A^{t+1} &= A^t + \frac{(\mathbf{y}^t - A^t\mathbf{s}^t)(\mathbf{s}^t)^T}{\mathbf{s}^t \cdot \mathbf{s}^t} \end{aligned}$$

for $t = 1, 2, 3, \dots$. Better convergence than the Newton chord method is obtained^[92] but there is no expectation that A^t converges to the Jacobian matrix $A(\mathbf{w}_0)$ at the equilibrium point \mathbf{w}_0 , even if the method converges to \mathbf{w}_0 as $t \rightarrow \infty$. Hence, the final matrix cannot be used to compute, say, the eigenvalues of A at \mathbf{w}_0 . Normally the Jacobian matrix $A(\mathbf{w})$ has a special structure (for CFD methods, this is banded and sparse) and this is always used to allow efficient linear solution. However the rank one update of Broyden's method may not preserve this structure.

2.5 Numerical Methods for Calculating Hopf Bifurcations

Consider the continuous time system (2.1) depending upon one parameter μ . An equilibrium solution satisfies

$$f(\mathbf{w}, \mu) = 0. \quad (2.13)$$

At the critical value μ_0 of the parameter μ there is a Hopf bifurcation if the following conditions are satisfied.^[93] The Jacobian matrix $f_{\mathbf{w}}(\mathbf{w}_0, \mu_0)$ has a simple pair of purely imaginary eigenvalues $\pm i\omega$ while all other eigenvalues have non zero real part. And for $\mu \approx \mu_0$ then the critical eigenvalue $\lambda = \lambda_r \pm i\omega$ have a non zero speed crossing the imaginary axis.

2.5.1 Indirect Calculation

Seydel^[68] classes the indirect approach of locating bifurcation points of equation (2.1) as the tracing out the solutions of (2.13) as the parameter μ varies and to detect where the stability changes. The sequence of solutions pairs (\mathbf{w}^t, μ^t) take the form

$$f(\mathbf{w}^t, \mu^0 + t * \Delta\mu) = 0 \quad t = 0, 1, 2, 3, \dots \quad (2.14)$$

For the detection of the Hopf bifurcation point, a test function $\gamma(\mathbf{w}, \mu)$ is defined which has regular zeros at the bifurcation points.

A natural choice for the test function γ is the maximum of all real parts of the eigenvalues of the Jacobian A , denoted by λ_k :

$$\gamma := \max \{ \text{Re}(\lambda_1), \dots, \text{Re}(\lambda_n) \}. \quad (2.15)$$

This choice has the advantage of being physically meaningful because $\gamma < 0$ guarantees local stability and continuity provided $f(\mathbf{w}, \mu)$ is continuously differentiable. During the computation of the sequence (2.14) γ is calculated. There is unlikely to be a solution pair such that $\gamma(\mathbf{w}^t, \mu^t) = 0$ so a change of sign between these points

$$\gamma(\mathbf{w}^t, \mu^t) \gamma(\mathbf{w}^{t+1}, \mu^t) < 0$$

is monitored instead. The point can be located more accurately by applying Newton's method to the system

$$\begin{cases} f(\mathbf{w}, \mu) = 0 \\ \gamma(\mathbf{w}, \mu) = 0 \end{cases} \quad (2.16)$$

To apply a Newton-like method the test function γ has to be defined and differentiable in the neighbourhood of the curve. If the system given in equation (2.16) is singular then another method must be used to find the solution. Hassard^[94] located Hopf points by solving by the secant method for the eigenvalue of smallest real part.

The calculation of this test function is non-trivial. First there is a concern about how the eigenvalues are influenced by the accuracy of the evaluation of the Jacobian matrix. The Jacobian can possibly be calculated by first order approximations^[89] or numerical differentiation as a practical alternative to analytical evaluation. The question for a detection method is how useful are the eigenvalues of an approximate Jacobian to f_w . They might be expected to be reasonable except where stability is lost, where the real part of the critical eigenvalue is close to zero and the relative error possibly high.

A critical part of a detection method based on this choice of test function is the evaluation of the eigenvalues of the Jacobian matrix. Methods based on QR factorisation,^[49] which calculate all the eigenvalues of a matrix, have a cost which grows like $O(n^3)$ and so will be too expensive for the current application. However the QR method gives much more information than is required. In the current case only the sign of the eigenvalue with maximum real part is needed. This can be obtained from the inverse power method.^[49] This strategy needs an initialisation for the first solution but more importantly a test is required to make sure the eigenvalue is indeed the one with maximum real part. This is different from calculating the eigenvalue of largest or smallest magnitude, which is commonly done. There is a way around this problem by means of a generalised Cayley transform^[49] on the Jacobian matrix A .

$$C := (A - a_1 I)^{-1} (A - a_2 I) \quad (2.17)$$

for real a_1 and a_2 . By this transformation the eigenvalues of A are mapped to the eigenvalues of C . The eigenvalue of A which is dominant in real part, denoted λ , can be calculated from the eigenvalue of C which is dominant in magnitude, denoted θ , from

$$\mu = \frac{a_1 \theta - a_2}{\theta - 1}. \quad (2.18)$$

2.5.2 Direct calculation

Griewank and Reddien^[71] proposed the following direct method for the calculation of Hopf bifurcations which is also the third algorithm used in Holdniok and Kubiček comparative numerical study^[72].

For λ to be an eigenvalue of the Jacobian matrix A then the following equations is valid

$$A\mathbf{p} = \lambda\mathbf{p}. \quad (2.19)$$

where $\mathbf{p} = \mathbf{p}_r + i\mathbf{p}_i$ is the right eigenvector. A Hopf bifurcation with respect to the parameter μ occurs when $A(\mathbf{w}_0, \mu)$ has one pair of eigenvalues of the form $\pm i\omega$ then equation (2.19) reduces to

$$A\mathbf{p} = i\omega\mathbf{p}. \quad (2.20)$$

One possible normalisation to make the eigenvector \mathbf{p} unique is as follows, choose a constant real vector $\mathbf{s} \in \mathbb{R}^n$ so that

$$\mathbf{s}^T \mathbf{p}_r = 0 \quad \mathbf{s}^T \mathbf{p}_i = 1. \quad (2.21)$$

Taking real and imaginary parts of equation (2.20)

$$\begin{aligned} A\mathbf{p}_r &= -\omega\mathbf{p}_i \\ A\mathbf{p}_i &= \omega\mathbf{p}_r \end{aligned} \quad (2.22)$$

A Hopf bifurcation point can be calculated directly by solving equations (2.13) (2.22) and (2.21) together

$$F_A = \begin{bmatrix} f \\ A\mathbf{p}_r + \omega\mathbf{p}_i \\ A\mathbf{p}_i - \omega\mathbf{p}_r \\ \mathbf{s}^T \mathbf{p}_r \\ \mathbf{s}^T \mathbf{p}_i - 1 \end{bmatrix} = 0 \quad \mathbf{W}_A = [\mathbf{w}, \mathbf{p}_r, \mathbf{p}_i, \mu, \omega]^T. \quad (2.23)$$

This system will be referred to as the **augmented system** throughout this thesis. This method is also used in the code Auto97².

Holdniok and Kubiček^[72] suggested that the dimensionality of the augmented system (2.23) can be reduced from $(3n + 2)$ to $(2n + 2)$ by noting the following: if

² Auto is the standard bifurcation and continuation package. The latest version of Auto and can be found at <http://indy.cs.concordia.ca/auto/>

ω is non-zero \mathbf{p}_r and \mathbf{p}_i are linearly independent. The matrix A^2 has a double real eigenvalue $\lambda = -\omega^2$ with a two dimensional eigenspace spanned by $\{\mathbf{p}_r, \mathbf{p}_i\}$ at the Hopf point. Taking a vector $\mathbf{r} \notin \{\mathbf{p}_r, \mathbf{p}_i\}$, there exists $\mathbf{S} \in \text{span}\{\mathbf{p}_r, \mathbf{p}_i\}$ with $\|\mathbf{S}\| = 1$ and orthogonal to \mathbf{r} . The augmented system then becomes

$$F_A = \begin{bmatrix} f \\ A^2\mathbf{S} + \omega^2\mathbf{S} \\ \mathbf{S}^T\mathbf{S} - 1 \\ \mathbf{r}^T\mathbf{S} \end{bmatrix} = 0 \quad \mathbf{W}_A = [\mathbf{w}, \mathbf{S}, \mu, \omega]^T.$$

This system is one third of the size of the original augmented system but is likely to suffer from ill-conditioning since the condition number of the new system will be the square of the original system.

The augmented system (2.23) can be solved by applying Newton's method with a Newton update given by

$$\frac{\partial F_A}{\partial \mathbf{W}_A} \Delta \mathbf{W}_A = -F_A(\mathbf{W}_A^t) \quad (2.24)$$

where $\Delta \mathbf{W}_A = \mathbf{W}_A^{t+1} - \mathbf{W}_A^t$. The Jacobian matrix on the left hand side of equation (2.24) is given in expanded form as

$$\frac{\partial F_A}{\partial \mathbf{W}_A} = \begin{bmatrix} A & 0 & 0 & f_\mu & 0 \\ A_{\mathbf{w}}\mathbf{p}_r & A & I\omega & A_\mu\mathbf{p}_r & \mathbf{p}_i \\ A_{\mathbf{w}}\mathbf{p}_i & -I\omega & A & A_\mu\mathbf{p}_i & -\mathbf{p}_r \\ 0 & \mathbf{s}^T & 0 & 0 & 0 \\ 0 & 0 & \mathbf{s}^T & 0 & 0 \end{bmatrix}. \quad (2.25)$$

The function F has $3n + 2$ unknowns if \mathbf{w} has dimension n which is the same as the number of equations in (2.25). Hence equation (2.24) is closed.

2.5.3 Evaluation

In both of the alternative methods the solution of large nonlinear systems of equations is required. The augmented system is significantly larger than systems arising in CFD calculations. The indirect method relies on the calculation of the eigenvalue of largest real part for large matrices. It is potentially an easier task to solve the larger systems arising from the augmented system than to reliably calculate the required eigenvalue for detection. Therefore the current work will focus on the

direct solution of the augmented system. This decision defines the numerical problems which must be overcome. First, the Jacobian matrix of the must be calculated exactly since it is included in F of the augmented system (2.23). Secondly, the second Jacobian matrix A_w must be at least approximated if the iteration (2.24) is used. Finally, the resulting linear system must be solved efficiently. These issues, for aeroelastic systems, are the central challenges of this work.

2.6 Model Problem

To test the solution methodology for the augmented system and its solution via (2.24), a model problem is considered which describes the unsteady behaviour of a non-adiabatic tubular reactor with axial mixing ^[95–97]

$$\begin{aligned}\frac{\partial y}{\partial t} &= \frac{1}{Pe_m} \frac{\partial^2 y}{\partial x^2} - \frac{\partial y}{\partial x} - \mu y \exp\left(\Gamma - \frac{\Gamma}{\Theta}\right) \\ \frac{\partial \Theta}{\partial t} &= \frac{1}{Pe_h} \frac{\partial^2 \Theta}{\partial x^2} - \frac{\partial \Theta}{\partial x} - \beta(\Theta - \bar{\Theta}) \\ &\quad + \mu \alpha y \exp\left(\Gamma - \frac{\Gamma}{\Theta}\right)\end{aligned}\tag{2.26}$$

where Pe_m , Pe_h , β , α , Γ , and $\bar{\Theta}$ are fixed constants and μ is the bifurcation parameter. The boundary conditions ($t > 0$) are given by

$$\frac{\partial y}{\partial x} = Pe_m(y - 1) \quad \frac{\partial \Theta}{\partial x} = Pe_m(\Theta - 1) \quad (x = 0)$$

$$\frac{\partial y}{\partial x} = \frac{\partial \Theta}{\partial x} = 0 \quad (x = 1)$$

For the results presented here the constants are set to $Pe_m = 5$, $Pe_h = 5$, $\beta = 2.5$, $\alpha = 0.5$, $\Gamma = 25$, and $\bar{\Theta} = 1.0$.

The system is discretised using a cell centred finite difference scheme so that the first and second differences are approximated by

$$\frac{\partial^2 y}{\partial x^2} \Big|_i = \frac{y_{i+1} - 2y_i + y_{i-1}}{h^2} \quad \frac{\partial y}{\partial x} \Big|_i = \frac{y_{i+1} - y_{i-1}}{2h}.$$

Here a uniform mesh of spacing h is used with the i -th point at $x_i = ih$ for ($i = 0, \dots, n$). The boundary conditions for $x = 1$ are applied by setting halo cell values to be identical to the values in the adjacent interior cell. There are three possibilities for applying the condition at $x = 0$.

First there is the first order approximation $y_b = y_0$ which leads to

$$y_{-1} = y_0 - hPe_m(y_0 - 1) \quad \frac{\partial y_{-1}}{\partial y_0} = 1 - hPe_m \quad (2.27)$$

$$\frac{\partial y_{-1}}{\partial y_1} = 0.$$

The first of the two second order approximations is $y_b = (y_0 + y_{-1})/2$ which leads to

$$y_{-1} = \frac{y_0(2 - hPe_m) + 2hPe_m}{2 + hPe_m} \quad \frac{\partial y_{-1}}{\partial y_0} = \frac{2 - hPe_m}{2 + hPe_m} \quad (2.28)$$

$$\frac{\partial y_{-1}}{\partial y_1} = 0.$$

The alternative second order approximation is $y_b = (3y_0 - y_1)/2$ which leads to an extra term being added into the Jacobian matrix

$$y_{-1} = y_0 - \frac{hPe_m}{2}[3y_0 - y_1 - 2] \quad \frac{\partial y_{-1}}{\partial y_0} = 1 - \frac{3hPe_m}{2} \quad (2.29)$$

$$\frac{\partial y_{-1}}{\partial y_1} = \frac{hPe_m}{2}.$$

For this problem having the first order boundary condition greatly effects the accuracy of the results so that even a grid with 512 cells does not give a grid converged answer, as shown in figures 2.3 and 2.4.

The solution of equation (2.27) is by the full Newton method with the use of the exact Jacobian on the left-hand side. For the continuation problem (2.14) this is solved using a banded LU decomposition. For the solution of the augmented system (2.23), since the bandwidth has grown to nearly the width of the full matrix, a full LU decomposition is used. It is possible to use a direct solver for the linear system since the dimension is small in the model problem.

To check these results, unsteady time stepping is also considered. An explicit method is used which results in a large number of time steps ($\Delta t = 1/500$ is required for stability). The bifurcation point is bracketed between a stable solution at one parameter value and an unstable solution at a second value. Each new calculation halves the length of the region bracketing the bifurcation value. This method however does not give the eigenvalue and eigenvector causing the instability as part of the solution. This information is found as part of the solution of the augmented system.

The rich solution space for this model problem is shown in figure 2.5. This includes stable and unstable equilibria, limit points and Hopf bifurcation points.

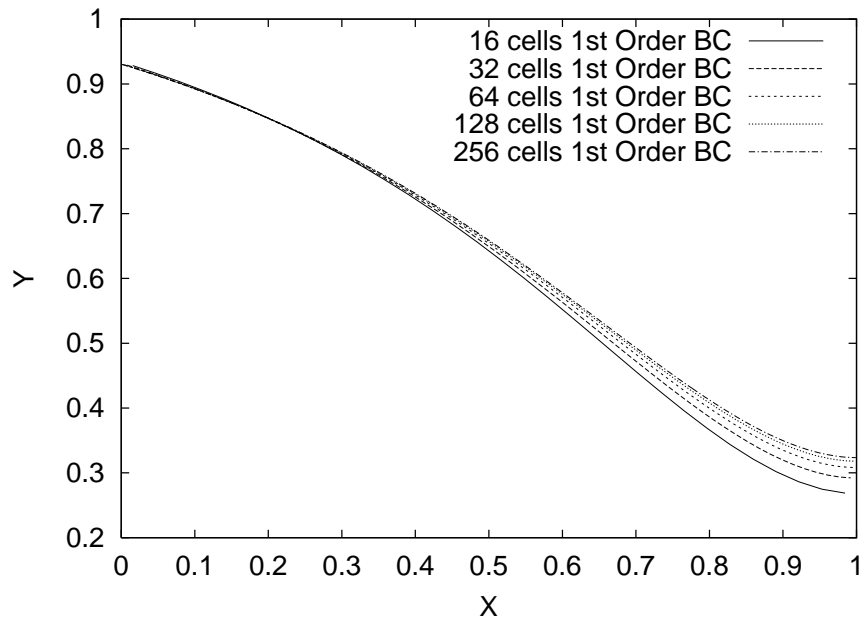


FIGURE 2.3: The grid convergence of the y solution with a first order treatment of the boundary condition at $x = 0$

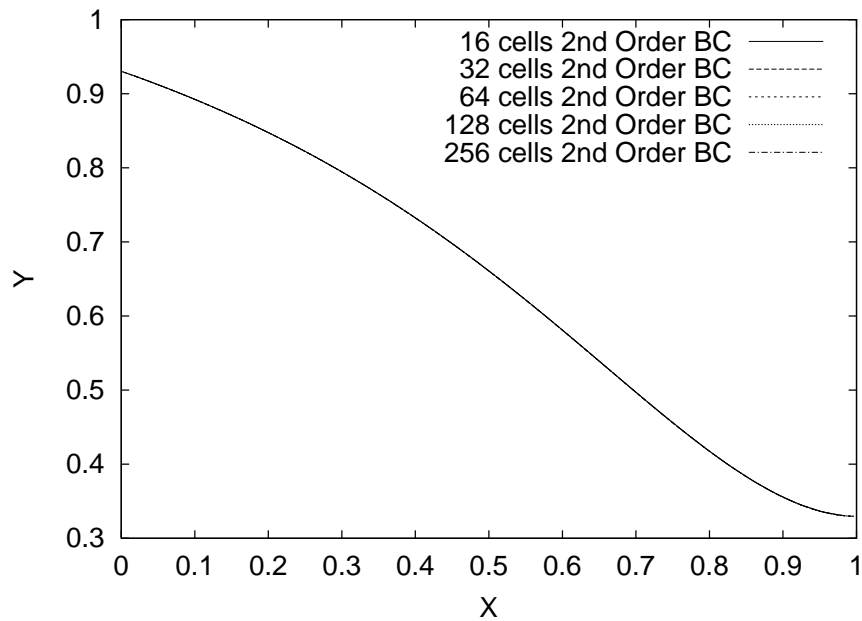


FIGURE 2.4: The grid convergence of the y solution with a second order treatment of the boundary condition at $x = 0$

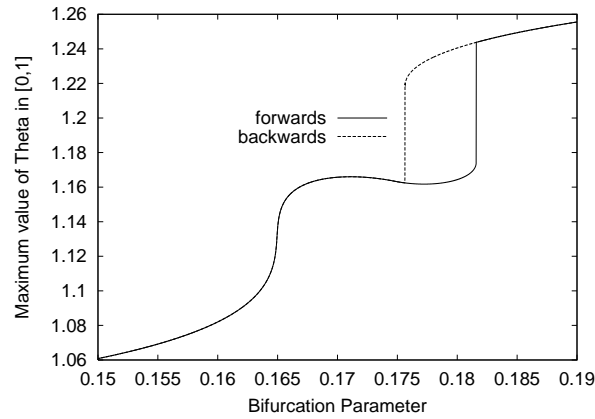


FIGURE 2.5: The equilibrium solution as mapped out by a continuation method varying the bifurcation parameter μ

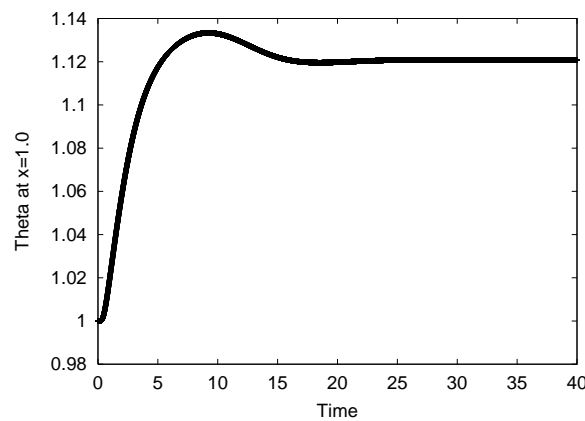


FIGURE 2.6: The time history of Θ at $x = 1$ with $\mu = 0.1648$

There is also a hysteresis loop for increasing and decreasing μ . The solution is characterised by the maximum value of Θ within the domain. The equilibrium solutions for varying μ are shown in figure 2.5. For values of $\mu < 0.165$ and $\mu > 0.180$ this equilibrium is stable and the solution to equation (2.27) is steady. For values of μ in between these extremes the equilibrium is unstable and a limit cycle oscillation is formed. Depending on whether the parameter μ is increased (solid line) or decreased (solid and dashed lines) a different equilibrium is obtained, indicating hysteresis. The equilibria were mapped out using the continuation method with Newton's method for the corrector stage. In addition, time marching calculations were done to map out the stability of these equilibria. The time history for Θ at $x = 1$ is shown in figures 2.6 and 2.7 for $\mu = 0.1648$ and $\mu = 0.1668$ respectively. It is clearly seen that the solution is steady in the first case and oscillates in the second.

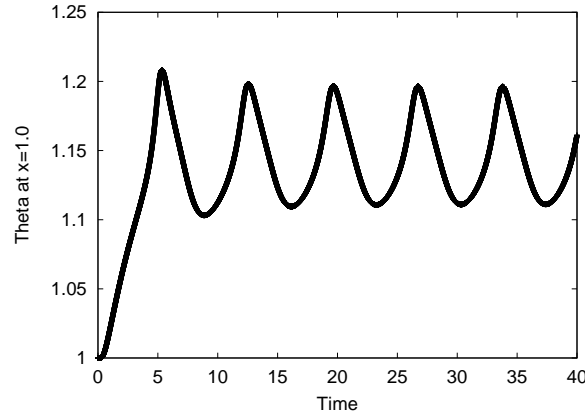


FIGURE 2.7: The time history of Θ at $x = 1$ with $\mu = 0.1668$

Next, the augmented system was solved to find the bifurcation points. If the initial guess is poor then the solution diverges. For the current calculations the following initial guess was used: $\mu = 0.16$, $x_{2k} = 1.0$, $x_{2k+1} = 0.0$, $\mathbf{p}_{r_i} = \sqrt{N}$, $\mathbf{p}_{i_{2k}} = \sqrt{N}$, $\mathbf{p}_{i_{2k+1}} = -\sqrt{N}$, $\mathbf{s} = \mathbf{p}_i$ and N is the number of cells in the mesh. By changing the initial conditions the Newton iterations can be made to converge to the second Hopf point at $\mu = 0.1796$. Starting from this guess the iterations had to be under-relaxed by a factor 0.5 until the domain of quadratic convergence was reached (the criteria used was based on the initial residual being reduced by half). A sequence of grids was used to show mesh independence and a second method of initialisation was used taking the final solution from the previous grid in the sequence as the starting solution on the next grid. No relaxation was required using this technique.

The convergence of the bifurcation parameter is shown in table 2.2. The number of Newton iterations required with and without the grid sequencing to initialise the iteration is given in the fourth and sixth columns. The sequenced start-up is obviously very beneficial in reducing the cost of the calculation. From the convergence plots shown in figures 2.8 and 2.9 for the residual and bifurcation value of μ respectively it is clear that the Newton iterations take a while to reach the domain of quadratic convergence when not using the sequenced start-up. However, once the quadratic region is reached the convergence is rapid. The CPU times shown in the fifth column of the table scale with N^3 since a full Gaussian elimination was used on the full matrix for this test problem. The exact Jacobian matrix of the augmented system has a large bandwidth.

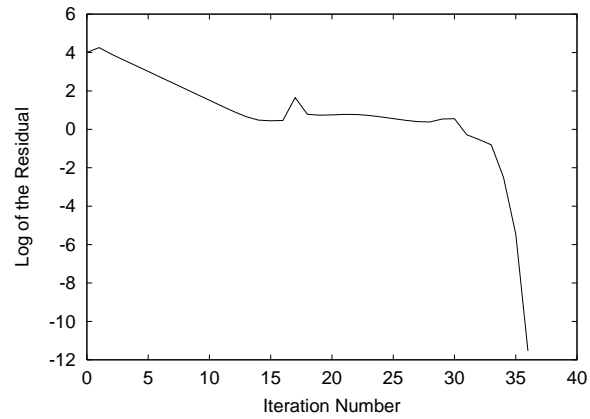
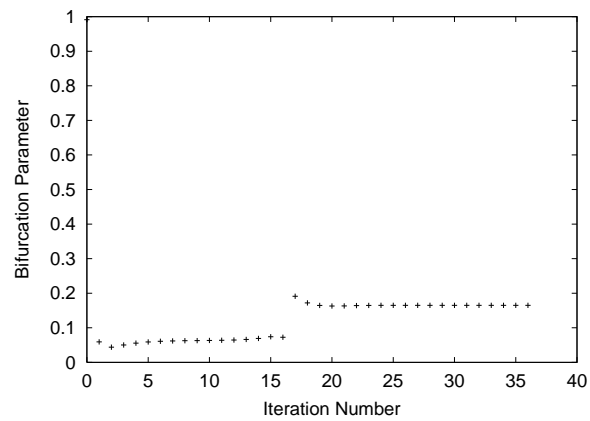
FIGURE 2.8: *Convergence of the Log of the residual against iteration number*FIGURE 2.9: *Convergence of the bifurcation parameter against iteration number*

TABLE 2.2: Grid convergence for the solution of the Augmented System

No. of Cells	Bifurcation parameter	Newton Iters	CPU Time	Nested
8	0.16508010	24	0.0	N/A
16	0.16504272	29	0.1	6
32	0.16503947	32	1.3	5
64	0.16503896	34	11.2	5
128	0.16503886	37	329	5
256	0.16503883	40	8109	5

2.7 Conclusions

The iteration scheme (2.24) has been applied to a model problem and both Hopf bifurcation points could be found however the current implementation did show some difficulties. The current linear solve cannot be used for large problems due to the $O(N^3)$ operation count this will be changed in the aeroelastic formulation to an iterative method. The initial guess used in the model problem did not allow for fast convergence of the system of equations (2.24). Indeed by just changing the size of the under-relaxation parameter it was possible to converge to both Hopf points from exactly the same starting solution. A reliable method for calculating the initial guess for the aeroelastic solution will need to be found. In general it was not possible to remove A_w in (2.24) and make the system loosely coupled. In the aeroelastic case an approximation of this term will be difficult and being able to loosely couple the system highly desirable. An inner iteration will have to be formulated to take this into account.

Chapter 3

Model Reduction

3.1 Background

The use of coordinate transformations^[77] to simplify nonlinear equations in the vicinity of a bifurcation is a well known technique for systems of low order (eg order 10 in ^[98]). The original variables are transformed so that a small number of critical variables are isolated which can describe qualitatively the behaviour of the full system for changes in the parameter near the bifurcation point. This is known as topological equivalence. In this way the structure of the topological equivalence dynamical system can be studied near the bifurcation point cheaply. The focus of this chapter is the method of projection by Kuznetsov^[87] for the computation of centre manifolds which is based on Hassard *et al.* ^[94] The transformation avoids having to compute the eigenvalues of the Jacobian matrix and so can cope with the very large systems of ordinary differential equations (ODE) arising from a discrete aeroelastic system. Kuznetsov^[99] derived explicit computational formulas for the coefficients of the normal forms for all codim 1 and 2 equilibrium bifurcations by using the reduction/normalisation technique of Coulet and Spiegel.^[100] This technique combines the calculation of the centre-manifold with the reduction to the normal form into one step.

3.2 Centre Manifold Theorems

The invariant manifold of a nonlinear system of ordinary differential equations near an equilibrium point or a limit cycle is determined by the structure of its vector

field. Two methods can be used to simplify the original nonlinear system; the centre manifold^[73] or the normal form theory^[101]. The normal form theory is a method for transforming the original nonlinear differential equation to a simpler standard form by an appropriate change of coordinates so that the main features of the manifold become clearer. Transformations have been used in fluid mechanics since Blasius.^[102]

The Hartman-Grobman theorem^[103] states that a system of ODEs in the form

$$\dot{\mathbf{w}} = f(\mathbf{w}), \quad \mathbf{w} \in \mathbb{R}^n \quad (3.1)$$

with an equilibrium point $f(0) = 0$ is dynamically equivalent near the origin to the linear system

$$\dot{\mathbf{w}} = f_{\mathbf{w}}(0)\mathbf{w} \quad (3.2)$$

if the matrix $f_{\mathbf{w}}(0)$ has no eigenvalues with zero real part.

The reduction theorem^[104] is at the heart of the study of topological equivalence of system of ODEs. According to this theorem there is a mapping Y such that the non-linear system of differential equations

$$\begin{cases} \dot{\mathbf{x}} = \mathcal{B}\mathbf{x} + g(\mathbf{x}, \mathbf{y}) \\ \dot{\mathbf{y}} = \mathcal{C}\mathbf{y} + h(\mathbf{x}, \mathbf{y}) \end{cases} \quad (3.3)$$

is topological equivalent to the partial linearised system

$$\begin{cases} \dot{\mathbf{x}} = \mathcal{B}\mathbf{x} + g(\mathbf{x}, Y(\mathbf{x})) \\ \dot{\mathbf{y}} = \mathcal{C}\mathbf{y} \end{cases} \quad (3.4)$$

if matrix \mathcal{C} has no eigenvalues with zero real part and all the eigenvalues of \mathcal{B} lie on the imaginary axis. The original proof of this theorem was given by Reizins^[105] for the case of \mathbf{x} in a one-dimensional vector space. More general cases were proved by Shoshitaishvili^[104], and Palmer^[106]. The important thing to notice is that the equations for \mathbf{x} and \mathbf{y} are decoupled in (3.4). The first equation is the restriction of (3.3) to its centre manifold W^c .^[73] The dynamics of the topological equivalent system (3.4) are easier to understand since the equation in \mathbf{y} is linear and has exponentially decaying solutions if all the eigenvalues of \mathcal{C} have negative real part.

For a Hopf bifurcation with $(\lambda_{1,2} = \pm i\omega)$ then

$$\mathcal{B} = \begin{pmatrix} 0 & -\omega \\ \omega & 0 \end{pmatrix},$$

$\mathbf{x} \in \mathbb{R}^2$, and $\mathbf{y} \in \mathbb{R}^{n-2}$. Using the complex form by use of the transformation $z = x_1 + ix_2$ then the system (3.3) looks like

$$\begin{cases} \dot{z} &= i\omega z + G(z, \bar{z}, \mathbf{y}) \\ \dot{\mathbf{y}} &= \mathcal{C}\mathbf{y} + H(z, \bar{z}, \mathbf{y}) \end{cases} \quad (3.5)$$

where G and H are smooth complex-valued functions of $z, \bar{z} \in \mathbb{C}$.

3.3 Change of Coordinates

Following the notation used in Kuznetsov^[87] suppose equation (3.1) has an equilibrium at $\mathbf{w} = 0$ and remove the linear parts from f

$$\dot{\mathbf{w}} = A\mathbf{w} + F(\mathbf{w}), \quad \mathbf{w} \in \mathbb{R}^n \quad (3.6)$$

where $F(\mathbf{w})$ has at least quadratic terms. Consider the right hand side of (3.6) written in a Taylor expansion about $\mathbf{w} = 0$

$$\dot{\mathbf{w}} = A\mathbf{w} + \frac{1}{2}B(\mathbf{w}, \mathbf{w}) + \frac{1}{6}C(\mathbf{w}, \mathbf{w}, \mathbf{w}) + \mathcal{O}\|\mathbf{w}\|^4. \quad (3.7)$$

where

$$A = f_{\mathbf{w}}(0) \quad (3.8)$$

$$B_i(\mathbf{x}, \mathbf{y}) = \sum_{j,k=1}^n \left. \frac{\partial^2 F(\boldsymbol{\xi})}{\partial \xi_j \partial \xi_k} \right|_{\boldsymbol{\xi}=0} x_j y_k, \quad i = 1, 2, \dots, n \quad (3.9)$$

$$C_i(\mathbf{x}, \mathbf{y}, \mathbf{z}) = \sum_{j,k,l=1}^n \left. \frac{\partial^3 F(\boldsymbol{\xi})}{\partial \xi_j \partial \xi_k \partial \xi_l} \right|_{\boldsymbol{\xi}=0} x_j y_k z_l, \quad i = 1, 2, \dots, n \quad (3.10)$$

and $F(\mathbf{w})$ can be written as

$$F(\mathbf{w}) = \frac{1}{2}B(\mathbf{w}, \mathbf{w}) + \frac{1}{6}C(\mathbf{w}, \mathbf{w}, \mathbf{w}) + \mathcal{O}\|\mathbf{w}\|^4. \quad (3.11)$$

To be able to apply the reduction theorem to system (3.6) the matrix A must be partitioned into eigenvalues of zero real parts and the remainder. It is theoretically possible to use Jordan blocks to find a linear mapping such that the system is diagonalisable.^[49] However, this requires the computation of all the eigenvectors of the Jacobian matrix. It is possible to store this number of vectors up to the order of 10^4 but after this storage requirements become too expensive. The cost of calculating all the eigenvalues and eigenvectors grows like n^3 and hence rapidly

becomes computationally expensive. Since matrix \mathcal{C} does not have to in Jordan form Seydel^[68] suggests a different changes of coordinates. At the Hopf bifurcation where the Jacobian matrix A has 2 critical eigenvalues $\lambda_{1,2} = \pm i\omega$. The corresponding critical eigen-space of A is 2-dimensional and non-critical eigen-space of A has $m = n - 2$ dimensions. Then equation (3.6) can be transformed by means of the following

$$\tilde{\mathbf{w}} = \begin{bmatrix} S_{11} & S_{12} \\ S_{21} & S_{22} \end{bmatrix} \mathbf{w}$$

where $S(n \times n)$, $S_{11}(2 \times 2)$, $S_{21}(m \times 2)$, $S_{12}(2 \times m)$, $S_{22}(m \times m)$ are matrices. The first 2 rows of S are left eigenvectors of A corresponding to the critical eigenvalues $\lambda_{1,2}$. To define S_{21} and S_{22} let

$$R = S^{-1} = \begin{bmatrix} R_{11} & R_{12} \\ R_{21} & I_{m \times m} \end{bmatrix}$$

where $I_{m \times m}$ is the $m \times m$ identity matrix and the first 2 columns of R are the right eigenvectors of A corresponding to the right critical eigenvalues. Here the left and right eigenvectors are normalised such that their dot product is unity. Then the matrices S and R satisfy

$$\begin{aligned} S_{21} &= -R_{21}S_{11} \\ S_{22} &= I_{m \times m} - R_{21}S_{12} \\ R_{12} &= -S_{11}^{-1}S_{12} \end{aligned}$$

and these relations define both S and R completely in terms of the critical left and right eigenvectors.

Applying a Taylor expansion of the right hand of the transformed system gives

$$\dot{\tilde{\mathbf{w}}} = \tilde{A}\tilde{\mathbf{w}} + \mathcal{O}(\|\tilde{\mathbf{w}}\|^2) \quad (3.12)$$

Following the partitioning of S and R , A is written as

$$A = \begin{bmatrix} A_{11} & A_{12} \\ A_{21} & A_{22} \end{bmatrix}$$

and \tilde{A} as

$$\tilde{A} = \begin{bmatrix} \tilde{A}_{11} & \tilde{A}_{12} \\ \tilde{A}_{21} & \tilde{A}_{22} \end{bmatrix}$$

Then in particular the block $\tilde{A}_{22} = A_{21}S_{21} + A_{22}(I - R_{21}S_{12})$ is full. This means that the matrix \mathcal{C} in equation (3.3) is also full and non trivial to calculate for a system of large dimension.

Both of the above change of coordinates suffer from the fact that the function H is not the same as the original F due to the change in variable. The derivatives of the new function can in theory be computed using the chain rule. However, computationally this will only be possible for systems of small dimension.

3.4 Method of Projection

The method of projection by Kuznetsov^[87] for the computation of centre manifolds which is based on Hassard *et al.*^[94] avoids the problems discussed above as it does not transform system (3.6) into its eigenbases. Like the method of Seydel above it uses the left and right eigenvectors of the critical eigenvalues but its “projects” the system onto these eigenvectors instead of using them in a transformation. The method is based on the Fredholm alternative theorem.^[107]

Below shows how the method of projection can be used to calculate the centre manifold for a Hopf bifurcation. This method has been applied to the Hopf and other types of bifurcations and the resulting normal forms can be found in Kuznetsov.^[87,99] Suppose the matrix A in system (3.6) has a pair of complex eigenvalues on the imaginary axis $\lambda_{1,2} = i\omega$, $\omega > 0$. Let \mathbf{p} be the right eigenvector corresponding to λ_1 . Then $\bar{\mathbf{p}}$ is the right eigenvector corresponding to λ_2 and

$$A\mathbf{p} = i\omega\mathbf{p}, \quad A\bar{\mathbf{p}} = -i\omega\bar{\mathbf{p}}.$$

The left eigenvector \mathbf{q} also has the same property

$$A^T\mathbf{q} = -i\omega\mathbf{q}, \quad A^T\bar{\mathbf{q}} = i\omega\bar{\mathbf{q}}.$$

These can be normalised such that $\langle \mathbf{q}, \mathbf{p} \rangle = 1$ where $\langle \mathbf{q}, \mathbf{p} \rangle = \sum_{i=1}^n \bar{q}_i p_i$. The eigenspace S corresponding to $\pm i\omega$ is two dimensional and is spanned by $\{\mathbf{p}_r, \mathbf{p}_i\}$, i.e. the real and imaginary parts of \mathbf{p} . The eigenspace T corresponds to all the other eigenvalues of A is $n - 2$ dimensional. Then $\mathbf{y} \in T$ if and only if $\langle \mathbf{q}, \mathbf{y} \rangle = 0$ follows from the Fredholm alternative theorem.^[107]

It is possible to decompose any $\mathbf{w} \in \mathbb{R}^n$ as

$$\mathbf{w} = z\mathbf{p} + \bar{z}\bar{\mathbf{p}} + \mathbf{y} \tag{3.13}$$

where $z \in \mathbf{C}$, $z\mathbf{p} + \bar{z}\bar{\mathbf{p}} \in S$, and $\mathbf{y} \in T$. This decompose is the critical idea of the method as \mathbf{w} has been partitioned into a part which is critical eigenspace S and a part which is in the rest T . Taking the inner product of \mathbf{q} with equation (3.13) gives

$$\langle \mathbf{q}, \mathbf{w} \rangle = z\langle \mathbf{q}, \mathbf{p} \rangle + \bar{z}\langle \mathbf{q}, \bar{\mathbf{p}} \rangle + \langle \mathbf{q}, \mathbf{y} \rangle = z + \bar{z}\langle \mathbf{q}, \bar{\mathbf{p}} \rangle \quad (3.14)$$

since \mathbf{q} and \mathbf{p} were normalised such that $\langle \mathbf{q}, \mathbf{p} \rangle = 1$ and $\mathbf{y} \in T$ implies $\langle \mathbf{q}, \mathbf{y} \rangle = 0$.

It can be shown that $\langle \mathbf{q}, \bar{\mathbf{p}} \rangle = 0$ using the definitions of the left and right eigenvectors.

$$\langle \mathbf{q}, \bar{\mathbf{p}} \rangle = \langle \mathbf{q}, \frac{1}{-i\omega} A \bar{\mathbf{p}} \rangle = \frac{1}{-i\omega} \langle A^T \mathbf{q}, \bar{\mathbf{p}} \rangle = \frac{\omega}{-i\omega} \langle \mathbf{q}, \bar{\mathbf{p}} \rangle.$$

since $\omega \neq -i\omega$ as $\omega > 0$ then $\langle \mathbf{q}, \bar{\mathbf{p}} \rangle = 0$. Using this with equation (3.14) gives

$$\langle \mathbf{q}, \mathbf{w} \rangle = z. \quad (3.15)$$

Combining equations (3.15) and (3.13) yields the system of $(n+2)$ coordinates

$$\begin{cases} z &= \langle \mathbf{q}, \mathbf{w} \rangle \\ \mathbf{y} &= \mathbf{w} - \langle \mathbf{q}, \mathbf{w} \rangle \mathbf{p} - \langle \bar{\mathbf{q}}, \mathbf{w} \rangle \bar{\mathbf{p}}. \end{cases}$$

Using these coordinates the system (3.6) has the form

$$\begin{cases} \dot{z} &= i\omega z + \langle \mathbf{q}, F(z\mathbf{p} + \bar{z}\bar{\mathbf{p}} + \mathbf{y}) \rangle \\ \dot{\mathbf{y}} &= A\mathbf{y} + F(z\mathbf{p} + \bar{z}\bar{\mathbf{p}} + \mathbf{y}) - \langle \mathbf{q}, F(z\mathbf{p} + \bar{z}\bar{\mathbf{p}} + \mathbf{y}) \rangle \mathbf{p} - \langle \bar{\mathbf{q}}, F(z\mathbf{p} + \bar{z}\bar{\mathbf{p}} + \mathbf{y}) \rangle \bar{\mathbf{p}}. \end{cases} \quad (3.16)$$

This system is $(n+2)$ dimensional however since $\mathbf{y} \in \mathbf{R}^n$ and \mathbf{q} is complex there are two real constraints on \mathbf{y} as the real and imaginary part of $\langle \mathbf{q}, \mathbf{y} \rangle$ vanish and hence is closed. The system (3.16) is now in the form of (3.3) and hence the reduction theorem can be applied.

The system (3.16) is Taylor expanded in z , \bar{z} and \mathbf{y} to give the following approximation

$$\begin{cases} \dot{z} &= i\omega z + \frac{1}{2}G_{20}z^2 + G_{11}z\bar{z} + \frac{1}{2}G_{02}\bar{z}^2 + \frac{1}{2}G_{21}z^2\bar{z} + \langle \mathbf{G}_{10}, \mathbf{y} \rangle z + \langle \mathbf{G}_{01}, \mathbf{y} \rangle \bar{z} + \dots \\ \dot{\mathbf{y}} &= A\mathbf{y} + \frac{1}{2}\mathbf{H}_{20}z^2 + \mathbf{H}_{11}z\bar{z} + \mathbf{H}_{02}\bar{z}^2 + \dots \end{cases} \quad (3.17)$$

where $G_{20}, G_{11}, G_{02}, G_{21} \in \mathbf{C}$; $\mathbf{G}_{01}, \mathbf{G}_{10}, \mathbf{H}_{ij} \in \mathbf{C}^n$. These can be calculated from the following

$$G_{jk} = \frac{\partial^{j+k}}{\partial z^j \partial \bar{z}^k} \langle \mathbf{q}, F(z\mathbf{p} + \bar{z}\bar{\mathbf{p}}) \rangle \Big|_{z=0}, \quad j+k \geq 2, \quad (3.18)$$

$$\bar{G}_{10,j} = \frac{\partial^2}{\partial y_j \partial z} \langle \mathbf{q}, F(z\mathbf{p} + \bar{z}\bar{\mathbf{p}} + \mathbf{y}) \rangle \Big|_{z=0, \mathbf{y}=0}, \quad j = 1, 2, \dots, n, \quad (3.19)$$

$$\bar{G}_{01,j} = \frac{\partial^2}{\partial y_j \partial \bar{z}} \langle \mathbf{q}, F(z\mathbf{p} + \bar{z}\bar{\mathbf{p}} + \mathbf{y}) \rangle \Big|_{z=0, \mathbf{y}=0}, \quad j = 1, 2, \dots, n, \quad (3.20)$$

$$\mathbf{H}_{jk} = \frac{\partial^{j+k}}{\partial z^j \partial \bar{z}^k} F(z\mathbf{p} + \bar{z}\bar{\mathbf{p}}) \Big|_{z=0} - G_{jk}\mathbf{p} - \bar{G}_{kj}\bar{\mathbf{p}} \quad j+k=2, \quad (3.21)$$

Using (3.11) and the definitions of the left and right eigenvectors the following formulas for equations (3.18) and (3.21) can be computed:

$$G_{20} = \langle \mathbf{q}, B(\mathbf{p}, \mathbf{p}) \rangle \quad G_{11} = \langle \mathbf{q}, B(\mathbf{p}, \bar{\mathbf{p}}) \rangle \quad G_{02} = \langle \mathbf{q}, B(\bar{\mathbf{p}}, \bar{\mathbf{p}}) \rangle \quad G_{21} = \langle \mathbf{q}, C(\mathbf{p}, \mathbf{p}, \bar{\mathbf{p}}) \rangle \quad (3.22)$$

and

$$\begin{aligned} \mathbf{H}_{20} &= B(\mathbf{p}, \mathbf{p}) - \langle \mathbf{q}, B(\mathbf{p}, \mathbf{p}) \rangle \mathbf{p} - \langle \bar{\mathbf{q}}, B(\mathbf{p}, \mathbf{p}) \rangle \bar{\mathbf{p}} \\ \mathbf{H}_{11} &= B(\mathbf{p}, \bar{\mathbf{p}}) - \langle \mathbf{q}, B(\mathbf{p}, \bar{\mathbf{p}}) \rangle \mathbf{p} - \langle \bar{\mathbf{q}}, B(\mathbf{p}, \bar{\mathbf{p}}) \rangle \bar{\mathbf{p}}. \end{aligned} \quad (3.23)$$

Since $\mathbf{y} \in \mathbb{R}^n$, $\mathbf{H}_{02} = \bar{\mathbf{H}}_{20}$. The inner products in system (3.17) can be computed:

$$\langle \mathbf{G}_{10}, \mathbf{y} \rangle = \langle \mathbf{q}, B(\mathbf{p}, \mathbf{y}) \rangle, \quad \langle \mathbf{G}_{01}, \mathbf{y} \rangle = \langle \mathbf{q}, B(\bar{\mathbf{p}}, \mathbf{y}) \rangle. \quad (3.24)$$

The method of project has lead to system (3.17) which contains the first second and third Jacobians of the original function f and inner products of the left and right eigenvalues. As long as analytic expressions or approximations to the second and third Jacobians are available the calculation of the Taylor coefficients of (3.17) is not intractable. All that remains is to apply the centre manifold theorem to system (3.17) to approximate \mathbf{y} so the restricted system has dimension 2.

The centre manifold^[73] can be represented by

$$\mathbf{y} = Y(z, \bar{z}) = \frac{1}{2} \mathbf{k}_{20} z^2 + \mathbf{k}_{11} z \bar{z} + \mathbf{k}_{02} \bar{z}^2 + \mathcal{O}|z|^3 \quad (3.25)$$

with the constraint $\langle \mathbf{q}, \mathbf{k}_{ij} \rangle = 0$. The vectors $\mathbf{k}_{ij} \in \mathbb{C}^n$ can be found from the linear equations

$$\begin{cases} (2i\omega I - A)\mathbf{k}_{20} = \mathbf{H}_{20} \\ -A\mathbf{k}_{11} = \mathbf{H}_{11} \\ (-2i\omega I - A)\mathbf{k}_{02} = \mathbf{H}_{02} \end{cases} \quad (3.26)$$

These equations are invertible since 0, and $\pm 2i\omega$ are not eigenvalues of A . Then the restricted equation can be written as

$$\begin{aligned} \dot{z} &= i\omega z + \frac{1}{2} G_{20} z^2 + G_{11} z \bar{z} + \frac{1}{2} G_{02} \bar{z}^2 \\ &+ \frac{1}{2} (G_{21} - 2\langle \mathbf{q}, B(\mathbf{p}, A^{-1} \mathbf{H}_{11}) \rangle + \langle \mathbf{q}, B(\bar{\mathbf{p}}, (2i\omega I - A)^{-1} \mathbf{H}_{20}) \rangle) z^2 \bar{z} + \dots \end{aligned} \quad (3.27)$$

Using these equations and the identities

$$A^{-1}\mathbf{p} = \frac{1}{i\omega}\mathbf{p} \quad A^{-1}\bar{\mathbf{p}} = \frac{1}{i\omega}\bar{\mathbf{p}} \quad (2i\omega I - A)^{-1}\mathbf{p} = \frac{1}{i\omega}\mathbf{p} \quad (2i\omega I - A)^{-1}\bar{\mathbf{p}} = \frac{1}{3i\omega}\bar{\mathbf{p}}$$

the restricted equation can be rewritten as

$$\dot{z} = i\omega z + \frac{1}{2}G_{20}z^2 + G_{11}z\bar{z} + \frac{1}{2}G_{02}\bar{z}^2 + \frac{1}{2}g_{21}z^2\bar{z} \quad (3.28)$$

where

$$\begin{aligned} g_{21} &= \langle \mathbf{q}, C(\mathbf{p}, \mathbf{p}, \bar{\mathbf{p}}) \rangle \\ &- 2\langle \mathbf{q}, B(\mathbf{p}, A^{-1}B(\mathbf{p}, \bar{\mathbf{p}})) \rangle + \langle \mathbf{q}, B(\bar{\mathbf{p}}, (2i\omega I - A)^{-1}B(\mathbf{p}, \mathbf{p})) \rangle \\ &+ \frac{1}{i\omega} \langle \mathbf{q}, B(\mathbf{p}, \mathbf{p}) \rangle \langle \mathbf{q}, B(\mathbf{p}, \bar{\mathbf{p}}) \rangle \\ &- \frac{2}{i\omega} |\langle \mathbf{q}, B(\mathbf{p}, \bar{\mathbf{p}}) \rangle|^2 - \frac{1}{3i\omega} |\langle \mathbf{q}, B(\bar{\mathbf{p}}, \bar{\mathbf{p}}) \rangle|^2 \end{aligned}$$

It should be noted that equation (3.28) is not the normal form^[73] of the Hopf bifurcation

$$\dot{z} = i\omega z + c_1 z^2 \bar{z} + \mathcal{O}(\|z\|^4). \quad (3.29)$$

To transform equation (3.28) into normal form requires an additional transformation to be applied to remove all the quadratic terms for example see Hassard *et al.*^[94] Equation (3.28) will be the bases of the 2 degree of freedom models used in the rest of this thesis.

3.5 Centre manifolds with one parameter dependent systems

To be able to carry out parametric studies of equation (3.1) a bifurcation parameter must be added to the system and included in the calculated centre manifolds. Consider the parameterised equation

$$\dot{\mathbf{w}} = f(\mathbf{w}, \mu) \quad (3.30)$$

where $\mathbf{w} \in \mathbb{R}^n$ and $\mu \in \mathbb{R}$. Suppose that at $\mu = 0$ the system has a Hopf bifurcation at $\mathbf{w} = 0$ with two eigenvalues on the imaginary axis. Then system (3.16) can be rewritten as

$$\begin{cases} \dot{z} &= i\omega z + \langle \mathbf{q}, F(z\mathbf{p} + \bar{z}\bar{\mathbf{p}} + \mathbf{y}, \mu) \rangle \\ \dot{\mathbf{y}} &= A\mathbf{y} + F(z\mathbf{p} + \bar{z}\bar{\mathbf{p}} + \mathbf{y}, \mu) - \langle \mathbf{q}, F(z\mathbf{p} + \bar{z}\bar{\mathbf{p}} + \mathbf{y}, \mu) \rangle \mathbf{p} - \langle \mathbf{q}, F(z\mathbf{p} + \bar{z}\bar{\mathbf{p}} + \mathbf{y}, \mu) \rangle \bar{\mathbf{p}} \end{cases}$$

This system is $(n + 2)$ dimensional but we have two constraints on \mathbf{y} . The system is Taylor expanded in z , \bar{z} and \mathbf{y} to give the following approximation

$$\begin{cases} \dot{z} = i\omega z + \frac{1}{2}G_{20}z^2 + G_{11}z\bar{z} + \frac{1}{2}G_{02}\bar{z}^2 + \frac{1}{2}G_{21}z^2\bar{z} + \langle \mathbf{G}_{10}, \mathbf{y} \rangle z + \langle \mathbf{G}_{01}, \mathbf{y} \rangle \bar{z} \\ \quad + \langle \mathbf{q}, f_\mu \mu \rangle + z\mu \langle \mathbf{q}, A_\mu \mathbf{p} \rangle + \bar{z}\mu \langle \mathbf{q}, A_\mu \bar{\mathbf{p}} \rangle + \mu \langle \mathbf{q}, A_\mu \mathbf{y} \rangle \dots \\ \dot{y} = A\mathbf{y} + \frac{1}{2}\mathbf{H}_{20}z^2 + \mathbf{H}_{11}z\bar{z} + \frac{1}{2}\mathbf{H}_{02}\bar{z}^2 + \dots \end{cases} \quad (3.31)$$

where G_{20} , G_{11} , G_{02} , $G_{21} \in \mathbb{C}$; \mathbf{G}_{01} , \mathbf{G}_{10} , $\mathbf{H}_{ij} \in \mathbb{C}^n$, involve inner products of the second and third Jacobian operators. The four extra terms $\langle \mathbf{q}, f_\mu \mu \rangle$, $z\mu \langle \mathbf{q}, A_\mu \mathbf{p} \rangle$, $\bar{z}\mu \langle \mathbf{q}, A_\mu \bar{\mathbf{p}} \rangle$ and $\mu \langle \mathbf{q}, A_\mu \mathbf{y} \rangle$ compared to equation (3.17) arise from an expansion of the f in μ and provide the reduced model with a parameterisation in μ . All of the scalars and vectors are functions of f or inner products of \mathbf{q} , f and its derivatives, and this makes the manipulation of the system feasible, even for systems of large dimension. The equation (3.31) is again restricted onto the centre manifold of the Hopf bifurcation point to yield a 2 degree of freedom model that is topological equivalent to of equation (3.30).

3.6 Computational Cost of the Method of Projection

With these identities it is possible to calculate all the terms required for both the transformed system (3.17) and the projected system (3.27). The direct calculation of the bifurcation point provides \mathbf{p} , $\bar{\mathbf{p}}$, \mathbf{w}_0 , μ_0 and ω so only the adjoint eigenvector \mathbf{q} must be calculated in addition. This can be done easily and quickly with the inverse power method since we know the value of the eigenvalue and hence have an excellent shift. This method is already employed in the direct bifurcation solver to obtain initial estimates for \mathbf{p} and is cheap compared to the direct bifurcation solution itself. The values of G_{20} , G_{11} , and G_{02} are calculated using the identities above and require just eight function evaluations and a few inner products. The same applies for G_{21} . All these terms are fixed and only need to be calculated once.

To avoid having to compute $B(\mathbf{p}, \mathbf{y})$ and $B(\bar{\mathbf{p}}, \mathbf{y})$ at each iteration, since \mathbf{y} is not fixed, two more complex linear systems are required see equations(3.26). This is due to the reduction onto the centre manifold and again they are fixed at the start and so only need to be calculated once. Once the above information is calculated the use of the reduced model is independent of the number of unknowns in the original system.

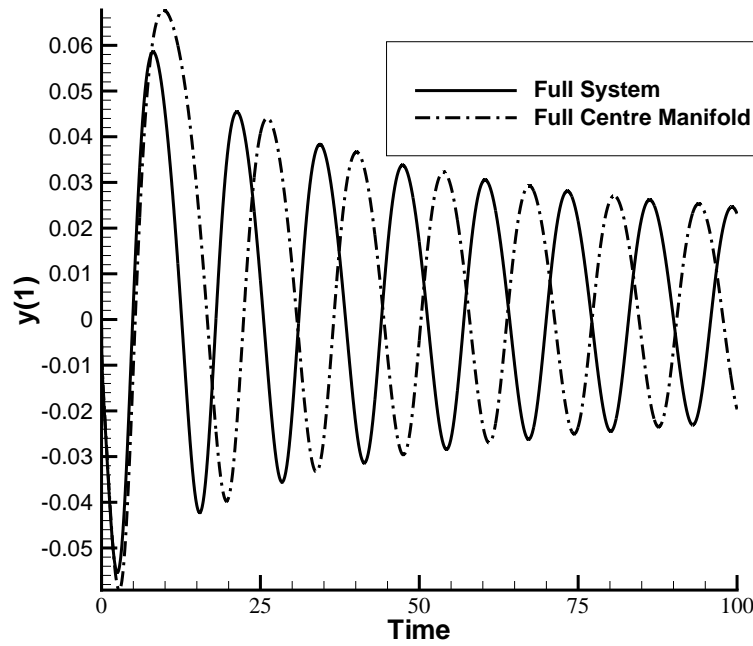


FIGURE 3.1: Comparison of the time history computed with full and reduced models of y at $x = 1$ with $\mu = 0.16508$ and an initial deflection of $\delta\Theta = 0.01$

3.7 Model Problem

The model problem is the non-adiabatic tubular reactor with axial mixing used in section 2.6. For reduced models the prediction is only expected to represent well the original model in the neighbourhood of the bifurcation point. The size of this neighbourhood is vitally important if the reduced model is going to be of practical use. The time history for y at $x = 1$ is shown in figures 3.1 and 3.2 for initial deflections of 0.01 and 0.001 respectively in Θ at $x = 1$. For the larger deflection the reduced model over-predicts the size of the initial oscillation but quickly recovers to obtain the correct amplitude and damping. This over-prediction causes a phase shift in the solution with the reduced model response slightly under-predicting the frequency.

Figure 3.3 shows the comparison of the amplitudes for the full and reduced models with varying μ . The straight line shows perfect agreement. As the bifurcation parameter is increased both the size of the amplitude of the oscillation increases as well as the discrepancy between the two models. The time history for y at $x = 1$ is shown in figures 3.4 and 3.5. Close to the bifurcation parameter there is very little

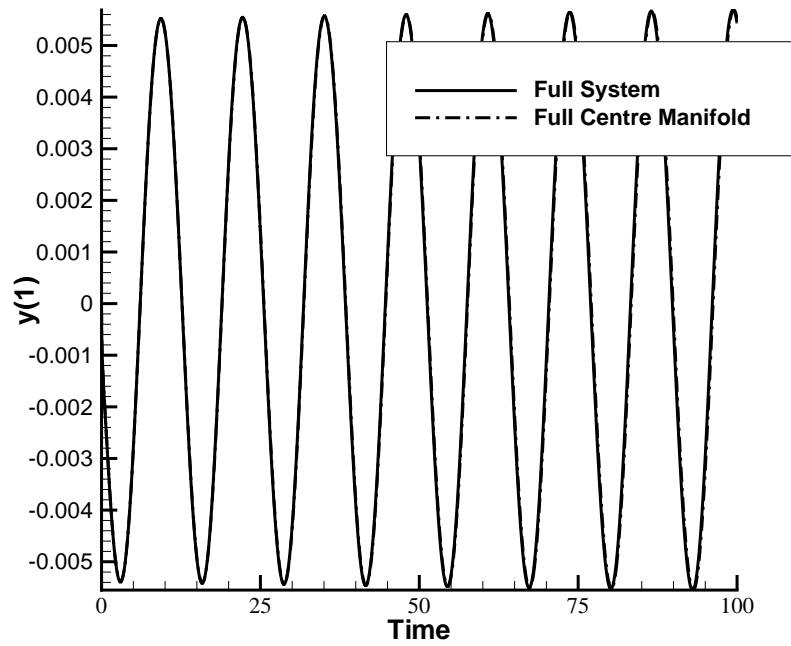


FIGURE 3.2: Comparison of the time history computed with full and reduced models of y at $x = 1$ with $\mu = 0.16508$ and an initial deflection of $\delta\Theta = 0.001$

difference between the two models while far from the bifurcation point the reduced order model over-predicts the amplitude of the oscillation and under-predicts the frequency. Similar behaviour has been obtained on the range of meshes and can be seen in figures 3.6 and 3.7 with a mesh 32 times finer.

3.8 Conclusions

We have shown that the use of the direct bifurcation method can provide extra useful information that can be incorporated into a reduced order model. Kuznetsov's^[87] method of projection was chosen since it avoids the transformation of the system into its eigenbasis which is inconceivable for aeroelastic systems of realistic size. The tubular reactor is probably a hard test for the reduction method since the solution changes rapidly for very small increases in the bifurcation parameter, (eg see the steep gradient in figure 2.5 around $\mu = 0.1605$). The accuracy of the two-degree of freedom model was independent of the size of n and enough terms have been retained in the system equations (3.31) to allow for reasonable approximation of the

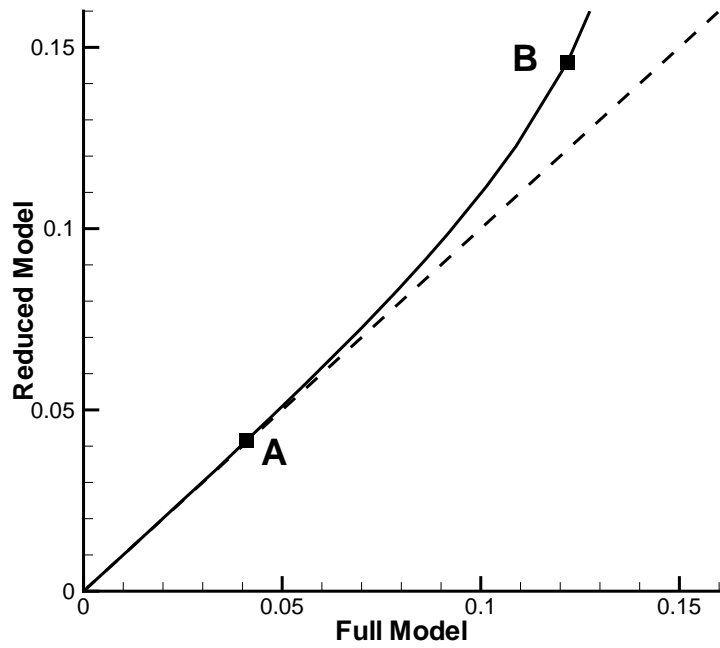


FIGURE 3.3: *The correspondence of amplitudes for the full and reduced models. The comparison of time histories at point A is shown in Figure 3.4 and in Figure 3.5 for point B*

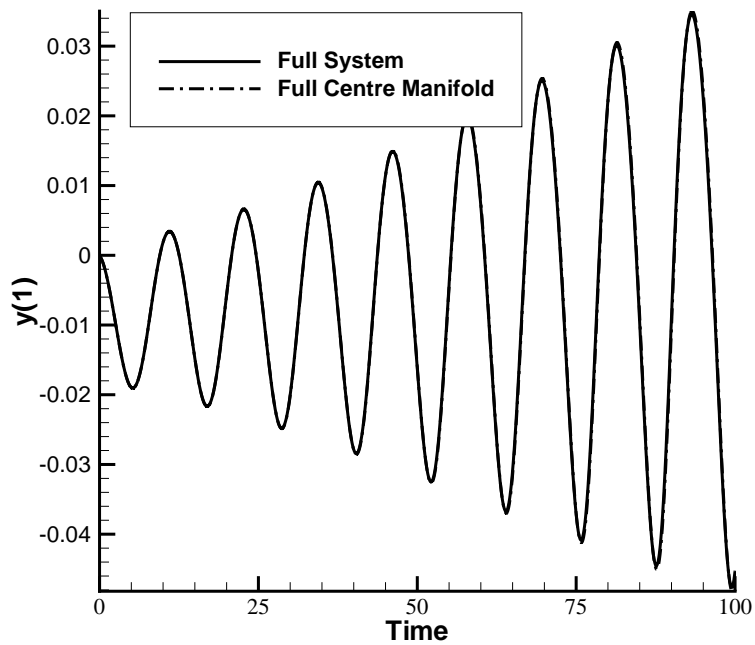


FIGURE 3.4: *Comparison of time histories close to the bifurcation point $\mu_0 + 0.00007$*

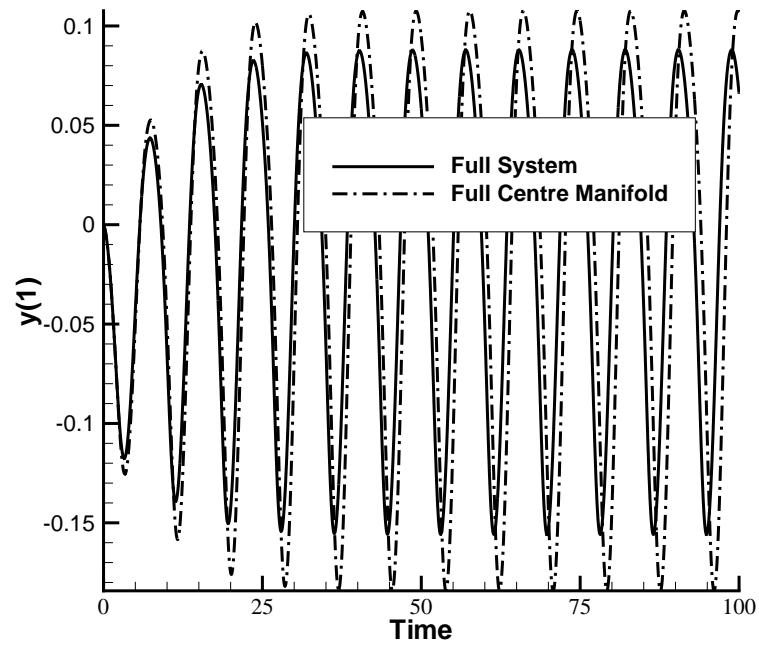


FIGURE 3.5: Comparison of time histories far from the bifurcation point $\mu_0 + 0.00075$. The full model was used to compute the solid line and the dot dashed line for the reduced model

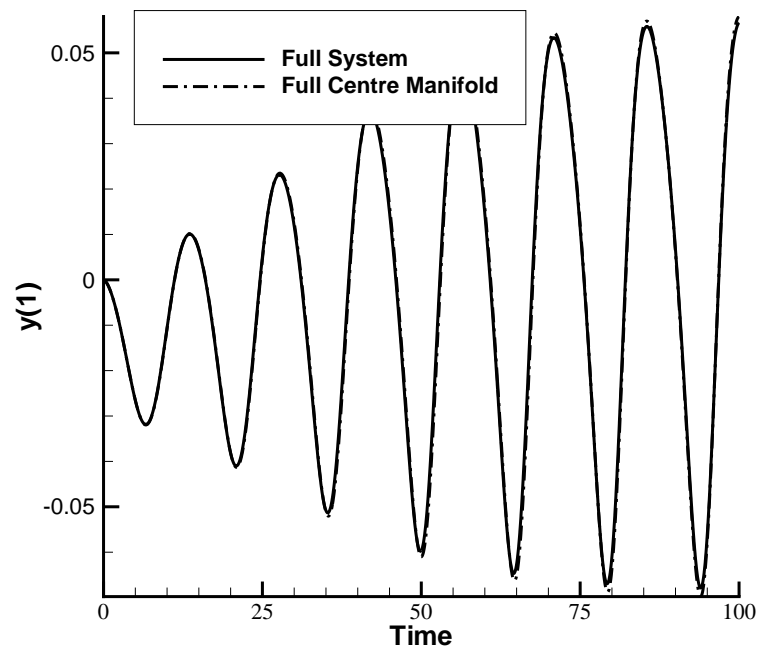


FIGURE 3.6: Comparison of time histories close to the bifurcation point $\mu_0 + 0.00007$

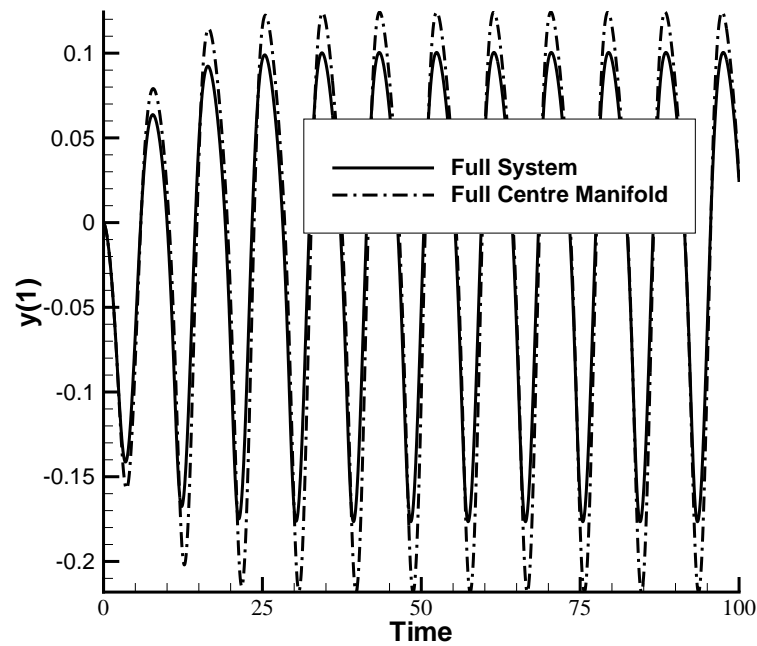


FIGURE 3.7: Comparison of time histories far from the bifurcation point $\mu_0 + 0.00075$. The full model was used to compute the solid line and the dot dashed line for the reduced model

LCO amplitude. These observations make using the system of equations (3.31) seem a viable method for aeroelastic analysis.

The remaining issues for aeroelastic systems are two fold. Firstly the coefficients in equation (3.22) were calculated analytically for this model problem. This will not be possible in the aeroelastic case. Hence a way of accurately calculating the second and third Jacobians of a second order spatial scheme will be required to build the two-degree of freedom model. Secondly the two linear systems need to be solved in (3.26) will contain the Jacobian of the second order spatial scheme so a robust linear solver is required.

A possible approach to practical aeroelastic analysis is to calculate a steady state using the coupled solver, then to calculate the bifurcation (flutter) point using a direct solve which in turn yields the information required for the model reduction. The reduced system can then be used to calculate the damping values below the flutter point, and the LCO amplitudes above it, which can then be used to compare with flight test data.

Chapter 4

Two Degree of Freedom Aeroelastic System

The augmented system was solved for an aeroelastic system consisting of an aerofoil moving in pitch and plunge by Morton and Beran^[85]. The linear system was solved using a direct method and this motivated the use of an approximate Jacobian matrix to reduce the cost of this calculation. Robustness problems were encountered when applying the method, particularly at transonic Mach numbers. A complex variable formulation was introduced in^[108] which resolved some of these problems. An approach considered to reduce the difficulties of applying a direct solver to large linear systems was to use domain decomposition to reduce the size of the system at the expense of an outer iteration over the domains. This was tested on a model problem in references^[97, 108].

The main problem with applying the solution of the augmented system in the referenced works^[85, 97, 108] can be traced to using a direct solver for the linear system, both in terms of the approximations to the Newton iteration to reduce the cost of solving these systems, and in application to large problems. The aim of the current chapter is to circumvent this problem by applying sparse matrix solvers. The chapter continues with the CFD and CSD formulation followed by the formulation of the augmented system. The two main challenges for implementing the augmented solver are then considered, namely the generation of the Jacobian matrix and the solution of the linear system. Based on results for these two topics, an iteration scheme is proposed for the solution of the augmented system and results are then presented to illustrate the performance of the scheme.

4.1 Aerodynamic and Structural Simulations

A strong conservation law form of the two-dimensional, time-dependent Euler equations for a perfect gas with conservative variables $\tilde{\mathbf{w}}_f = (\rho, \rho u, \rho v, \rho E)^T$ and time-variant curvilinear coordinates (ξ, η, t) can be written in nondimensional form as (Steger^[109]),

$$\frac{\partial \mathbf{w}_f}{\partial t} + \frac{\partial \mathbf{F}^i}{\partial \xi} + \frac{\partial \mathbf{G}^i}{\partial \eta} = 0 \quad (4.1)$$

where $\mathbf{w}_f = \tilde{\mathbf{w}}_f/J$. Here, $J = \xi_x \eta_y - \xi_y \eta_x$ is the determinant of the transformation. The flux vectors \mathbf{F}^i and \mathbf{G}^i are,

$$\mathbf{F}^i = \frac{1}{J} \begin{pmatrix} \rho U \\ \rho u U + \xi_x p \\ \rho v U + \xi_y p \\ (\rho E + p)U - \xi_t p \end{pmatrix}, \quad (4.2)$$

$$\mathbf{G}^i = \frac{1}{J} \begin{pmatrix} \rho V \\ \rho u V + \eta_x p \\ \rho v V + \eta_y p \\ (\rho E + p)V - \eta_t p \end{pmatrix}. \quad (4.3)$$

where the contravariant velocities along the ξ and η coordinates are defined as,

$$\begin{aligned} U &= \xi_x(u - x_g) + \xi_y(v - y_g) \\ V &= \eta_x(u - x_g) + \eta_y(v - y_g). \end{aligned} \quad (4.4)$$

In the above ρ , u , v , p and E denote the density, the two Cartesian components of the velocity, the pressure and the specific total energy respectively. x_g and y_g are the local grid speeds in Cartesian coordinates.

The flow solution in the current work is obtained using the code PMB (parallel multi-block). A summary of the applications examined using this code can be found in reference ^[36]. A fully implicit steady solution of the Euler equations is obtained by advancing the solution forward in time by solving the discrete nonlinear system of equations

$$\frac{\mathbf{w}_f^{t+1} - \mathbf{w}_f^t}{\Delta t} = \mathbf{R}_f(\mathbf{w}_f^{t+1}). \quad (4.5)$$

The term on the right-hand side, called the residual, is the discretisation of the convective terms, given here by Osher's approximate Riemann solver^[110], MUSCL interpolation^[111] and Van Albada's limiter. The sign of the definition of the residual

is opposite to convention in CFD but this is to provide a set of ordinary differential equations which follows the convention of dynamical systems theory, as will be discussed in the next section. Equation (4.5) is a nonlinear system of algebraic equations. These are solved by an implicit method^[89], the main features of which are an approximate linearisation to reduce the size and condition number of the linear system, and the use of a preconditioned Krylov subspace method to calculate the updates. The steady state solver is applied to unsteady problems within a pseudo-time stepping iteration.^[112]

The aerofoil is allowed to move in pitch α and plunge h . Let $\mathbf{w}_s = [h, \dot{h}, \alpha, \dot{\alpha}]^T$ be the vector of structural unknowns with dot indicating the plunge or pitch rate. Then the nondimensional equations of motion,^[2] neglecting structural damping and structural non-linearities, are

$$\frac{d\mathbf{w}_s}{dt} + M^{-1}K\mathbf{w}_s = M^{-1}\mathbf{f}_a \quad (4.6)$$

where $\mathbf{f}_a = (0, 2C_l/\mu_s\pi, 0, 4C_m/\mu_s\pi)^T$ is the vector of integrated fluid forces with lift coefficient C_l and moment coefficient C_m about the elastic axis. The matrices M and K are the mass matrix

$$M = \begin{bmatrix} 1 & 0 & 0 & 0 \\ 0 & 1 & 0 & \frac{x_\alpha}{2} \\ 0 & 0 & 1 & 0 \\ 0 & x_\alpha & 0 & \frac{r_\alpha^2}{2} \end{bmatrix} \quad (4.7)$$

and the stiffness matrix

$$\begin{bmatrix} 0 & -1 & 0 & 0 \\ \frac{4\omega_R^2}{\bar{U}^2} & 0 & 0 & 0 \\ 0 & 0 & 0 & -1 \\ 0 & 0 & \frac{2r_\alpha^2}{\bar{U}^2} & 0 \end{bmatrix}, \quad (4.8)$$

respectively. Here $r_\alpha = \sqrt{I_\alpha/m}$ is the radius of gyration defined in terms of the pitch moment of inertia I_α and the aerofoil mass per unit span m , x_α is the offset between the centre of mass and the elastic axis, $\mu_s = m/\pi\rho_\infty b^2$ is the aerofoil to fluid mass ratio defined in terms of the fluid free-stream density ρ_∞ and the semi-chord b , $\omega_R = \omega_h/\omega_\alpha$ is the ratio of the natural frequencies of plunging to pitching, $\bar{U} = U_\infty/\omega_\alpha b$ is the reduced velocity. These equations are solved by a two stage Runge-Kutta method.

The aerodynamic grid positions and speeds depend on \mathbf{w}_s . Since no aerofoil deformation is present the initial grid can be rotated and translated according to

$$\begin{bmatrix} x \\ y \end{bmatrix} = \begin{bmatrix} \cos \alpha & \sin \alpha \\ -\sin \alpha & \cos \alpha \end{bmatrix} \begin{bmatrix} x^0 - x_{ea} \\ y^0 - y_{ea} \end{bmatrix} + \begin{bmatrix} x_{ea} \\ y_{ea} + h \end{bmatrix} \quad (4.9)$$

where the superscript 0 indicates the initial position of the (x, y) point and the subscript ea indicates the location of the elastic axis. The grid speeds can then be calculated from

$$\begin{bmatrix} x_g \\ y_g \end{bmatrix} = \begin{bmatrix} \dot{\alpha}(y_{i,j} - y_{ea} - h) \\ -\dot{\alpha}(x_{i,j} - x_{ea}) + \dot{h} \end{bmatrix}. \quad (4.10)$$

For coupled CFD-CSD calculations the aerodynamic and structural solutions must be sequenced. For steady solutions, taking one step of the CFD solver followed by one step of the structural solver will result in the correct equilibrium. However, for time accurate calculations more care must be taken to avoid introducing additional errors. The exact formulation used to avoid this is discussed in reference [113].

4.2 Formulation of Augmented System

Consider the semi-discrete form of the coupled CFD-CSD system

$$\frac{d\mathbf{w}}{dt} = \mathbf{R}(\mathbf{w}, \mu) \quad (4.11)$$

where

$$\mathbf{w} = [\mathbf{w}_f, \mathbf{w}_s]^T \quad (4.12)$$

is a vector containing the fluid unknowns \mathbf{w}_f and the structural unknowns \mathbf{w}_s and

$$\mathbf{R} = [\mathbf{R}_f, \mathbf{R}_s]^T \quad (4.13)$$

is a vector containing the fluid residual \mathbf{R}_f from equation (4.5) and the structural residual $\mathbf{R}_s = M^{-1}(\mathbf{f}_a - K\mathbf{w}_s)$. The residual in equation (4.11) also depends on a parameter μ which is independent of \mathbf{w} . In the case of the pitch-plunge aerofoil there are a number of possible choices for μ and \bar{U} was chosen.

The semi-discrete equation (4.11) then can be augmented as described in

section 2.5.2 with

$$\mathbf{R}_A = \begin{bmatrix} \mathbf{R} \\ A\mathbf{p}_r + \omega\mathbf{p}_i \\ A\mathbf{p}_i - \omega\mathbf{p}_r \\ \mathbf{s}^T \mathbf{p}_r \\ \mathbf{s}^T \mathbf{p}_i - 1 \end{bmatrix} \quad (4.14)$$

and $\mathbf{w}_A = [\mathbf{w}, \mathbf{p}_r, \mathbf{p}_i, \mu, \omega]^T$. Newton's method can be used to solve this type of problem. A sequence of approximations \mathbf{w}_A^n to a solution is generated by solving the linear system

$$\frac{\partial \mathbf{R}_A}{\partial \mathbf{w}_A} \Delta \mathbf{w}_A = -\mathbf{R}_A^t \quad (4.15)$$

where $\Delta \mathbf{w}_A = \mathbf{w}_A^{t+1} - \mathbf{w}_A^t$. The Jacobian matrix on the left-hand side of equation (4.15) is given by equation (2.25).

There are three key issues for the application of equation (4.15). First, as was shown with the model problem in chapter 2, a good initial guess is required or the iterations converge slowly or even diverge. Secondly, the Jacobian matrix $\partial \mathbf{R}_A / \partial \mathbf{w}_A$ is required. Thirdly, the large sparse linear system given in equation (4.15) must be solved. These points will be considered in the following sections.

One simplification arises if we are dealing with a symmetric problem, eg a symmetrical aerofoil at zero incidence [85]. In this case $\mathbf{R}_{\bar{v}} = 0$ and hence can be calculated from equation (4.11) independently of the other Hopf conditions in equation (2.23). Then, a smaller system can be solved for this choice of the bifurcation parameter

$$\mathbf{R}_A = \begin{bmatrix} A\mathbf{p}_r + \omega\mathbf{p}_i \\ A\mathbf{p}_i - \omega\mathbf{p}_r \\ \mathbf{s}^T \mathbf{p}_r \\ \mathbf{s}^T \mathbf{p}_i - 1 \end{bmatrix} \quad (4.16)$$

with $\mathbf{w}_A = [\mathbf{p}_r, \mathbf{p}_i, \mu, \omega]^T$. The Jacobian matrix in Newton's method then becomes

$$\frac{\partial \mathbf{R}_A}{\partial \mathbf{w}_A} = \begin{bmatrix} A & I\omega & A_\mu \mathbf{p}_r & \mathbf{p}_i \\ -I\omega & A & A_\mu \mathbf{p}_i & -\mathbf{p}_r \\ \mathbf{s}^T & 0 & 0 & 0 \\ 0 & \mathbf{s}^T & 0 & 0 \end{bmatrix}. \quad (4.17)$$

For the rest of this chapter we will concentrate on solving the symmetric problem.

4.3 Calculation of the Jacobian Matrix

The difficult terms to form in the Jacobian matrix of the augmented system (4.17) are A and A_μ . The calculation of A is most conveniently done by partitioning the matrix as

$$A = \begin{bmatrix} \frac{\partial \mathbf{R}_f}{\partial \mathbf{w}_f} & \frac{\partial \mathbf{R}_f}{\partial \mathbf{w}_s} \\ \frac{\partial \mathbf{R}_s}{\partial \mathbf{w}_f} & \frac{\partial \mathbf{R}_s}{\partial \mathbf{w}_s} \end{bmatrix} = \begin{bmatrix} A_{ff} & A_{fs} \\ A_{sf} & A_{ss} \end{bmatrix}. \quad (4.18)$$

The block A_{ff} describes the influence of the fluid unknowns on the fluid residual and has by far the largest number of non-zeros for the pitch-plunge aerofoil problem. The fluid residual is calculated using Osher's scheme and the Jacobian matrix is calculated analytically in two stages. The residual for one cell in the grid is built up from fluxes. Following the usual approach for Riemann solvers,

$$\mathbf{f}_e = \mathbf{f}_e(\mathbf{w}_l, \mathbf{w}_r)$$

where $\mathbf{w}_l = \mathbf{w}_l(\mathbf{w}_{i-1,j}, \mathbf{w}_{i,j}, \mathbf{w}_{i+1,j})$ and $\mathbf{w}_r = \mathbf{w}_r(\mathbf{w}_{i,j}, \mathbf{w}_{i+1,j}, \mathbf{w}_{i+2,j})$. The left and right states are computed from the cell values using MUSCL interpolation. Assuming a uniform mesh spacing the extrapolation to the left and right states are

$$\mathbf{w}_l = \mathbf{w}_{i,j} + \frac{\phi(r_{i,j})}{4} [(1 - \chi)\Delta_- \mathbf{w}_{i,j} + (1 + \chi)\Delta_+ \mathbf{w}_{i,j}] \quad (4.19)$$

$$\mathbf{w}_r = \mathbf{w}_{i+1,j} - \frac{\phi(r_{i+1,j})}{4} [(1 - \chi)\Delta_+ \mathbf{w}_{i+1,j} + (1 + \chi)\Delta_- \mathbf{w}_{i+1,j}] \quad (4.20)$$

where $\Delta_+ \mathbf{w}_{i,j} = \mathbf{w}_{i+1,j} - \mathbf{w}_{i,j}$, $\Delta_- \mathbf{w}_{i,j} = \mathbf{w}_{i,j} - \mathbf{w}_{i-1,j}$, $\phi(r_{i,j})$ is the limiter and $r_{i,j} = \Delta_- \mathbf{w}_{i,j} / \Delta_+ \mathbf{w}_{i,j}$. In the current work the alternative form of the van Albada limiter is used namely

$$\phi(r) = \frac{2r}{r^2 + 1}. \quad (4.21)$$

Using equation (4.21) and $\chi = 0$ gives the following left and right states

$$\mathbf{w}_l = \mathbf{w}_{i,j} + \frac{1}{2} \frac{(\Delta_- \mathbf{w}_{i,j})(\Delta_+ \mathbf{w}_{i,j}) + \varepsilon}{(\Delta_- \mathbf{w}_{i,j})^2 + (\Delta_+ \mathbf{w}_{i,j})^2 + 2\varepsilon} [\Delta_- \mathbf{w}_{i,j} + \Delta_+ \mathbf{w}_{i,j}]. \quad (4.22)$$

$$\mathbf{w}_r = \mathbf{w}_{i+1,j} - \frac{1}{2} \frac{(\Delta_- \mathbf{w}_{i+1,j})(\Delta_+ \mathbf{w}_{i+1,j}) + \varepsilon}{(\Delta_- \mathbf{w}_{i+1,j})^2 + (\Delta_+ \mathbf{w}_{i+1,j})^2 + 2\varepsilon} [\Delta_- \mathbf{w}_{i+1,j} + \Delta_+ \mathbf{w}_{i+1,j}]. \quad (4.23)$$

where ε is a small number to avoid division by zero. For the cell interface there are four contributions to the Jacobian matrix arising from

$$\frac{\partial \mathbf{f}_e}{\partial \mathbf{w}_{i-1,j}}, \quad \frac{\partial \mathbf{f}_e}{\partial \mathbf{w}_{i,j}}, \quad \frac{\partial \mathbf{f}_e}{\partial \mathbf{w}_{i+1,j}}, \quad \frac{\partial \mathbf{f}_e}{\partial \mathbf{w}_{i+2,j}}.$$

The calculation of the terms

$$\frac{\partial \mathbf{f}_e}{\partial \mathbf{w}_l} \quad \text{and} \quad \frac{\partial \mathbf{f}_e}{\partial \mathbf{w}_r}$$

is non-trivial but has been coded, tested and used in the CFD solver ^[36]. These are exploited to calculate the exact Jacobian terms for the second order spatial discretisation by using the chain rule

$$\begin{aligned} \frac{\partial \mathbf{f}_e}{\partial \mathbf{w}_{i-1,j}} &= \frac{\partial \mathbf{f}_e}{\partial \mathbf{w}_l} \frac{\partial \mathbf{w}_l}{\partial \mathbf{w}_{i-1,j}} \\ \frac{\partial \mathbf{f}_e}{\partial \mathbf{w}_{i,j}} &= \frac{\partial \mathbf{f}_e}{\partial \mathbf{w}_l} \frac{\partial \mathbf{w}_l}{\partial \mathbf{w}_{i,j}} + \frac{\partial \mathbf{f}_e}{\partial \mathbf{w}_r} \frac{\partial \mathbf{w}_r}{\partial \mathbf{w}_{i,j}} \\ \frac{\partial \mathbf{f}_e}{\partial \mathbf{w}_{i+1,j}} &= \frac{\partial \mathbf{f}_e}{\partial \mathbf{w}_l} \frac{\partial \mathbf{w}_l}{\partial \mathbf{w}_{i+1,j}} + \frac{\partial \mathbf{f}_e}{\partial \mathbf{w}_r} \frac{\partial \mathbf{w}_r}{\partial \mathbf{w}_{i+1,j}} \\ \frac{\partial \mathbf{f}_e}{\partial \mathbf{w}_{i+2,j}} &= \frac{\partial \mathbf{f}_e}{\partial \mathbf{w}_r} \frac{\partial \mathbf{w}_r}{\partial \mathbf{w}_{i+2,j}} \end{aligned}$$

Some care must be taken at boundaries where halo cells are used to simplify implementation. The halo values are functions of the internal values $\mathbf{w}_{b1} = \mathbf{w}_{b1}(\mathbf{w}_1, \mathbf{w}_2)$ and $\mathbf{w}_{b2} = \mathbf{w}_{b2}(\mathbf{w}_1, \mathbf{w}_2)$. The value of the halo cells is determined by the boundary condition. For example a simple outflow boundary sets the halos values to free-stream so making \mathbf{w}_{b1} and \mathbf{w}_{b2} independent of \mathbf{w}_1 and \mathbf{w}_2 . Applying the chain rule,

$$\frac{\partial \mathbf{f}_b}{\partial \mathbf{w}_1} = \frac{\partial \mathbf{f}_b}{\partial \mathbf{w}_l} \frac{\partial \mathbf{w}_l}{\partial \mathbf{w}_1} + \frac{\partial \mathbf{f}_b}{\partial \mathbf{w}_r} \frac{\partial \mathbf{w}_r}{\partial \mathbf{w}_1} + \frac{\partial \mathbf{f}_b}{\partial \mathbf{w}_l} \frac{\partial \mathbf{w}_l}{\partial \mathbf{w}_{b1}} \frac{\partial \mathbf{w}_{b1}}{\partial \mathbf{w}_1} + \frac{\partial \mathbf{f}_b}{\partial \mathbf{w}_r} \frac{\partial \mathbf{w}_r}{\partial \mathbf{w}_{b1}} \frac{\partial \mathbf{w}_{b1}}{\partial \mathbf{w}_1} + \frac{\partial \mathbf{f}_b}{\partial \mathbf{w}_l} \frac{\partial \mathbf{w}_l}{\partial \mathbf{w}_{b2}} \frac{\partial \mathbf{w}_{b2}}{\partial \mathbf{w}_1}$$

and

$$\frac{\partial \mathbf{f}_b}{\partial \mathbf{w}_2} = \frac{\partial \mathbf{f}_b}{\partial \mathbf{w}_l} \frac{\partial \mathbf{w}_l}{\partial \mathbf{w}_2} + \frac{\partial \mathbf{f}_b}{\partial \mathbf{w}_r} \frac{\partial \mathbf{w}_r}{\partial \mathbf{w}_2} + \frac{\partial \mathbf{f}_b}{\partial \mathbf{w}_l} \frac{\partial \mathbf{w}_l}{\partial \mathbf{w}_{b1}} \frac{\partial \mathbf{w}_{b1}}{\partial \mathbf{w}_2} + \frac{\partial \mathbf{f}_b}{\partial \mathbf{w}_l} \frac{\partial \mathbf{w}_l}{\partial \mathbf{w}_{b2}} \frac{\partial \mathbf{w}_{b2}}{\partial \mathbf{w}_2}.$$

The dependence of the halo values on the interior values leads to similar extra terms from the adjacent interfaces to the boundary also.

The Jacobians of the second-order spatial scheme were tested by forming matrix vector products against random vectors and comparing with the results from a matrix free product. In two dimensions there are nine non-zero 4x4 blocks for every cell in the grid. The Jacobian calculated in this way is referred to as second order throughout this chapter.

An approximate Jacobian matrix, referred to as modified order, is also used in the iteration scheme defined below, and has been used with success to accelerate CFD only calculations ^[36]. The approximation is to equate the terms arising from a

flux calculation associated with cells to the left and right of an interface without the dependence on the left and right states calculated from the MUSCL interpolation.

$$\frac{\partial \mathbf{f}_e}{\partial \mathbf{w}_{i-1,j}} = \mathbf{0}; \quad \frac{\partial \mathbf{f}_e}{\partial \mathbf{w}_{i,j}} = \frac{\partial \mathbf{f}_e}{\partial \mathbf{w}_l}; \quad \frac{\partial \mathbf{f}_e}{\partial \mathbf{w}_{i+1,j}} = \frac{\partial \mathbf{f}_e}{\partial \mathbf{w}_r}; \quad \frac{\partial \mathbf{f}_e}{\partial \mathbf{w}_{i,j}} = \mathbf{0}$$

With this approximation the number of non-zero contributions arising from each flux calculation is reduced from four blocks to two. This scheme is similar to calculating the exact Jacobian matrix for a first-order spatial discretisation, with the modification that the MUSCL interpolated values at the interface are used in the evaluation rather than the cell values that would be used for a first-order spatial scheme. In fact these approximations are exact for a first-order spatial discretisation where $\mathbf{w}_l = \mathbf{w}_{i-1,j}$ and $\mathbf{w}_r = \mathbf{w}_{i,j}$.

The dependence of the fluid residual on the structural unknowns is partially hidden by the notation used. The fluid residual depends not only on the fluid cell values but also on the location of the grid points themselves. The fluid and structural unknowns are independent variables and hence to calculate the term A_{fs} the fluid unknowns are kept fixed. The influence of the structural unknowns is felt through the moving grid. For example, for an aerofoil moving in pitch and plunge the grid is translated and rotated according to the current values of the structural solution. In addition the residual also depends on the mesh speeds. The easiest way of computing A_{fs} is, keeping \mathbf{w}_f fixed, to increment the structural unknowns in turn (ie $\alpha, \dot{\alpha}, h, \dot{h}$), to update the grid locations and speeds, re-evaluate the fluid residual and use a finite difference to calculate the Jacobian terms one column at a time. This requires n_s fluid residual evaluations where n_s is the number of structural unknowns, and is relatively cheap if n_s is small, as is the case for the pitch-plunge aerofoil where $n_s = 4$.

The term A_{sf} essentially involves calculating the dependence of integrated fluid forces on the fluid unknowns. For example, for the pitch-plunge aerofoil the fluid variables contribute to the structural equations through the lift and moment coefficients. In turn, these coefficients are calculated using a linear combination of the values of pressure in the two cells adjacent to the aerofoil surface. It is therefore straight-forward to calculate the exact terms in the Jacobian matrix.

Finally, the exact Jacobian matrix for the dependence of the structural equations on the structural unknowns is easy to calculate from equation (4.6).

For the two-degree of freedom aerofoil the bifurcation parameter (\bar{U} in this

case) only appears in the structural equations and in terms involving the structural unknowns. Therefore, for this case, we have

$$A_\mu = \begin{bmatrix} 0 & 0 \\ 0 & \frac{\partial^2 \mathbf{R}_s}{\partial \mu \partial \mathbf{w}_s} \end{bmatrix} \quad (4.24)$$

Due to the simple algebraic expression for $\partial \mathbf{R}_s / \partial \mathbf{w}_s$ it is straightforward to calculate the required term analytically.

A simplification is used to reduce storage requirements for the evaluation of the augmented residual, which requires the products $\mathbf{A}\mathbf{p}_r$ and $\mathbf{A}\mathbf{p}_i$. This can be done using a matrix free formulation as

$$\mathbf{A}\mathbf{x} \approx \frac{\mathbf{R}(\mathbf{w} + h\mathbf{x}) - \mathbf{R}(\mathbf{w} - h\mathbf{x})}{2h} \quad (4.25)$$

where \mathbf{x} denotes the real or imaginary part of the critical eigenvalue and h is the increment applied. Computing this expression is not costly as it requires only two residual evaluations. This gives a very accurate approximation to the required product without having to evaluate and store A . The matrix A is required for the left hand side coefficient matrix but the modified order approximation is used for this purpose which reduces the storage. Hence, using the matrix free evaluation of the augmented residual reduces the memory requirements for the scheme overall and simplifies the code considerably. The use of automatic differentiation ^[114,115] tools, with some effort put into recoding the residual calculations, would allow the required terms for the right-hand side to be evaluated exactly.

4.4 Solution of the Linear System

The calculation of the Newton updates requires the solution of the large sparse linear system in equation (4.15). Experience with solving CFD only problems^[116] shows that the system can potentially be solved efficiently by Krylov subspace type iterative solvers^[117]. The majority of the non-zero terms in the matrix are associated with the eigenvector real and imaginary parts. Hence, initial experiments for the linear solver were carried out for the system with coefficient matrix

$$\mathbf{C} = \begin{bmatrix} A & I\omega \\ -I\omega & A \end{bmatrix} \quad (4.26)$$

where the matrix A is evaluated at an equilibrium solution for the NACA0012 aerofoil at a freestream Mach number of 0.5 and zero incidence. The reduced velocity was chosen to be the bifurcation value and ω the imaginary component of the critical eigenvector. The calculations shown here were done on the medium grid, as described below, and the matrix is of modified accuracy unless otherwise stated.

For the formulation of the Newton iterations the matrix is presented in a block form, which is convenient for calculating, coding and describing the various contributions to the iteration. These blocks are not used in the linear solution which operates on non-zeros in the matrix regardless of their origin. However, within the Jacobian matrix A there is also a natural block structure since the discretisation of the Euler equations is expressed cell by cell, with four conserved variables in each cell. This means that A consists of 4×4 blocks. For the discussion of the preconditioning of the iterative solver this latter block structure is either exploited (i.e. operations in the factorisation are done on the 4×4 blocks) or it is ignored, in which case operations are done directly on the elements of the matrix. The former case is referred to as block and the latter as point wise.

The key issue for iterative linear solvers is usually the preconditioner. The incomplete LU factorisation family ^[117] can be very effective at approximating the inverse of the coefficient matrix with a small number of terms. For CFD calculations, block ILU factorisations with no fill in have proved very successful ^[36]. Here no fill in means that the factorisation has the same sparsity pattern as the coefficient matrix.

Due to the structure of the coefficient matrix and the previous success in calculating effective preconditioners for the matrix A , initial attempts to factorise the matrix C focused on the two block factorisation

$$\begin{bmatrix} A & I\omega \\ -I\omega & A \end{bmatrix} = \begin{bmatrix} I & 0 \\ -\omega A^{-1} & I \end{bmatrix} \begin{bmatrix} A & I\omega \\ 0 & A + \omega^2 A^{-1} \end{bmatrix}. \quad (4.27)$$

However, manipulating the term $A + \omega^2 A^{-1}$ efficiently is not straightforward (in particular the inverse of this term is required) and so these efforts were abandoned. The BILU factorisation of the matrix C is calculated directly as opposed to being constructed in terms of a factorisation of A .

The sparse matrix package Aztec ^[118] was used to carry out experiments for the solution of this system. This package has three main solvers available, namely GMRES, CGS and TFQMR, although the differences in performance for the cur-

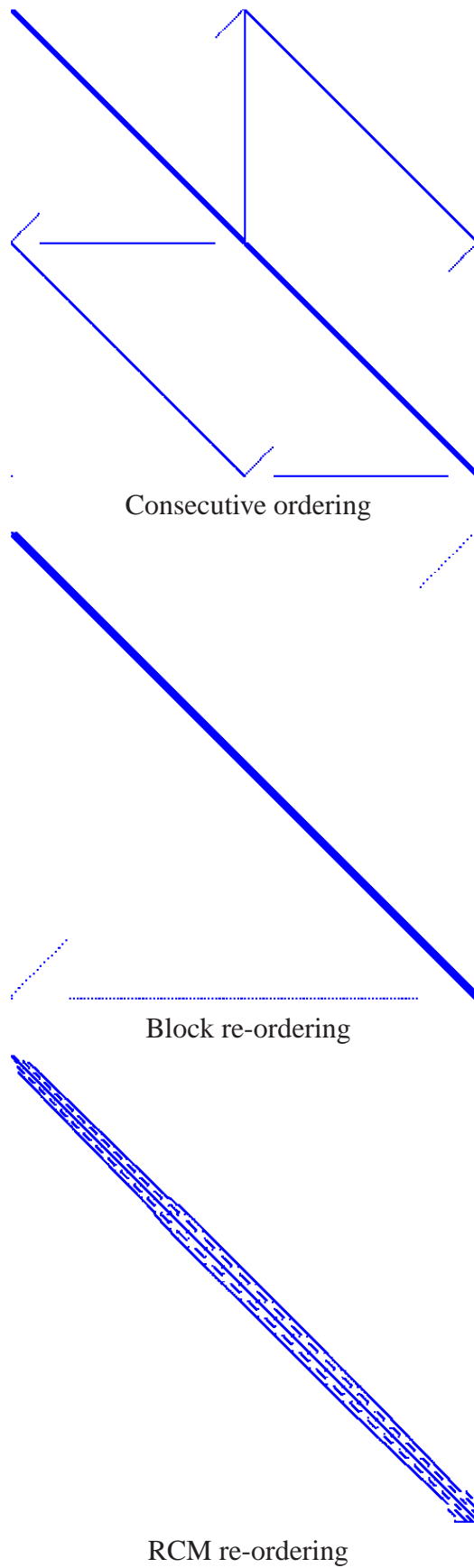


FIGURE 4.1: Sparsity patterns for various orderings of the augmented matrix

rent problem were found to be small. The last solver was found to work best for the current problems and so is used throughout this chapter. A variety of preconditioners are also available including pointwise ILU (i.e. working on the elements) and block ILU (working on the matrix in its block structured form). Various levels of fill in can be generated in the factorisation. The pointwise ILU preconditioner allows reordering to minimise the bandwidth by the reverse Cuthill McGee (RCM) algorithm. This is not available for the BILU factorisation. Two different orderings have also been used for the matrix when generated. The first lists all of the unknowns associated with the real and then the imaginary parts of the eigenvector, and the second orders the real and imaginary parts of the eigenvector components associated with each cell in the grid consecutively, referred to as block reordering. The sparsity patterns for these two orderings and the RCM reordering are shown in figure 4.1 and verify which shows RCM reordering is effective in minimising the bandwidth of the matrix.

Various calculations were carried out with the test matrix (4.26). First, the value of ω was set to zero to obtain a system which is close to that of the CFD-CSD only problem. Secondly the problem was solved with the correct value for ω and with the various orderings for ILU and BILU factorisations. Finally, one of these cases was rerun with a second-order Jacobian matrix for A . The results are summarised in figure 4.2. First, the system with ω set to zero was most easily solved and the performance of the iterative solver in this case is comparable with previous experience for the CFD-CSD only system. The RCM reordering makes the largest difference between all of the options for the modified order matrix but the performance for all three orderings is similar. Also, the ILU and BILU factorisations give similar convergence behaviour. Finally, the second order system does not converge when using preconditioning with no fill-in. For comparison a calculation was run using level one fill-in for the factorisation. This results in about ten times the number of terms being generated in the factorisation which means it is a better preconditioner but is much more expensive to calculate and use. Although the level one preconditioned system required fewer iterative steps to converge, the CPU time required for the level one solution was around twenty times longer and the memory required is an order of magnitude higher.

The following conclusions were drawn for the solution of the linear system:

- The preconditioning for the augmented system cannot easily be based on

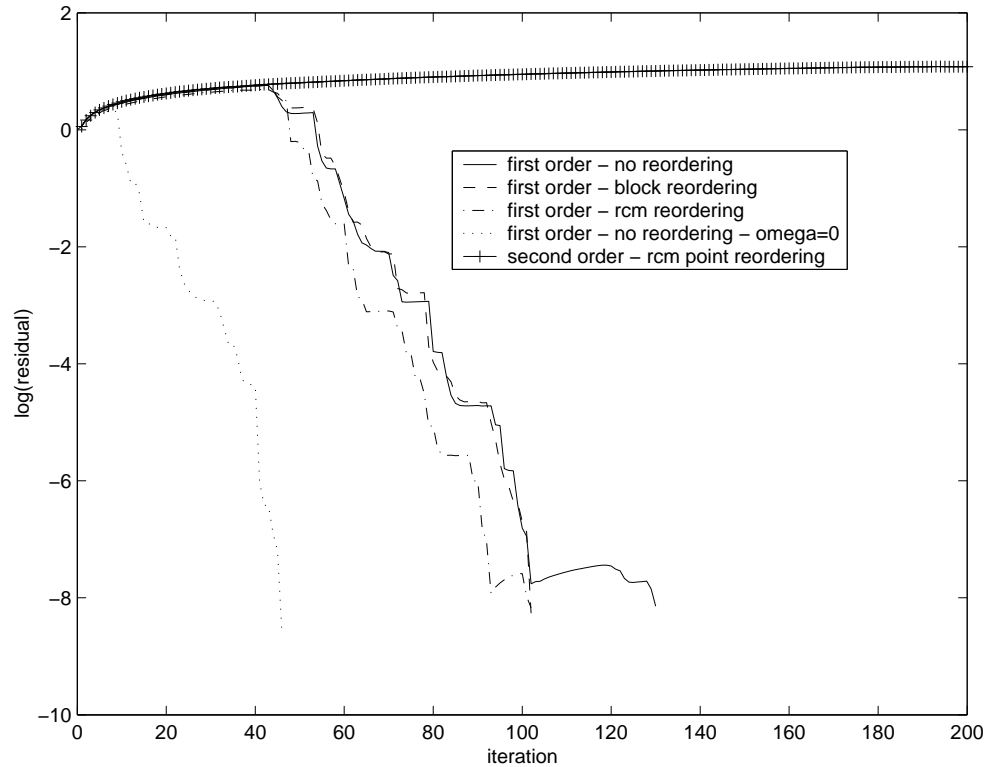


FIGURE 4.2: *Convergence histories for TFQMR solution of augmented system using several preconditioning options*

factorisations of A alone.

- The augmented linear systems are significantly more difficult to solve than CFD-CSD only systems.
- The second-order Jacobians cannot be solved with zero fill-in preconditioners whereas the modified order Jacobians can.
- Using RCM reordering marginally improves the convergence rate.

4.5 Iteration scheme for flutter boundaries

Many approximations to the coefficient matrix on the left-hand side of equation (4.15) are possible which still lead to a convergent iteration scheme. Approximations will tend to reduce the rate of convergence (and in particular will lead to the loss of quadratic convergence). However, the potential gains if the linear system is made easier to solve can outweigh this effect. This has been exploited for CFD only solvers where, for example, the Jacobian matrix associated with a first-order spatial scheme has been used to drive a higher order scheme to convergence^[36].

The advantages are first, the linear system is much better conditioned and can be solved in a smaller number of iterations, secondly the number of non-zero blocks in the matrix is reduced by a factor of 5/9 and finally, since the stencil is reduced, parallel communication is also reduced during the solution of the linear system. For inviscid flows around aerofoils, a reduction in the time to convergence for a CFD solver by a factor of four has been achieved.^[36]

The results from the tests on the linear solver suggest that the linear system associated with the second-order Jacobian matrix is too badly conditioned to be solved efficiently by the methods used in this chapter. The modified-order Jacobian is therefore considered as a replacement. This means that the iteration scheme is given by

$$\frac{\partial \bar{\mathbf{R}}_A}{\partial \mathbf{w}_A} \Delta \mathbf{w}_A = -\mathbf{R}_A^n \quad (4.28)$$

where

$$\frac{\partial \bar{\mathbf{R}}_A}{\partial \mathbf{w}_A} = \begin{bmatrix} \bar{A} & I\omega & \bar{A}_\mu \mathbf{p}_r & \mathbf{p}_i \\ -I\omega & \bar{A} & \bar{A}_\mu \mathbf{p}_i & -\mathbf{p}_r \\ \mathbf{s}^T & 0 & 0 & 0 \\ 0 & \mathbf{s}^T & 0 & 0 \end{bmatrix}. \quad (4.29)$$

Here

$$\bar{A} = \begin{bmatrix} \bar{A}_{ff} & A_{fs} \\ A_{sf} & A_{ss} \end{bmatrix} \quad (4.30)$$

where \bar{A}_{ff} is the modified-order fluid Jacobian as described above.

As was shown with the model problem in chapter 2 a good initial guess is important to obtain fast convergence of system (2.24). Assuming that the method will be used to trace out a stability boundary for varying values of a parameter, which in the current work is the freestream Mach number. At low values of Mach number, linear aerodynamic theory gives a good estimate of the bifurcation parameter and frequency of the unstable solution (the critical μ and ω). Alternatively time marching calculations can be used to find these values at one Mach number. We adopt the notation that the t^{th} approximation to the critical values at the k^{th} Mach number M_∞^k are denoted by $\mu^{t,k}$ and $\omega^{t,k}$, and the converged values by μ^k and ω^k . With this notation, the chosen values for $\mu^{1,1}$ and $\omega^{1,1}$ are assumed to be good estimates of μ^1 and ω^1 . Also, the converged values at the previous Mach number give a reasonable initial guess for the next one, i.e. $\mu^{1,k+1} = \mu^k$ and $\omega^{1,k+1} = \omega^k$ are satisfactory starting values at M_∞^{k+1} .

The initial guess for the eigenvector is crucial to obtaining convergence. If a good estimate for an eigenvalue is known then the inverse power method can be used to calculate the corresponding eigenvector^[119]. For a matrix A , the inverse power method iteration is given by

$$(A - i\omega_s I)\mathbf{p}^t = \mathbf{x}_p^{t-1} \quad (4.31)$$

and

$$\mathbf{x}_p^t = \frac{\mathbf{p}^t}{\|\mathbf{p}^t\|_\infty}. \quad (4.32)$$

This iteration converges to the eigenvector \mathbf{p} which corresponds to the eigenvalue in the spectrum of A which is closest to $i\omega_s$. Writing out the system in equation (4.31) in real and imaginary parts leads to a coefficient matrix of the form given in equation (4.26) and so the linear system to be solved is close to that of the augmented system (4.17). Therefore, the eigenvector is calculated for the modified order Jacobian \bar{A} to again allow easier solution of the linear system. The inverse power method is used to generate the initial approximation to the critical eigenvector at the first Mach number. At subsequent Mach numbers the converged eigenvector from the previous one is used as the initial guess.

For the second-order Jacobian the inverse power method can be used to trace the behaviour of an aeroelastic eigenvalue as the bifurcation value is changed. In a manner similar to linear methods, for each structural mode, the structural frequency is used as a shift and the corresponding aeroelastic eigenvalue calculated. This can then be used as a shift at the next parameter value and so on. The damping of each mode can then be traced.

Since the Jacobian matrix has been approximated it is interesting to see if additional approximations can be made, particularly since it has already been seen that the linear system (4.26) without the $I\omega$ terms in the off-diagonal blocks is much easier to solve. In addition, the part of one of these terms corresponding to the fluid unknowns was set to zero by Morton and Beran^[85] to allow for a more efficient direct solution of the linear system. Experiments were carried out to solve the augmented system at a Mach number of 0.5 with various combinations of these terms left out. The convergence rates omitting neither (full), $-I\omega$ (lower), $I\omega$ (upper) and both (both) of these terms is shown in figure 4.3 with the labels in brackets used on the figure. For the case when one of the terms is omitted the iteration fails to converge. When both terms are omitted the iteration converges but to the wrong

value of μ . Hence, it appears that, in general, making further approximations to the

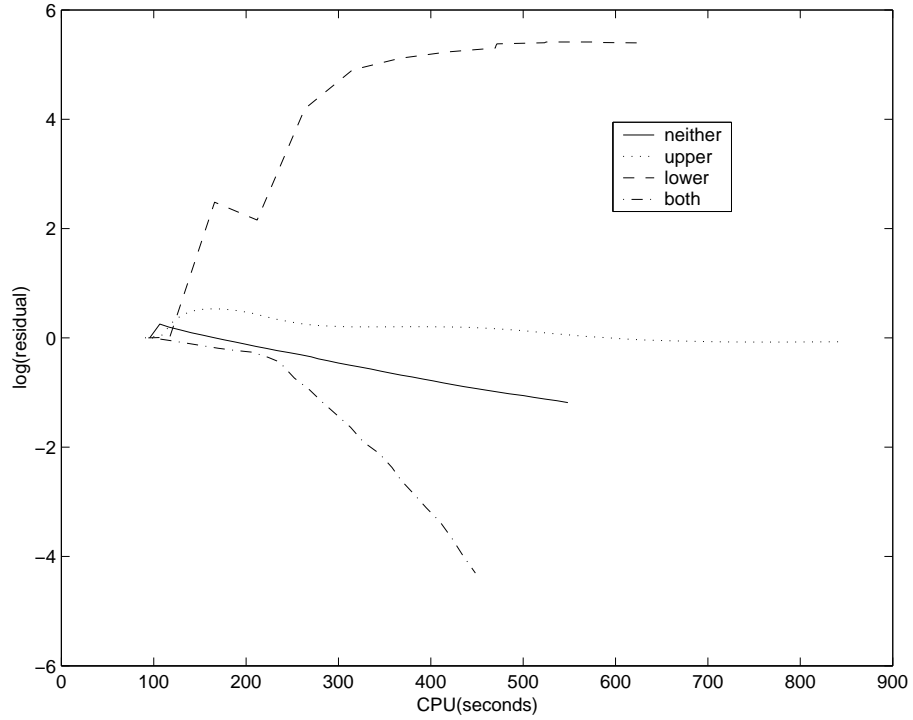


FIGURE 4.3: Comparison of convergence rate for retaining various combinations of $I\omega$ terms in augmented Jacobian matrix

augmented Jacobian adversely effects the performance of the scheme. The iteration scheme for calculating the bifurcation behaviour at a new Mach number M_∞^k is therefore the following:

- Calculate \bar{A} at the converged fluid-structure steady state (all of which except A_{ss} are independent of μ due to symmetry).
- Set starting values for the iteration as $\omega^{1,k} = \omega^{k-1}$, $\mu^{1,k} = \mu^{k-1}$ and $\mathbf{p}^{1,k} = \mathbf{p}^{k-1}$.
- Solve equation (4.28) and update solution by $\mathbf{w}_A^{n+1,k} = \mathbf{w}_A^{n,k} + \psi \Delta \mathbf{w}_A$ where ψ is a relaxation parameter chosen to be between 0 and 1, repeating until convergence.

4.6 Results for Symmetric Problem

The test problem considered to illustrate the performance of the proposed scheme is that of a NACA0012 aerofoil at zero incidence. The parameters for the structural model are given in table 4.1. Two cases are considered for varying aerofoil mass.

The first, called the light case, has $\mu_s = 10$ and the second, called the heavy case, has $\mu_s = 100$.

TABLE 4.1: *Structural model parameters*

Parameter	Value
r_α	0.539
x_α	-0.2
ω_R	0.343
μ_s	100.0 (heavy case)
μ_s	10.0 (light case)
x_{ea}	0.4
y_{ea}	0.0

The starting grid used for the calculations is of C topology and has 257 points wrapped around the aerofoil and 65 points normal and is shown in figure 4.4. The mesh is divided into three blocks for the solver and the block boundaries are indicated on the figure, running normal and streamwise from the trailing edge. The far field is located 15 chords away and the first spacing on the aerofoil surface is one hundredth of the chord. A medium grid was defined by taking every second point in each direction, a coarse grid by taking every fourth point and a very coarse grid by taking every eighth point.

To check the mesh used a steady state calculation was made for zero incidence and $M_\infty = 0.8$ and the results on the fine and medium grids are shown in figure 4.5 and agree closely, with only minor differences in the shock resolution. These results give confidence in the medium grid, which is used for the bifurcation calculations.

A check on the augmented solver can be made for the very coarse grid by computing using Matlab the complete eigenvalue spectrum of A at fixed values of $\mu = \bar{U}$ for the light case. The value of \bar{U} obtained on this grid for a Mach number of 0.5 is $\bar{U} = 1.6311$. The eigenspectrum for values of \bar{U} of 1.62, 1.6311 and 1.64 are plotted on various scales in figure 4.6. The critical eigenvalue crosses the imaginary axis at the value computed by the augmented solver, providing confirmation of the accuracy of the solver.

The scheme proposed in the previous section was first used to compute the stability boundary for the light case between Mach numbers of 0.5 and 0.95. This range includes transonic effects. The initial values for \bar{U} and ω were found from

time marching calculations at the first Mach number. The bifurcation calculation was first made on the coarse grid for Mach number steps of 0.05 and then on the medium grid for similar steps. These calculations indicated that the behaviour in the region 0.8 to 0.95 had not been resolved adequately and the resolution here was increased to steps of 0.01 on each grid. The resulting stability boundaries on the two grids are compared in figure 4.7 and are in good agreement. The augmented residual was reduced by three to four orders of magnitude, with up to 20 steps per Mach number used. This was sufficient to converge the bifurcation parameter to five significant figures and so is very conservative. The convergence behaviour in terms of the original calculation on the medium grid is shown in figure 4.8 where the reduction in residual and the convergence of μ is shown as a function of the augmented solver iteration. The residual of the linear solver was reduced by two orders at each augmented step. On average this means that 30 Krylov steps are required per solution of the linear solve, partly due to the plateau encountered at the start of each solve. Hence, there is scope for improving on the current performance by modifying the preconditioner and relaxing the convergence criteria. Nevertheless, the stability boundary using the initial 10 Mach numbers was traced out for the medium mesh in 4500 CPU seconds on a 1 GHz processor. An additional twenty Mach numbers were calculated in 7578 seconds.

The main cost of the direct solution is divided almost evenly between the CFD-CSD calculation of the steady state and the augmented solution. The cost of calculating the flutter point is about equivalent to a CFD steady state calculation at each Mach number. To put this in perspective, each time marching calculation requires about 3300 seconds on a 1 GHz processor to compute four cycles of the response. Four cycles indicates whether or not a solution is diverging for simple problems like the current one but may be insufficient to see the behaviour for a complex system which involves a larger number of degrees of freedoms. Care was taken to ensure convergence of these solutions with respect to the time step. Two sets of tests were carried out. First, the convergence of the time histories with regard to the pseudo time stepping tolerance was examined and it was found that the residual had to be reduced by three orders of magnitude at each real time step, leading to between 6-8 pseudo iterations. Secondly, a time step convergence study was carried out and again to achieve a converged prediction of the growth of the response a time step of 0.125, corresponding to about 120 real time steps per pitch-

ing cycle, was required. It is considered that there is little scope for speeding up the time marching calculations using the current solver since the number of time steps required is fixed by accuracy requirements and not solver requirements such as stability. For each Mach number at least three time marching calculations are required to locate the flutter speed, and several more would be required to locate the value to five significant figures. The behaviour of the time marching responses at conditions chosen to straddle the stability boundary are compared with the direct boundary in figure 4.9 on the medium grid and are in close agreement.

The heavy case proved more challenging for the augmented solver. This case has stability up to larger values of μ but also has two regions of high gradients in the transonic region of the μ -Mach stability curve. The initial calculations on the coarse grid successfully traced the curve over the entire Mach range and then for refined resolution in the transonic range, as for the light case. However, the augmented calculations on the medium grid diverged at the two values of Mach number (0.83 and 0.89) with maximum change in μ . The solution to this was to calculate the three regions separately, starting from information obtained on the coarse grid. The agreement between the calculations on the two grids is shown in figure 4.10 and again is close. The comparison with selected time marching calculations is shown in figure 4.11 and again shows consistency. The costs of the calculations are as for the light case.

4.7 Conclusions

A new iteration scheme for the direct calculation of aeroelastic instability boundaries has been proposed. The scheme builds on the original work of Morton and Beran by first using an iterative sparse linear solver to improve on the cost of direct methods, and secondly approximating the Jacobian matrix in the iteration scheme without overly disrupting the convergence or robustness of the scheme. To improve robustness the inverse power method is used to obtain a starting solution for the critical eigenvector.

The method has been tested on a symmetric pitch-plunge aerofoil problem. The stability boundary at zero incidence and ten Mach numbers on the medium grid was traced out by the direct scheme in less than one hour on a 1 GHz processor. There is scope for reducing this cost by relaxing the convergence criteria and by

improving the preconditioning. In any case, the method already only requires a time to calculate the stability boundary at each Mach number which is similar to a steady state CFD calculation. The whole boundary defined at 25 Mach numbers requires the time needed for about 3-4 time marching calculations. There appears to be little scope for reducing the cost of the time marching calculations further.

Some difficulties were encountered with the basic continuation strategy used which did not allow different branches on the stability curve to be traced automatically for the heavy case. Using information from the coarse grid the different branches of the solution were traced separately. Some work is required on this problem. However, it would be a lengthy business to map out the curve in all its detail using time marching.

The method has been developed with a view to generalisation. First, building the CFD-CSD equation into the iteration loop to compute non-symmetric problems is not likely to contribute greatly to the cost. The simplest approach is to iterate between the equilibrium calculation which provides a Jacobian matrix and the direct solver which provides the bifurcation parameter. The cost of this, especially since the previous equilibrium point can be used to restart the coupled static solution and the previous critical eigenvectors to restart the direct solution, is likely to be low. Secondly, incorporating a grid movement technique to account for deforming geometries is a small modification which is described in the next chapter. The extra Jacobian terms arising from the dependence of the fluid residual on the structural solution through the mesh deformation can be calculated by a combination of analytical terms and finite differences, although it has not been necessary to exploit this in the current chapter. Finally, the Krylov linear solver techniques are practical for three dimensional problems, and this extension will be reported in the next chapter.

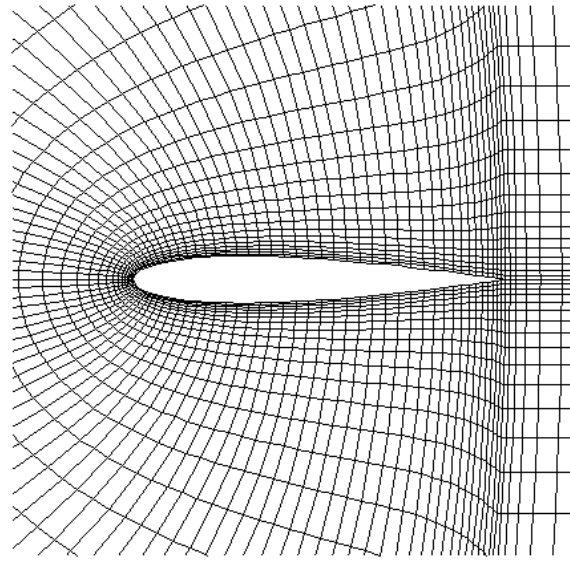


FIGURE 4.4: *Fine mesh for NACA0012 aerofoil*

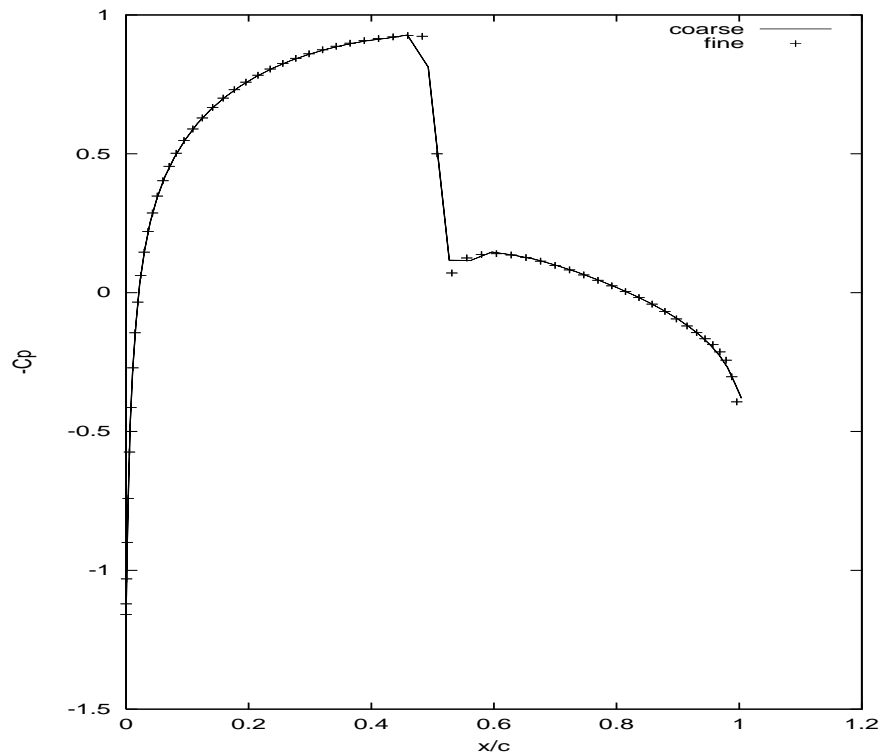


FIGURE 4.5: *Comparison of pressure distribution for NACA0012 aerofoil at zero incidence and $M_\infty = 0.8$ on the coarse and fine grids*

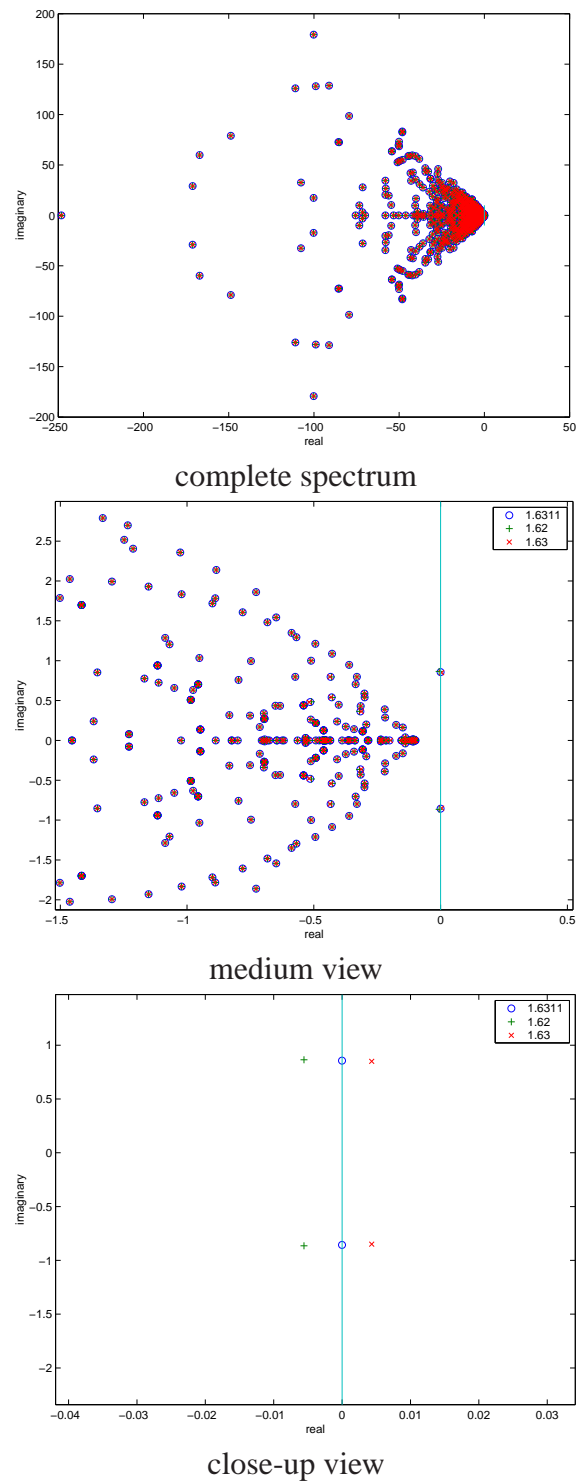


FIGURE 4.6: Eigenspectrum for quoted values of \bar{U} , the bifurcation parameter, on a very coarse grid at a Mach number of 0.5

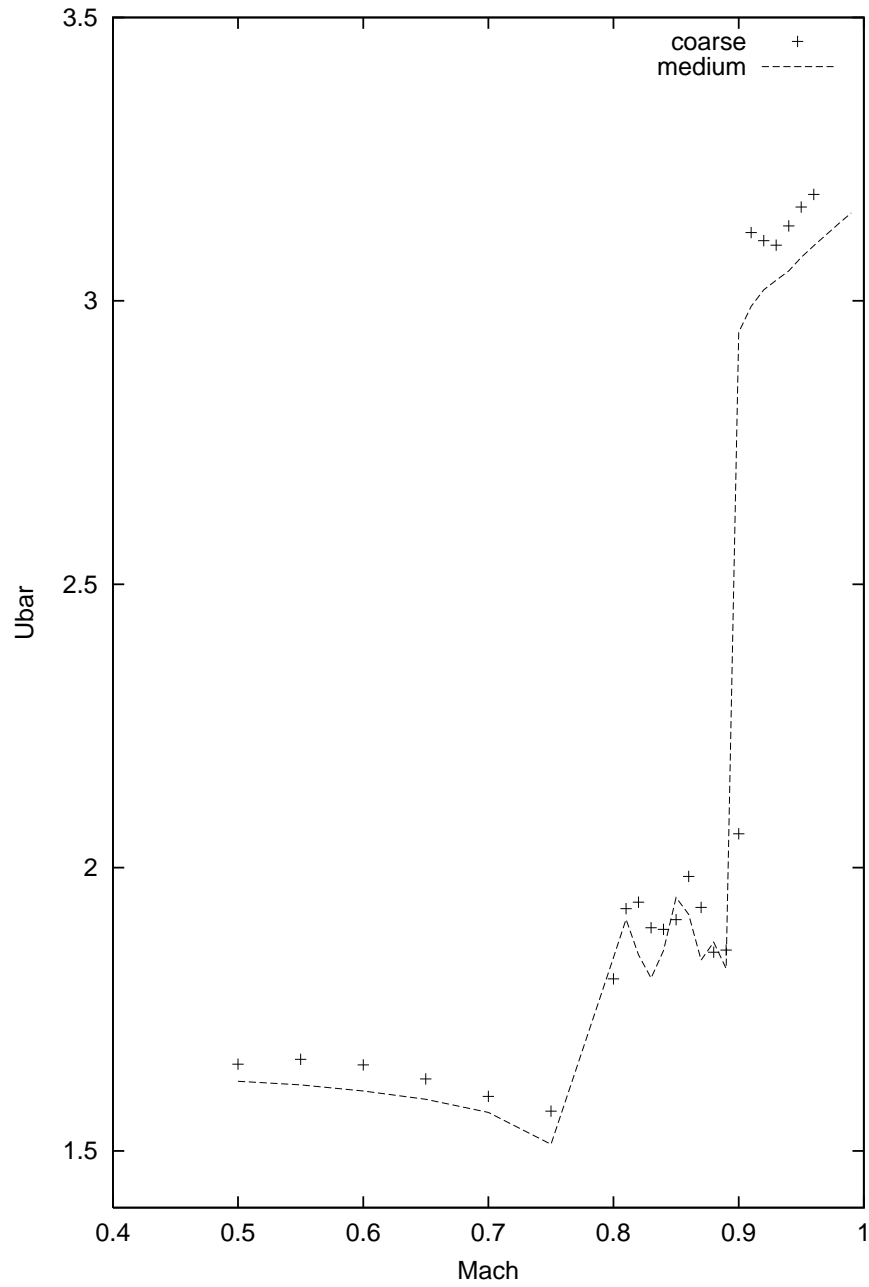
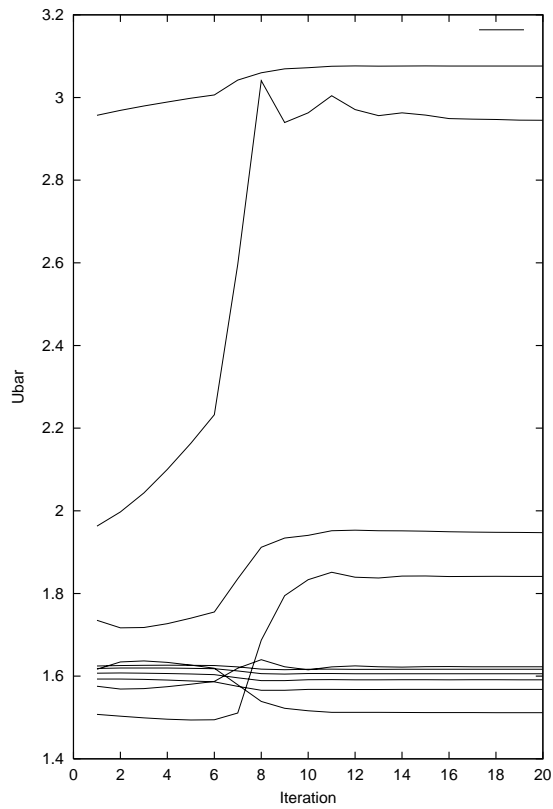
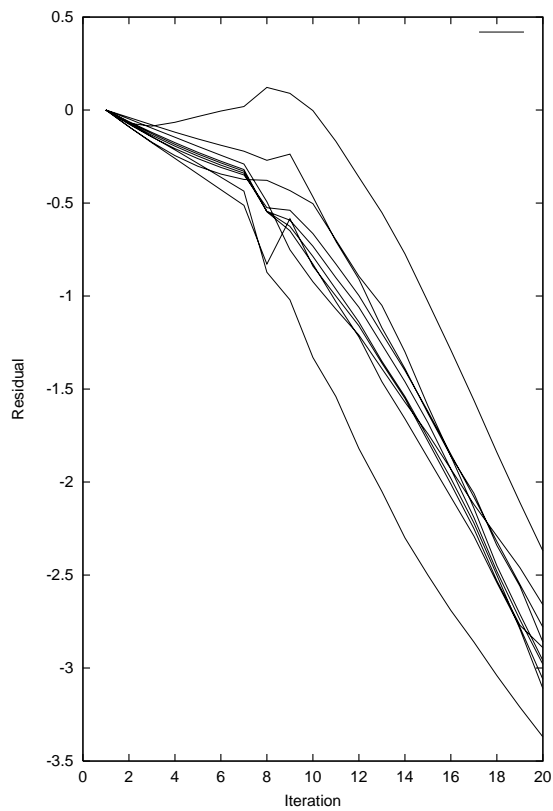


FIGURE 4.7: Comparison of stability boundaries for the light case on the coarse and medium grids



convergence of \bar{U}



convergence of residual

FIGURE 4.8: Convergence at different Mach numbers for the light case on the medium grid

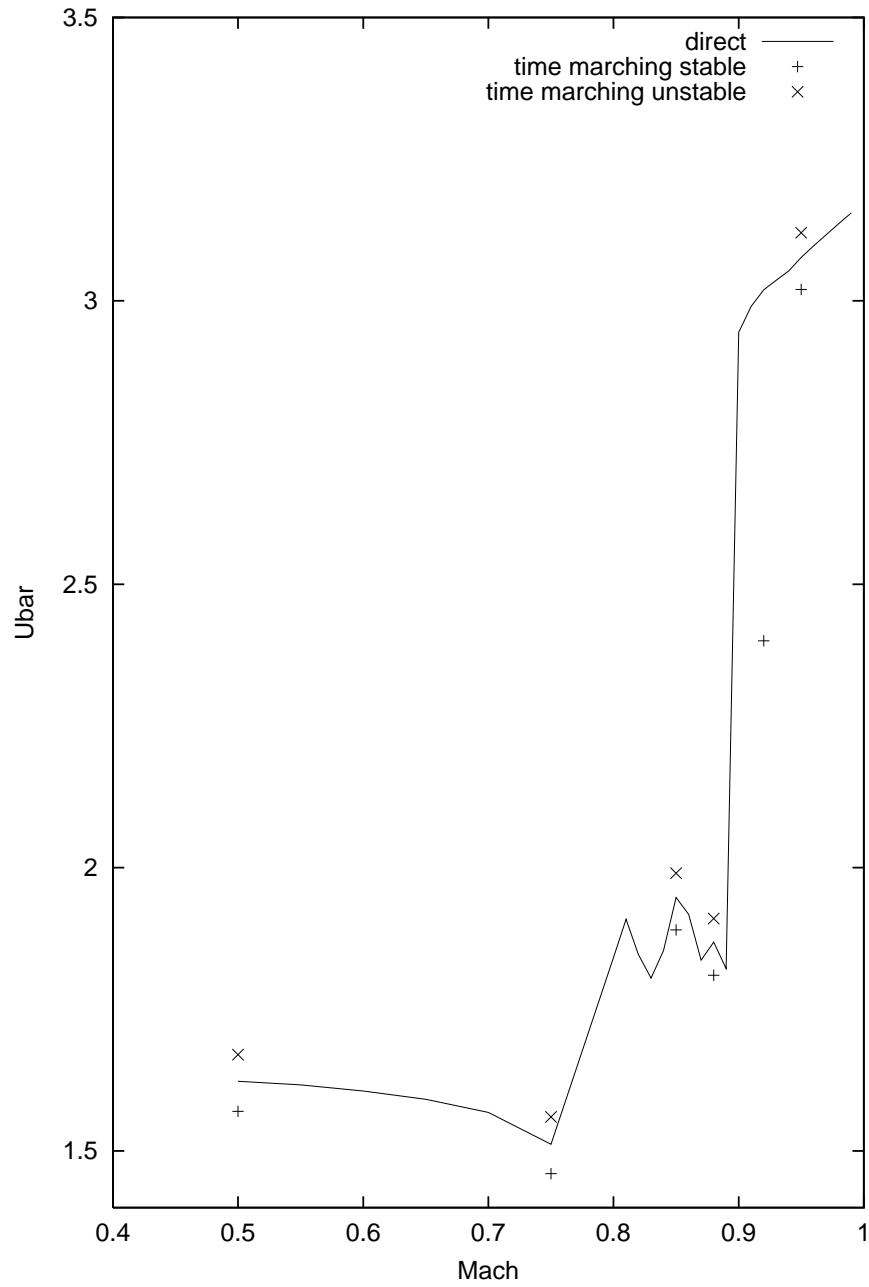


FIGURE 4.9: Comparison of stability boundary for the light case on the medium grids with time marching results

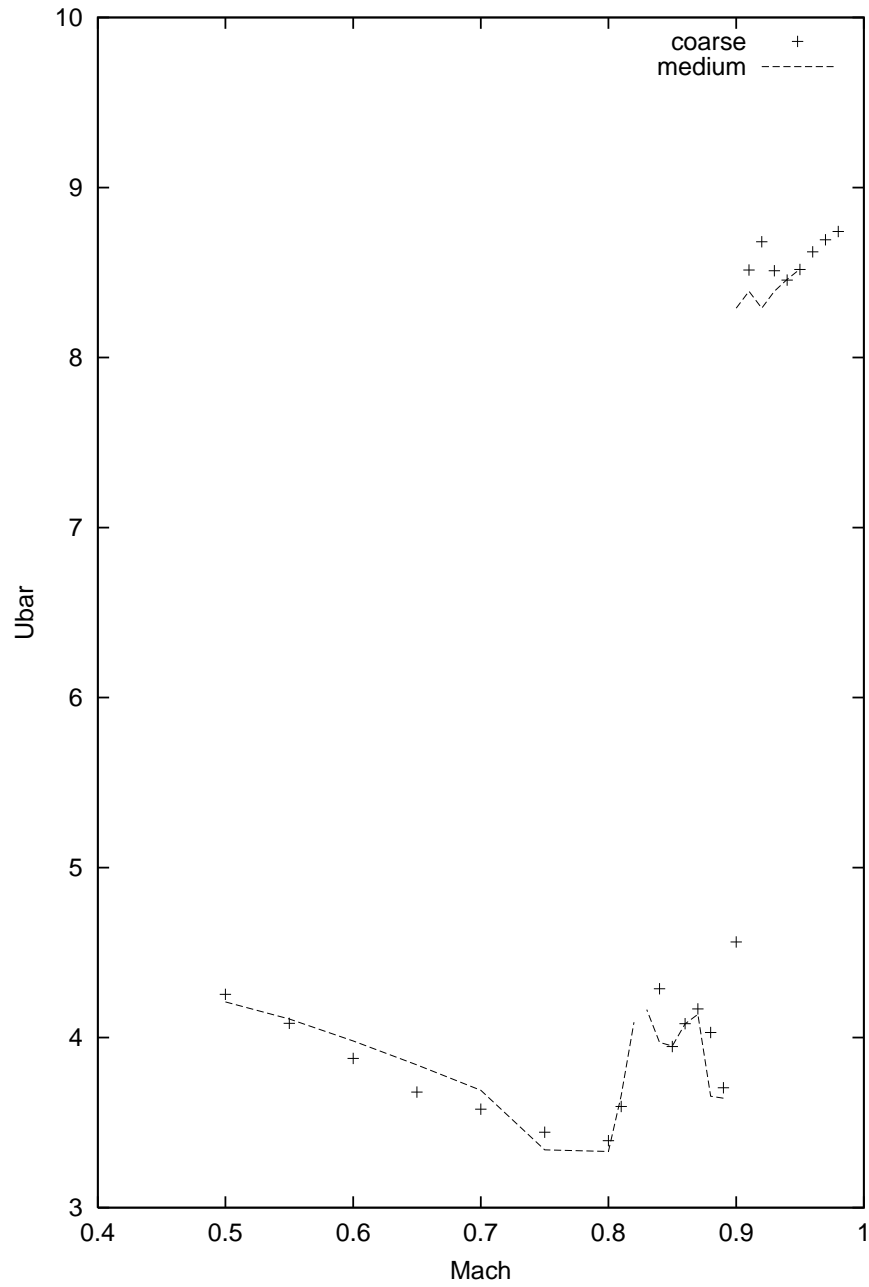


FIGURE 4.10: Comparison of stability boundaries for the heavy case on the coarse and medium grids

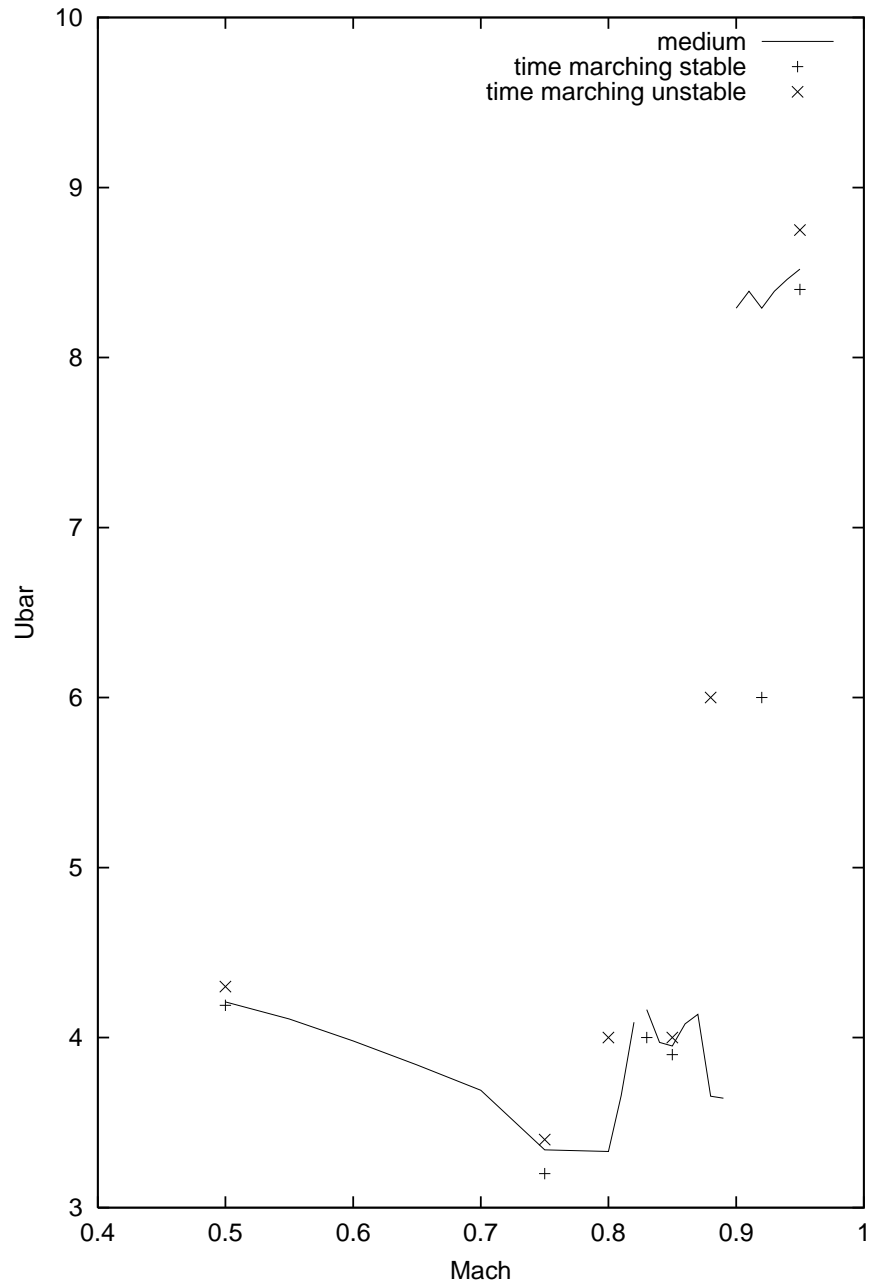


FIGURE 4.11: Comparison of stability boundary for the heavy case on the medium grids with time marching results

Chapter 5

Aeroelastic Stability Prediction for Wings

5.1 Introduction

This chapter extends the method to calculate flutter boundaries for wings. The additional issues to be considered are the treatment of a moving grid around a deforming geometry (as opposed to rigid motions for the aerofoil cases), the use of a modal structural model (instead of the pitch-plunge equations) and the resulting requirement to pass information between non-matching grids, and the larger problem size, and especially the impact of this on the solution of the linear system. The formulation is considered in the following two sections and then results are presented for the AGARD 445.6 wing test case ^[120] to demonstrate the feasibility of the method for three dimensional problems. The chapter finishes with the introduction to a new linear solver which can solve equations (3.26) and its application to symmetric and unsymmetric wings.

5.2 Aerodynamic and Structural Simulations

5.2.1 Aerodynamics

A strong conservation law form of the three-dimensional, time-dependent Euler equations for a perfect gas with conservative variables $\tilde{\mathbf{w}}_f = (\rho, \rho u, \rho v, \rho w, \rho E)^T$ and time-variant curvilinear coordinates (ξ, η, ζ, t) can be written in nondimen-

sional form as (Pulliam and Steger^[121]),

$$\frac{\partial \mathbf{w}_f}{\partial t} + \frac{\partial \mathbf{F}^i}{\partial \xi} + \frac{\partial \mathbf{G}^i}{\partial \eta} + \frac{\partial \mathbf{H}^i}{\partial \zeta} = 0 \quad (5.1)$$

where $\mathbf{w}_f = \tilde{\mathbf{w}}_f/J$. Here, $J = \xi_x \eta_y \zeta_z + \xi_y \eta_z \zeta_x + \xi_z \eta_x \zeta_y - \xi_z \eta_y \zeta_x - \xi_y \eta_x \zeta_z - \xi_x \eta_z \zeta_y$ is the determinant of the transformation. The flux vectors \mathbf{F}^i , \mathbf{G}^i and \mathbf{H}^i are,

$$\mathbf{F}^i = \frac{1}{J} \begin{pmatrix} \rho U \\ \rho u U + \xi_x p \\ \rho v U + \xi_y p \\ \rho w U + \xi_z p \\ (\rho E + p)U - \xi_t \end{pmatrix}, \quad (5.2)$$

$$\mathbf{G}^i = \frac{1}{J} \begin{pmatrix} \rho V \\ \rho u V + \eta_x p \\ \rho v V + \eta_y p \\ \rho w V + \eta_z p \\ (\rho E + p)V - \eta_t \end{pmatrix} \quad \mathbf{H}^i = \frac{1}{J} \begin{pmatrix} \rho W \\ \rho u W + \zeta_x p \\ \rho v W + \zeta_y p \\ \rho w W + \zeta_z p \\ (\rho E + p)W - \zeta_t \end{pmatrix}. \quad (5.3)$$

where the contravariant velocities along the ξ , η and ζ coordinates are defined as,

$$\begin{aligned} U &= \xi_x(u - x_g) + \xi_y(v - y_g) + \xi_z(w - z_g) \\ V &= \eta_x(u - x_g) + \eta_y(v - y_g) + \eta_z(w - z_g) \\ W &= \zeta_x(u - x_g) + \zeta_y(v - y_g) + \zeta_z(w - z_g). \end{aligned} \quad (5.4)$$

In the above ρ , u , v , w , p and E denote the density, the three Cartesian components of the velocity, the pressure and the specific total energy respectively and x_g , y_g and z_g are the local grid speeds in Cartesian coordinates.

The variables here have been non-dimensionalised with respect to the wing root chord c for x , y and z , the freestream velocity U_∞ for u , v and w , the freestream density ρ_∞ for ρ , U_∞/c for t and $\rho_\infty U_\infty^2$ for p .

5.2.2 Structural Dynamics, Inter-grid Transformation and Mesh Movement

The wing deflections $\delta \mathbf{x}_s$ are defined at a set of points \mathbf{x}_s by

$$\delta \mathbf{x}_s = \sum_{i=1}^M \alpha_i \phi_i \quad (5.5)$$

where ϕ_i are the mode shapes calculated from a full finite element model of the structure from the commercial FE package MSC/NASTRAN and α_i are the generalised coordinates. By projecting the finite element equations of motion of an elastic structure onto the mode shapes and assuming that the mode shapes have been scaled to give dimensional generalised masses $m_i = 1$, the modal equations of motion

$$\frac{d^2\alpha_i}{dt^2} + D_i \frac{d\alpha_i}{dt} + \omega_i^2 \alpha_i = \mu \phi_i^T \mathbf{f}_s \quad (5.6)$$

are obtained where \mathbf{f}_s is the vector of aerodynamic forces at the structural grid points and D_i is the coefficient of structural damping. Here a non-dimensionalisation consistent with the flow solver has been used. The bifurcation parameter $\mu = \rho_\infty / \rho_w$ in this case is a density ratio where ρ_w is the density of the wing structure. This parameter was chosen so flutter speed index vs Mach number graphs can be plotted. These equations are rewritten as a system in the form

$$\frac{d\mathbf{w}_s}{dt} = \mathbf{R}_s \quad (5.7)$$

where $\mathbf{w}_s = (\dots, \alpha_i, \dot{\alpha}_i, \dots)^T$ and $\mathbf{R}_s = (\dots, \dot{\alpha}_i, \mu \phi_i^T \mathbf{f}_s - \omega_i^2 \alpha_i - D_i \dot{\alpha}_i, \dots)^T$. This equation can be solved by a two stage Runge Kutta method, which requires a knowledge of \mathbf{f}_s^t and \mathbf{f}_s^{t+1} . To avoid introducing sequencing errors by approximating the value of \mathbf{f}_s^{t+1} , the Runge-Kutta solution is iterated in pseudo time along with the CFD solver, with the latest pseudo iterate being used to give a value for \mathbf{f}_s^{t+1} . At convergence the fluid and structural solvers are properly sequenced, at very little extra computational cost beyond what is required for the aerodynamic solution.

The aerodynamic forces are calculated at face centres on the aerodynamic surface grid. The problem of communicating these forces to the structural grid is complicated in the common situation that these grids not only do not match, but are also not even defined on the same surface. This problem, and the influence it can have on the aeroelastic response, was considered in Goura,^[122,123] where a method was developed, called the constant volume tetrahedron (CVT) transformation. This method uses a combination of projection of fluid points onto the structural grid, transformation of the projected point and recovery of the out-of-plane component to obtain a cheap but effective relation between deformations on the structural grid and those on the fluid grid. Denoting the fluid grid locations and aerodynamic forces as \mathbf{x}_a and \mathbf{f}_a , then

$$\delta \mathbf{x}_a = \mathcal{S}(\mathbf{x}_a, \mathbf{x}_s, \delta \mathbf{x}_s)$$

where \mathcal{S} denotes the relationship defined by CVT.^[122] In practice this equation is linearised to give

$$\delta \mathbf{x}_a = S(\mathbf{x}_a, \mathbf{x}_s) \delta \mathbf{x}_s$$

and then by the principle of virtual work, $\mathbf{f}_s = S^T \mathbf{f}_a$. The matrix S is called the spline matrix.

The grid speeds on the wing surface are also needed and these are approximated directly from the linearised transformation as

$$\delta \dot{\mathbf{x}}_a = S(\mathbf{x}_a, \mathbf{x}_s) \delta \dot{\mathbf{x}}_s$$

where the structural grid speeds are given by

$$\delta \dot{\mathbf{x}}_s = \Sigma \dot{\alpha}_i \phi_i. \quad (5.8)$$

The geometries of interest deform during the motion. This means that unlike the rigid aerofoil problem, the aerodynamic mesh must be deformed rather than rigidly translated and rotated. This is achieved using transfinite interpolation of displacements^[124] (TFI) within the blocks containing the wing. More elaborate treatments which move blocks to maintain grid orthogonality are possible^[37] but are not necessary here because only small wing deflections are encountered and the blocks in the mesh can be extended well away from the wing. The wing surface deflections are interpolated to the volume grid points \mathbf{x}_{ijk} as

$$\delta \mathbf{x}_{ijk} = \psi_j^0 \delta \mathbf{x}_{a,ik} \quad (5.9)$$

where ψ_j^0 are values of a blending function^[124] which varies between one at the wing surface (here $j=1$) and zero at the block face opposite. The surface deflections $\mathbf{x}_{a,ik}$ are obtained from the transformation of the deflections on the structural grid and so ultimately depend on the values of α_i . The grid speeds can be obtained by differentiating equation (5.9) to obtain

$$\delta \dot{\mathbf{x}}_{ijk} = \psi_j^0 \delta \dot{\mathbf{x}}_{a,ik}. \quad (5.10)$$

The surface velocities $\dot{\mathbf{x}}_{a,ik}$ are obtained from the transformation of the velocities on the structural grid in exactly the same way the deflections were above and so ultimately depend on the values of $\dot{\alpha}_i$.

5.3 Formulation of Augmented Solver

The augmented solver is set up in an analogous way to the two-dimensional case shown in section 4.3. Here the structural unknowns \mathbf{w}_s and structural residual \mathbf{R}_s are associated with the modal equations (5.6). The Jacobian matrix A is partitioned as in equation (4.18).

The block A_{ff} describes the influence of the fluid unknowns on the fluid residual and has by far the largest number of non zeros entries when a modal structural model is used and is calculated in an analogous way to the two-dimensional case in section 4.3.

The dependence of the fluid residual on the structural unknowns α_i and $\dot{\alpha}_i$ is partially hidden by the notation used. The fluid residual depends not only on the fluid cell values but also on the location of the grid points themselves and the cell volumes. The fluid and structural unknowns are independent variables and hence to calculate the term A_{fs} the fluid unknowns are kept fixed. The influence of the structural unknowns is felt through the moving grid. Using the modal structural model, the updated grid locations and speeds are calculated by moving the structural grid according to the values of the generalised coordinates and velocities, transferring these to the fluid surface grid using the transformation and then applying TFI to transfer these boundary values to the volume grid. As with in two-dimensional case second order finite differences, the terms in A_{fs} can be calculated in $2n_s$ evaluations of the aerodynamic residual if there are n_s structural unknowns.

The term A_{sf} involves calculating the dependence of the generalised fluid forces on the fluid unknowns. The surface forces on the aerodynamic grid are calculated and then transferred to the structural grid using the transformation. The inner product is then formed using the forces on the structural grid and the modal coefficients. The Jacobian matrix for the forces on the structural grid with respect to the fluid unknowns $\partial \mathbf{f}_s / \partial \mathbf{w}_f$ can be calculated analytically since \mathbf{f}_s is a linear combination of \mathbf{f}_a . Then the required terms for A_{sf} can be calculated through

$$A_{sf} = \frac{\partial \mathbf{R}_s}{\partial \mathbf{w}_f} = \begin{bmatrix} \vdots \\ 0 \\ \boldsymbol{\varphi} \boldsymbol{\phi}_i^T \partial \mathbf{f}_s / \partial \mathbf{w}_f \\ \vdots \end{bmatrix}.$$

When calculating the term A_{ss} it is important to remember that the generalised

force will change with the structural unknowns since the surface normals to the wing will change as the wing moves. A second-order finite difference calculation is used to include this effect.

The bifurcation parameter μ only appears in the structural equations. Therefore,

$$A_\mu = \begin{bmatrix} 0 & 0 \\ 0 & \frac{\partial^2 \mathbf{R}_s}{\partial \mu \partial \mathbf{w}_s} \end{bmatrix} \quad (5.11)$$

Due to the simple algebraic expression for $\partial \mathbf{R}_s / \partial \mathbf{w}_s$ it is straightforward to calculate the required term analytically.

5.4 Results for Symmetric Problem

5.4.1 Test Case

An important problem with the development of aeroelastic simulation tools is the lack of experimental data available for assessment. The experiments are intrinsically destructive and require careful model construction to ensure proper scaling, and hence the expense is much higher than rigid model tests. A complete set of measurements is available for the AGARD 445.6 wing and results have been included in most papers on computational aeroelasticity, giving a wide range of data to evaluate the current method. However, a disadvantage of this test case is that it does not feature significant non-linear aerodynamic effects since the wing is thin. Despite this, it is the first test case commonly used to test time marching codes and is suitable for the current work because it is symmetric. Previous time marching results are reviewed in reference.^[113]

The AGARD 445.6 wing^[120] is made of mahogany and has a 45° quarter chord sweep, a root chord of 22.96 inches and a constant NACA64A004 symmetric profile. A series of flutter tests, which were carried out at the NASA Langley transonic dynamics tunnel to determine stability characteristics, was reported in 1963. Various wing models were tested (and broken). The case for which most published results have appeared is the weakened wing (wing 3) in air. This wing had holes drilled out which were filled with plastic to maintain the aerodynamic shape whilst being structurally weaker. Published experimental data includes the dynamic conditions at which the wing was viewed to be unstable for Mach numbers in the range

0.338 to 1.141. The structural characteristics of the wing were provided in the form of measured natural frequencies and mode shapes derived from a finite element model. Full details of the structural model used are given in Goura's thesis.^[122] Four modes are retained with the first two bending modes having frequencies of 9.7 and 50.3Hz, and the two torsional modes of 36.9 and 90.0Hz.

A problem with the published results for the AGARD 445.6 wing is that most are of a demonstration nature in the sense that verification is hardly ever shown. There is a significant spread of the results obtained when using solutions of the Euler equations. The results which cluster around the measured data in the region of the flutter dip tend to be on coarser grids, with finer CFD grids generally giving lower flutter speeds. The only published attempt at a systematic grid refinement study was shown in reference.^[125] In this commendable study the fine and medium grid results were further apart than those on the medium and coarse grids and hence grid independence was not achieved, casting doubt on other published results on coarser grids. The main obstacle to a rigorous study is of course the cost of the calculations. A second question mark against the published results is that in the majority of cases no structural damping was used. In the description of the experiment a value of 2% is suggested^[120] although it is not clear how certain this value is.

5.4.2 Time Marching Solutions

An attempt was made to perform a detailed grid convergence study within the limits of the computers available. All calculations reported in this section were done with the PMB code. To optimise the grid used, two requirements were identified. First, since the calculations are inviscid, and hence no wake needs to be preserved, an O-grid was used which helps to maximise the number of grid points on the surface of the wing. A genuine multiblock topology was used to allow a good quality mesh to be preserved in the tip leading and trailing edge regions as shown in figure 5.1. Secondly, the important quantities which must be well predicted for the flutter calculations are the generalised modal forces. The pressure difference between the upper and lower surface therefore must be predicted accurately. The flutter response is dominated by the first bending mode which features some twist near the tip but is essentially a plunging motion near the root. The significant pressure difference, and following from this the main contribution to the generalised force, comes from

the region towards the wing tip. The grid points were therefore concentrated in this region. Most structured grids shown in the literature have been of the C-H topology and are reasonably uniform in the spanwise direction.

The finest grid in the current work has 1.43 million points, and 17700 on the wing surface. Medium and coarse grids were extracted from this which have 190 thousand and 27 thousand points respectively, with 4453 and 1131 points on the wing surface. The number of volume points used in the refinement study of reference [125], where the fine, medium and coarse grids have 2.1 million, 901 thousand and 274 thousand points respectively, is comparable to the current grids but significantly the number of surface points is less (9231, 5343 and 2366 respectively). It is stressed however that the topology in the current study would not be ideal for RANS calculations which were the main focus of [125]. Comparison is also made with the structured [21] and unstructured [19] studies by Batina and co-workers. The structured grid has 517 thousand points with 5289 on the wing surface. The unstructured grid has 129 thousand tetrahedra and, although no information is given about the number of points on the wing surface, the pictures shown in the paper suggest that the grid points are more strongly clustered in the wing region than is possible for structured grids.

A number of tests using the medium grid were made on the temporal parameters (time step and convergence level) at a Mach number of 0.96, a freestream velocity of 308 m/s, a density of 0.08 kg/m^3 and structural damping of 0.5%. First, the responses when using 10 or 20 pseudo steps per real time step were identical, indicating that 10 steps was more than adequate. Secondly, using a reduced time step of 0.01 and 0.02 also gave an identical response and hence the larger time step is adequate.

The influence of grid resolution is harder to test due to the calculation cost on the density of grids that are required. The three grid levels were used to locate the flutter point for a range of Mach numbers. Two calculations were run at different values of freestream density for each Mach number and the growth of the response calculated using the approach of [125] where the ratio of consecutive peaks was taken to define an amplification factor. Linear interpolation of the amplification was then used to estimate the value of density at which a neutrally stable response would be obtained. The medium grid calculations took about 5-6 hours on a 2.5 GHz PC to calculate 5 periods of the flutter response.

The comparison at Mach 0.96, which is close to the bottom of the flutter dip, between the predicted flutter speeds on the three grid levels with other predictions is shown in table 5.1. The results of [125] show a downward (and accelerating) trend in the flutter speed, with bigger differences between the fine and medium than between the medium and coarse. The value from [19] is lower still. The current results suggest that the medium grid provides good spatial resolution, with the 3 grids showing behaviour consistent with spatial convergence. The grid converged value using no structural damping is much lower than experiment. Using a value of structural damping of 2% shifts the flutter speed index above the experimental value.

The trends from these results suggest that the grid converged solution without structural damping is significantly below the experimental result. Adding structural damping brings the flutter speed back up into the range of the measurements, as shown in figure 5.2. The solution obtained using 0.5% structural damping is in good agreement with the experimental values.

5.4.3 Augmented Solver Results

The augmented solver was applied on the coarse and medium grids. The medium grid is the largest problem which can be tackled on the computers which were available. This case requires 1.5 Gb of memory. CPU time comparisons between the augmented and time marching calculation costs are expressed as multiples of the CPU time required for a steady-state calculation with the same code. The timings are likely to be conservative when assessing the performance of the augmented solver because additional gains are likely from writing a dedicated linear solver (i.e. one which is not configured to handle general sized matrix blocks).

Guided by the time marching results, a value of structural damping of 0.5% was used. The comparison on the medium grid between the measured, time marching and bifurcation results is shown for the dip region in figure 5.3. The bifurcation boundary was computed first for eight Mach numbers between 1.07 and 0.67, with a Mach number interval of 0.05, and subsequently for 12 Mach numbers in the dip region, with an interval of 0.01. The frequency from the time marching calculations was used with the inverse power method at the largest Mach number to initiate the calculations. Good agreement between the predictions of the two codes is observed as required.

An assessment of the relative cost of the time marching and bifurcation calculations can be made from the times in table 5.2. Here the average CPU time of an unsteady calculation and the average bifurcation cost for each Mach number have been expressed in multiples of the cost of a steady state calculation using the respective codes. The steady state calculation in each case has been converged 5 orders of magnitude. The augmented solver has been converged to at least 3 significant figures for the flutter speed, as indicated in figure 5.4. The stopping criterion is based on reducing the magnitude of the augmented residual, defined by equation (4.13), by one order from the starting value. The time for the unsteady calculations is based on 750 time steps resolving 5 cycles.

Similar conclusions to the previous aerofoil study shown in chapter 4 can be drawn. The time required to trace out the flutter boundary for 10 Mach numbers is about half the cost of a single time marching calculation. Considering the number of time marching calculations required to trace out a flutter boundary, the calculation cost can be reduced by 2 orders of magnitude by using the bifurcation method.

One concern was that the performance of the linear solver would deteriorate for larger problems. On average for the aerofoil 30 iterations were required to achieve a reduction of two orders in the residual. The number of linear solver iterations at each bifurcation iteration is shown in the scatter plot in figure 5.5 along with the average number of iterations required for the previous aerofoil calculations. The fact that the number of linear solver iterations is spread about the average two-dimensional cost indicates that the performance of the Krylov solver has been maintained for the larger three-dimensional problems.

5.5 Formulation of a Dedicated Linear Solver

The linear solver in the Aztec package which has been used to generate all results to date. As a test case we use the system $C\mathbf{x} = \mathbf{b}$ where

$$C = \begin{bmatrix} A & I\omega \\ -I\omega & A \end{bmatrix}. \quad (5.12)$$

Here A is Jacobian matrix of the CFD equations plus the CSD equations. This system is used in the inverse power iterations and is close to that used for the augmented solver.

Reference	Grid Volume	Grid Surface	Damping	Flutter Speed Index
Current	Coarse	1131	0	0.227
Current	Medium	4453	0	0.192
Current	Fine	17700	0	0.175
Current	Coarse	1131	2%	0.401
Current	Medium	4453	2%	0.381
Current	Fine	17700	2%	0.375
[125]	Coarse	2366	0	0.314
[125]	Medium	5340	0	0.304
[125]	Fine	9231	0	0.285
[19]	Unstructured	N/A	0	0.230
[21]	Structured	5289	0	0.294

TABLE 5.1: *Grid Refinement Influence on Flutter Speed Index at Mach 0.96*

Calculation Type	CPU (sec)	CPU (relative)
steady state	787	1
unsteady solution	19810	45
steady calculation	1767	1
bifurcation calculation	3304	1.87

TABLE 5.2: *Average calculation cost using the PMB code for the first two rows and the augmented solver for the bottom two rows in the table. The relative costs have been scaled by the time for a steady-state calculation with the appropriate code*

The following conclusions were drawn for the solution of the linear system with Aztec in section (4.4):

- The augmented linear systems are significantly more difficult to solve than CFD only systems.
- The second-order Jacobians cannot be solved with zero fill-in preconditioners whereas the approximate first-order Jacobians can.

The removal of both these are performance restrictions would be useful for two reasons. Firstly the linear systems in (3.26) require the solution of systems with second-order Jacobians. Having to use non zero fill-in preconditioners in 3D would limit the potential problem size greatly. Secondly it would be possible to use the ideas of indirect calculation shown in section 2.5.1. Indeed the behaviour of the real part of the critical eigenvalue below and above the Hopf bifurcation point would allow graphs of damping vs speed to be produced.

To facilitate easy testing of various options, an implementation of a Krylov method with BILU preconditioning was written in MATLAB. A general version of the preconditioning was written which allows various levels of fill-in.

5.5.1 Generalized Conjugate Residual

Eisenstat, Elman and Schultz^[126] developed a generalized conjugate gradient method that depends only on A rather than $A^T A$ and is called the generalized conjugate residual (GCR) algorithm. Saad and Schultz developed the Generalized Minimal Residual (GMRES) algorithm which is mathematically equivalent to GCR but is less prone to breakdown for certain problems, requires less storage and arithmetic operations. However GCR remains the easier algorithm to implement especially in parallel, and is given as

$$\begin{aligned}
 r_0 &= b - Cx_0 \\
 p_0 &= r_0 \\
 \text{For } j &= 0, 1, 2, \dots, \text{ until convergence. Do:} \\
 \alpha_j &= \frac{\langle r_j, Cp_j \rangle}{\langle Cp_j, Cp_j \rangle} \\
 x_{j+1} &= x_j + \alpha_j p_j \\
 r_{j+1} &= r_j - \alpha_j Cp_j \\
 \beta_{ij} &= -\frac{\langle Cr_{j+1}, Cp_i \rangle}{\langle Cp_i, Cp_i \rangle}, \text{ for } i = 0, 1, 2, \dots, j \\
 p_{j+1} &= r_{j+1} + \sum_{i=0}^j \beta_{ij} p_i
 \end{aligned} \tag{5.13}$$

Enddo

To calculate the β_{ij} the vector Cr_j and the previous Cp_j 's are required. The number of matrix vector products per step can be reduced to one if Cp_{j+1} is calculated by

$$Cp_{j+1} = Cr_{j+1} + \sum_{i=0}^j \beta_{ij} Cp_i \tag{5.14}$$

This may not be beneficial if C is sparse and j is large.

A restarted version called GCR(m) is defined so that when the iteration reaches step m all the p_j 's and Cp_j 's are thrown away. Techniques have been proposed to include approximate eigen-components in later restarts for GMRES^[127] and these techniques and similar strategies may help GCR also.

5.5.2 Block Incomplete Lower Upper Factorisation

For the block incomplete lower upper (BILU) factorisation the matrix is partitioned into 5×5 matrix blocks associated with each cell in the mesh. The use of this blocking reduces the memory required to store the matrix in a sparse matrix format. For the clarity of the rest of this section the block part will now be dropped.

Consider a general sparse matrix C whose elements are c_{ij} , $i, j = 1, \dots, n$. A general incomplete factorisation process computes a sparse lower triangular matrix L and a sparse upper triangular matrix U so the residual matrix $R = LU - C$ satisfies certain constraints, such as having entries in some locations. A common constraint consists of taking the zero pattern of the L U factors to be precisely the zero pattern of A . However the accuracy of the ILU(0) factorisation may be insufficient to provide an adequate rate of convergence.

More accurate incomplete LU factorisations allowing extra terms to be filled into the factorisation are often more efficient as well as more robust. Consider updating the c_{ij} element in full Gaussian elimination (GE) the inner loop contains the equation

$$c_{ij} = c_{ij} - c_{ik}c_{kj}. \quad (5.15)$$

If lev_{ij} is the current level of element c_{ij} then the new level is defined to be

$$\text{lev}_{ij} = \min(\text{lev}_{ij}, \text{lev}_{ik} + \text{lev}_{kj} + 1). \quad (5.16)$$

The initial level of fill for an element c_{ij} of a sparse matrix C is 0 if $c_{ij} \neq 0$ and ∞ otherwise. Each time an element is modified in the GE process its level of fill is updated by equation 5.16. Observe that the level of fill of an element will never increase during the elimination. Thus if $c_{ij} \neq 0$ in the original matrix A , then the element will have a level of fill equal to zero throughout the elimination process. The above gives a systematic way of discarding elements. Hence ILU(k) contains all of the fill in elements whose level of fill does not exceed k .

For all non zero elements c_{ij} define $\text{lev } c_{ij} = 0$
 For $i = 2, \dots, n$ Do:
 For $j = 1, 2, \dots, i - 1$ and for $\text{lev } a_{ij} < k$
 $c_{ij} = c_{ij}/c_{jj}$
 $c_{il} = c_{il} - c_{ij}c_{jl} \quad l = j + 1, \dots, n$ (5.17)
 Update the levels of fill in for non zero c_{ij}
 EndDo
 If $\text{lev } c_{ij} > k$ then $c_{ij} = 0$
 EndDo

5.5.3 Real and Complex Variable Formulations

Section 4.2 used a real variable formulation with the test matrix written as

$$C = \begin{bmatrix} A_{ff} & A_{fs} & \omega I & 0 \\ A_{sf} & A_{ss} & 0 & \omega I \\ -\omega I & 0 & A_{ff} & A_{fs} \\ 0 & -\omega I & A_{sf} & A_{ss} \end{bmatrix}. \quad (5.18)$$

However this form has increased the bandwidth of the matrix C . A different approach would be to maintain the matrix in complex variables

$$C_c = \begin{bmatrix} A_{ff} & A_{fs} \\ A_{sf} & A_{ss} \end{bmatrix} - i\omega \begin{bmatrix} I & 0 \\ 0 & I \end{bmatrix}. \quad (5.19)$$

There are several ways to approximate the matrices C and C_c before the incomplete factorisation is applied. These approximations only effect the rate of convergence of the linear solver and not the solution if the original matrix is used in the linear solver. Three possible methods were considered with increasing number of elements removed from the preconditioner.

Method 1

This is standard BILU(k) on the complete real C or complex matrix C_c .

Method 2

This is BILU(k) on the block diagonal of either C_c or C i.e.

$$C_c^{(2)} = \begin{bmatrix} A_{ff} & 0 \\ 0 & A_{ss} \end{bmatrix} - i\omega \begin{bmatrix} I & 0 \\ 0 & I \end{bmatrix} \quad (5.20)$$

and

$$C^{(2)} = \begin{bmatrix} A_{ff} & 0 & 0 & 0 \\ 0 & A_{ss} & 0 & 0 \\ 0 & 0 & A_{ff} & 0 \\ 0 & 0 & 0 & A_{ss} \end{bmatrix}. \quad (5.21)$$

Method 3

This extends the blocking in Method 2 by also including the blocking of the multi-block grid. This means A_{ff} loses all its inter block connectivity following the method used in the CFD only solver^[36].

5.5.4 Results

Table 5.3 shows the number of non-zero 5×5 blocks required for the different methods with a modified-order Jacobian. Each complex block requires twice the storage of a real block due to the real and imaginary parts. Even taking this into account the complex formulation always uses less memory than the real one. Also the scaling of the memory requirements is much less for the complex formulation as the level of fill-in increases. The real formulation of method 2 results in a singular preconditioner if A_{ss} is singular.

Table 5.4 shows the number of non-zero 5×5 blocks required for the different methods with a second-order Jacobian. Comparing them with the modified order Jacobian with level 3 fill in the second-order Jacobian requires 4 to 5 times the storage. However there is a much larger decrease in storage requirements as terms in the preconditioner are removed compared to the modified order case.

Method	Real or Complex	Number of Non Zeros 5×5 Blocks			
		BILU(0)	BILU(1)	BILU(2)	BILU(3)
1	Real	396518	806558	1590985	N/A
1	Complex	175854	304151	511390	902146
2	Complex	151667	278915	485085	874617
3	Complex	141603	247315	402803	689403

TABLE 5.3: *Table of the number of non zero in the preconditioner for the modified order Jacobian*

The test problem is derived from the AGARD 445.6 wing with 13,000 cells at Mach 0.67 with ω fixed at 0.28. This value was used as it is a good approximation

Method	Real or Complex	Number of Non Zeros 5×5 Blocks BILU(3)
1	Complex	4273227
2	Complex	4241749
3	Complex	2741219

TABLE 5.4: *Table of the number of non zero in the preconditioner for the second order Jacobian*

to the correct value of ω at bifurcation for both the modified and second order systems. All the methods are used a restart size of 60.

Figure 5.6 shows the differences between the first two methods using both real and complex versions of the preconditioner with a modified order Jacobian matrix. The performance drop from switching from method 1 to method 2 in the complex case is smaller. This is thought to be because, in effect, the complex case retains some of the off-diagonal terms that are removed in the real case.

Figure 5.7 shows the differences between the first two methods using both real and complex versions of the preconditioner with a second-order Jacobian matrix. It is clear than the second-order Jacobian system is much harder to converge than the modified order system. However the lack of performance decrease from switching from method 1 to method 2 when using a complex preconditioner is still valid. The use of method 3 improves the convergence rate of the linear solve so even though the off-diagonal terms were using more fill-in on the diagonal blocks still has advantages.

Figure 5.8 shows the differences for all 5 methods with the complex preconditioner and a second-order Jacobian. It is clear that removing the connectivity has degraded performance of the linear solver although convergence is still obtained.

The complex formulation of the preconditioner requires less storage and preconditions the linear system better than the real formulation. With the dedicated linear solver and this preconditioner the second-order Jacobian can now be solved, opening up the possibility of finding the eigenvalue of smallest real part of this matrix directly using the inverse power method.

5.6 Symmetric case: AGARD Wing

In section 5.4.3 the prediction of the flutter boundary by the augmented solver, using the Jacobian of the first-order scheme to drive the (approximate) Newton method, was compared with time domain predictions, which were in perfect agreement. A detailed grid refinement study was undertaken and for the first time grid converged solutions were published. The issue of the influence of structural damping on the solution in the dip at Mach 0.97 was considered in detail. Finally, comparison with other published results, including measurements, was made.

With the new dedicated linear solver the behaviour of the augmented solver when using the full Newton's method, and the inverse power method, are considered. These investigations are made possible by the availability of the Jacobian matrix of the second-order spatial scheme from section 4.3. The grid used is the coarse grid discussed above.

The convergence of the flutter speed index at Mach 0.97 is shown in figure 5.9. Rapid convergence is obtained through quadratic convergence of Newton's method, with the critical value being obtained in 3 iterations. The inverse power method was used to trace out the values of the aeroelastic eigenvalues, which are associated with the structural modes, as a function of dynamic pressure $q = 0.5\rho V^2$. The real and imaginary parts are shown in figure 5.10. The critical dynamic pressure, which is when the real part of an eigenvalue goes positive, agrees with the value from the direct calculation.

5.7 Asymmetric case: MDO Wing

The MDO wing is a commercial transport wing, with a span of 36 metres, designed to fly in the transonic regime ^[128,129]. The profile is a thick supercritical section. The structure is modelled as a wing box running down the central portion of the wing. The structural model consists of 8 modes between 0.88 and 14.97 Hz. This case has a non-symmetric section and so the static solution is dependent on the dynamic pressure, in contrast to the AGARD and Goland cases. The inverse power method is used below to map out the behaviour of the eigenspectrum with and without the effect of the static deflection. The grid has 22,000 points (110,000 degrees of freedom) and was derived by extracting points from a finer grid that

has 600,000 points. Steady calculations on both grids confirmed that the aerostatic solution and the flow topology obtained, which at Mach 0.85 is a upward bending and nose down twisting at the wing tip, and a strong shock towards the trailing edge which is weakened by the deflection, are similar on both grids, although the coarse grid solution has a more diffuse suction peak and shock.

This case introduces a new issue compared with the AGARD wing in that the MDO wing has a significant static deflection. This makes the inverse power method preferable to calculate the flutter point since this method can naturally take into account the static deformation. The real and imaginary parts of the eigenvalues of the aeroelastic system are plotted in figure 5.11 where no static deflection is allowed (that is the equilibrium solution is taken about the rigid wing). The dynamic pressure at which the second mode becomes undamped is $28594 \text{ kg}/(\text{ms}^2)$. The equivalent plot when a static deflection is allowed looks very similar except that the crossing of the second mode happens at $58097 \text{ kg}/(\text{ms}^2)$ i.e. the effect of the static deflection is to increase the critical dynamic pressure. The reason for this is clear from figure 5.12 where, as would be expected, the influence of the aerostatic deflection is to bend the wing up and twist it nose down at the wing tip, as shown in the figure. This weakens the shock, which is likely to be stabilising for the dynamic behaviour. What is important here is that this aerostatic effect is taken into account naturally by the inverse power method, since the Jacobian used is computed at the correct static solution for a given dynamic pressure.

5.8 Conclusions

The performance of the augmented solver and inverse power method for calculating flutter boundaries has been evaluated for the AGARD 445.6 wing test case. This is the first time that such an augmented solver has been used to calculate a three-dimensional aeroelastic instability problem. The good performance of the method previously observed for aerofoil problems has been preserved. In particular the cost of the iterative linear solver in terms of the number of iterations required has not increased as the size of the matrix has increased. It is estimated that the cost of tracing out a flutter boundary over ten Mach numbers has been reduced by 2 orders of magnitude compared with the time marching method.

The augmented solver presented relied on the system being symmetric which

means that the equilibrium solution is independent of the bifurcation parameter. In the asymmetric case the equilibrium solution has to be recalculated as the bifurcation parameter is updated during the Newton iterations. However the approach considered here for the asymmetric The MDO wing was the calculation of the structural eigenvalues from the Jacobian matrix via the inverse power method, and included the effect of a static deflection.

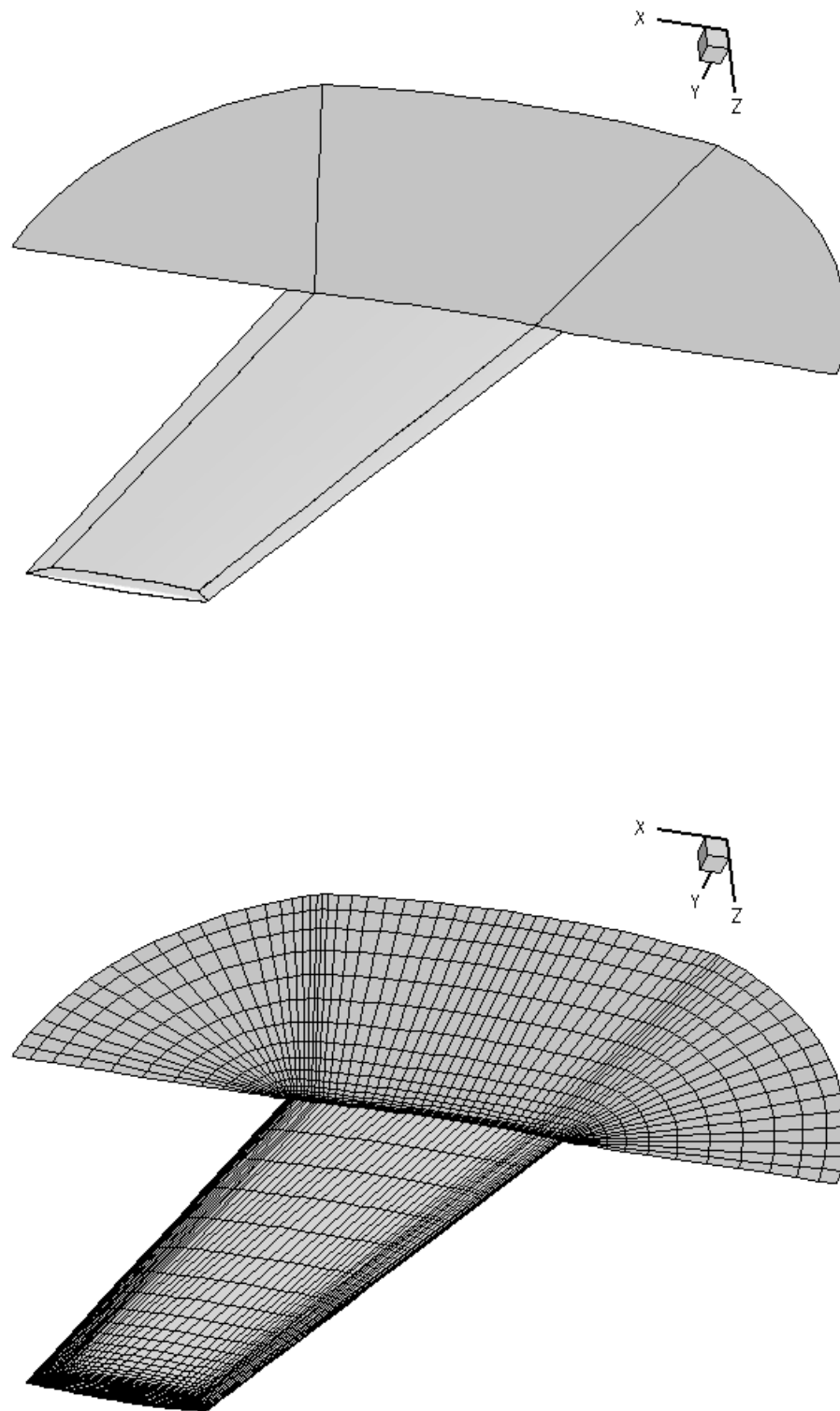


FIGURE 5.1: *Grid topology (above) and medium surface mesh (below). Note that only the inner blocks above the wing are shown on the symmetry plane*

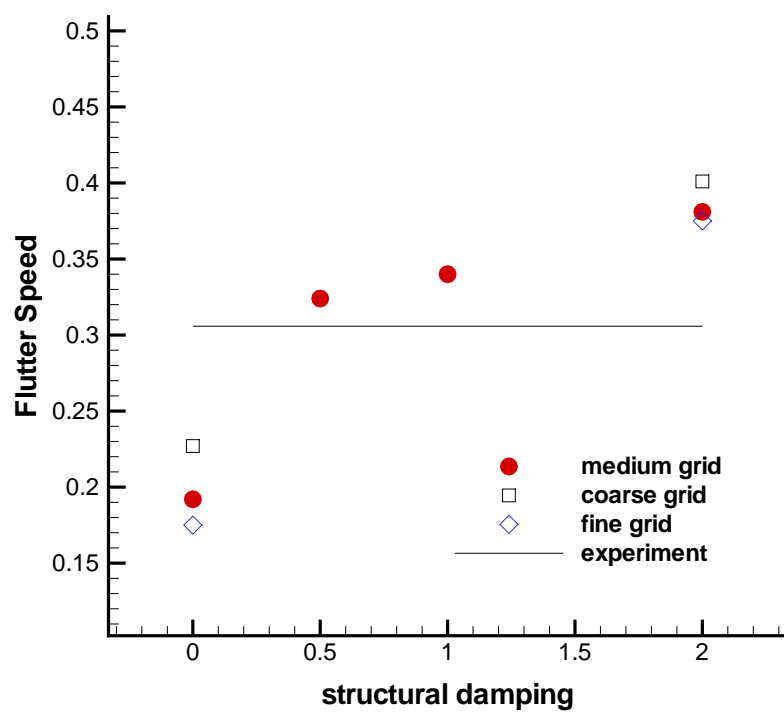


FIGURE 5.2: The variation of flutter speed index with the structural damping applied at Mach 0.96. The line indicates the measurement

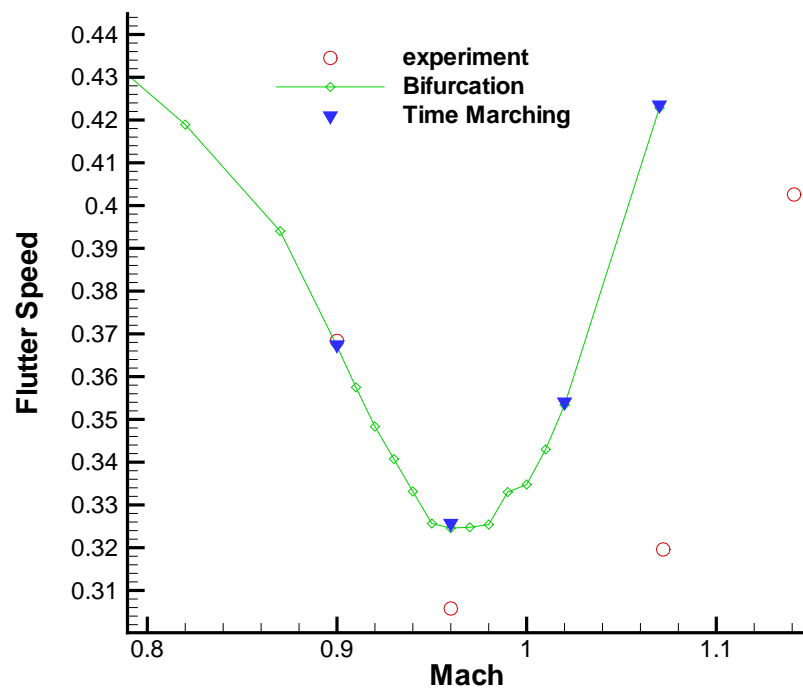


FIGURE 5.3: Comparison with measurements of the stability boundaries calculated on the medium grid using time marching and the bifurcation solver

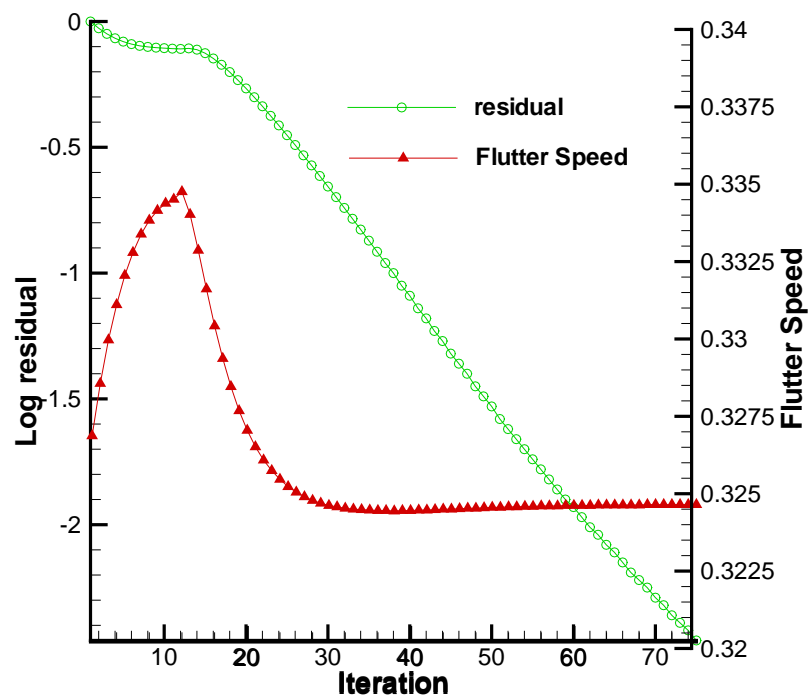
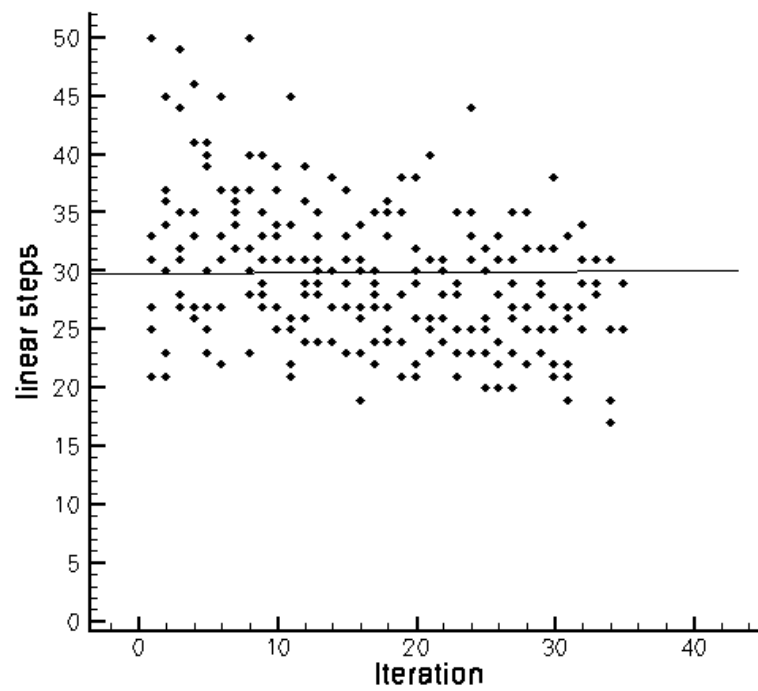


FIGURE 5.4: The convergence of the bifurcation parameter with the bifurcation solver iteration number at Mach 0.96. The flutter speed index is shown against the right hand axes and the augmented residual against the left hand axes



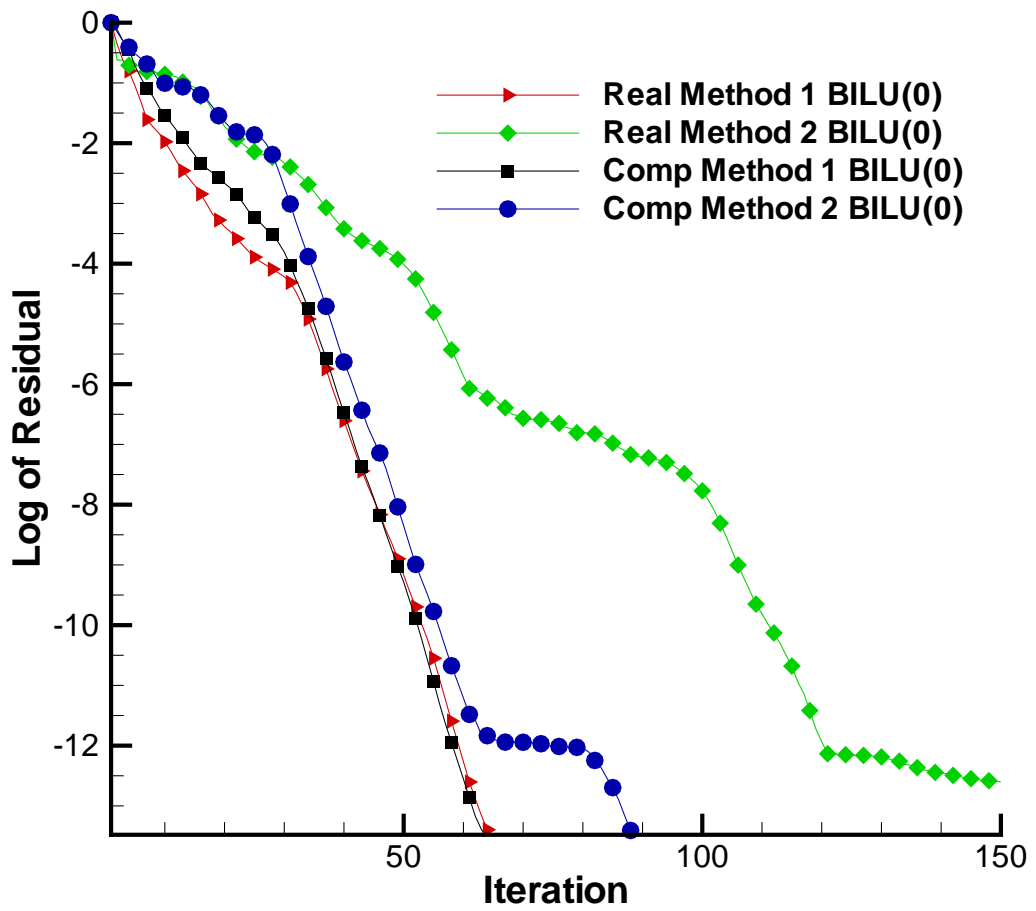


FIGURE 5.6: Comparison of the real and complex formulations for methods 1 and 2 with a modified order Jacobian

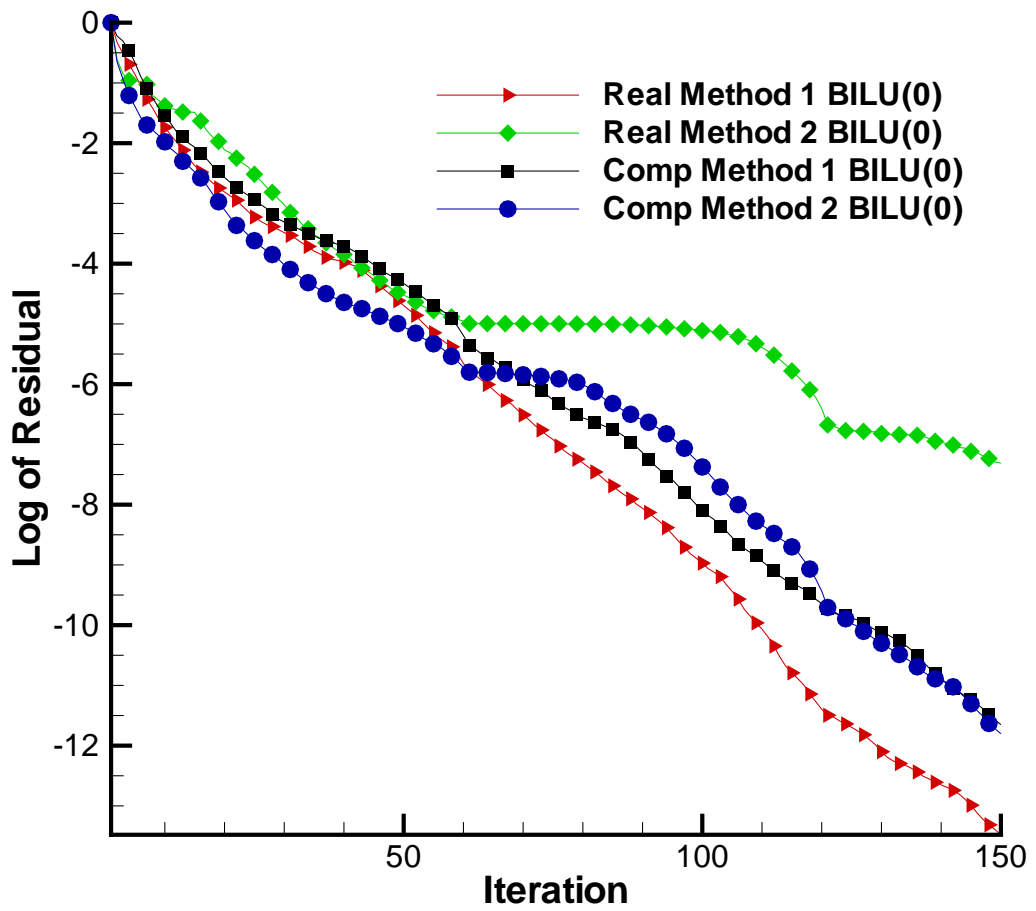


FIGURE 5.7: Comparison of the real and complex formulations for methods 1 and 2 with a second-order Jacobian

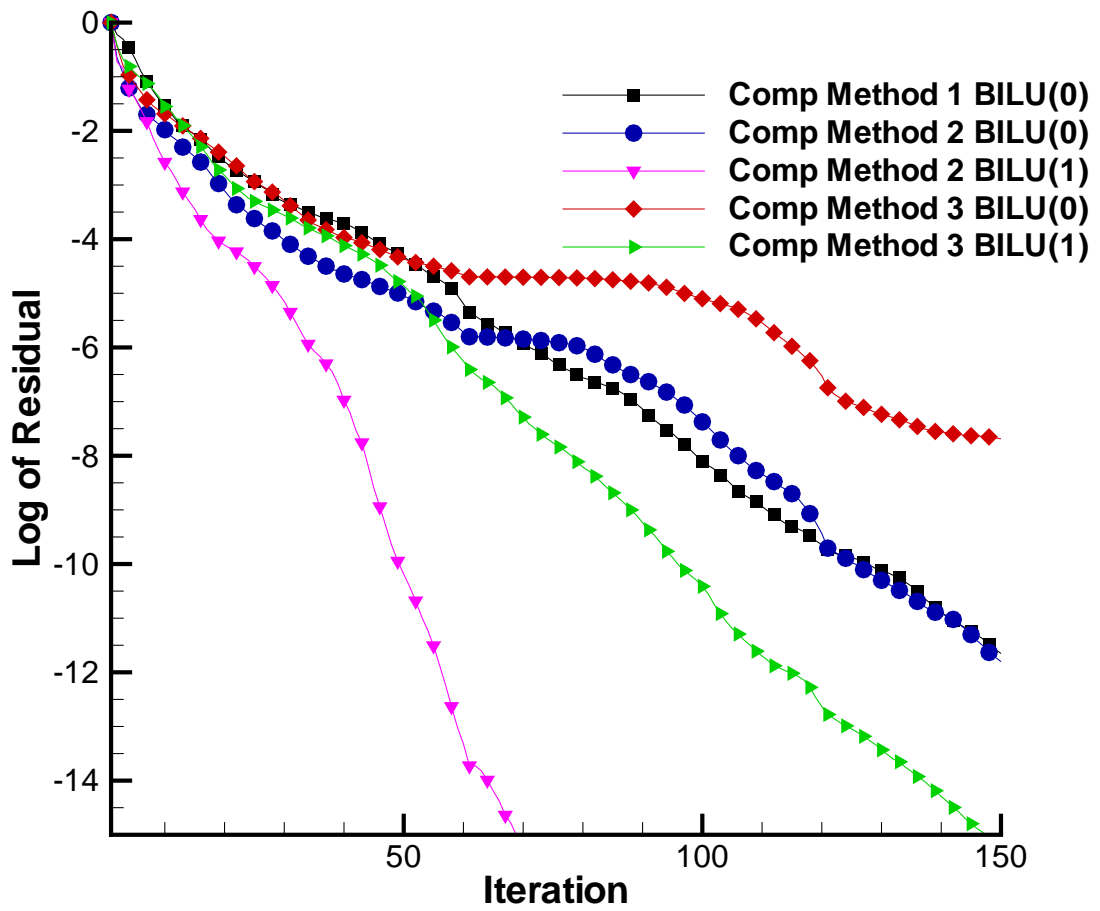


FIGURE 5.8: Comparison of complex formulations for all the methods with a second-order Jacobian

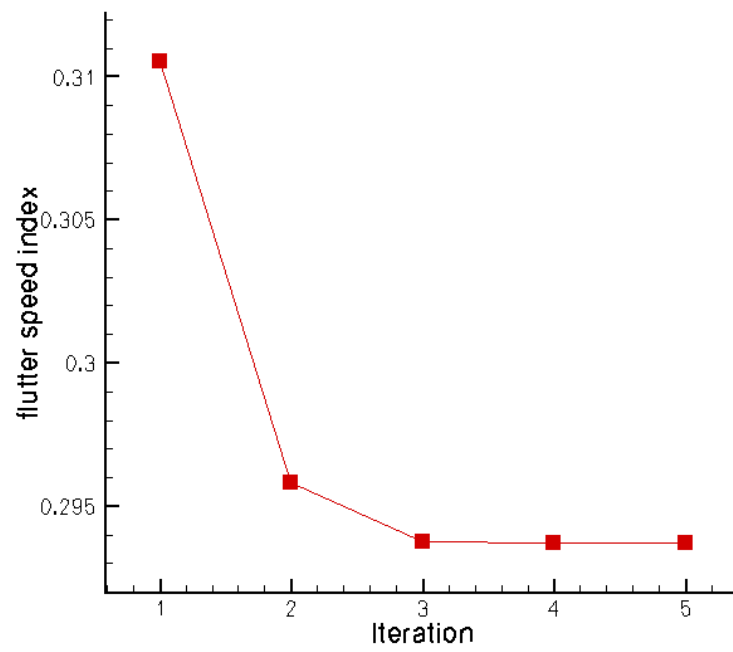
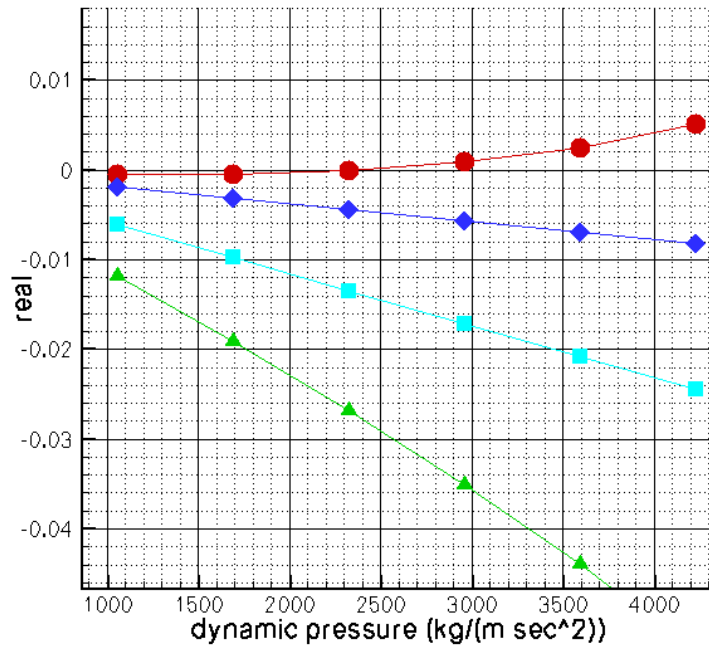
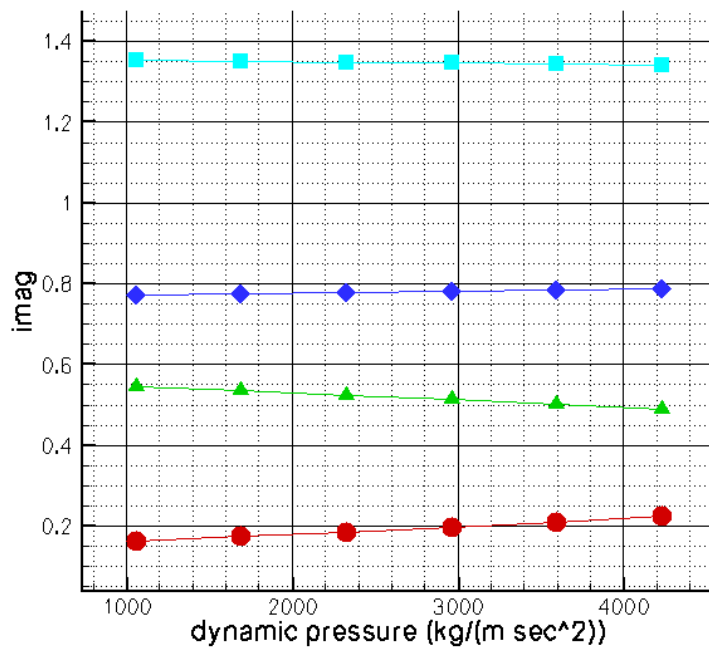


FIGURE 5.9: Convergence of flutter speed index for AGARD wing at Mach 0.97

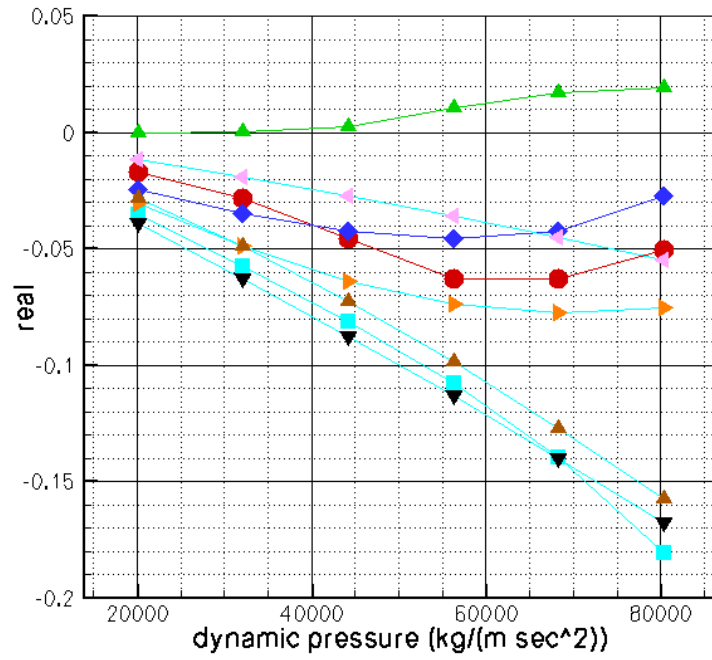


real

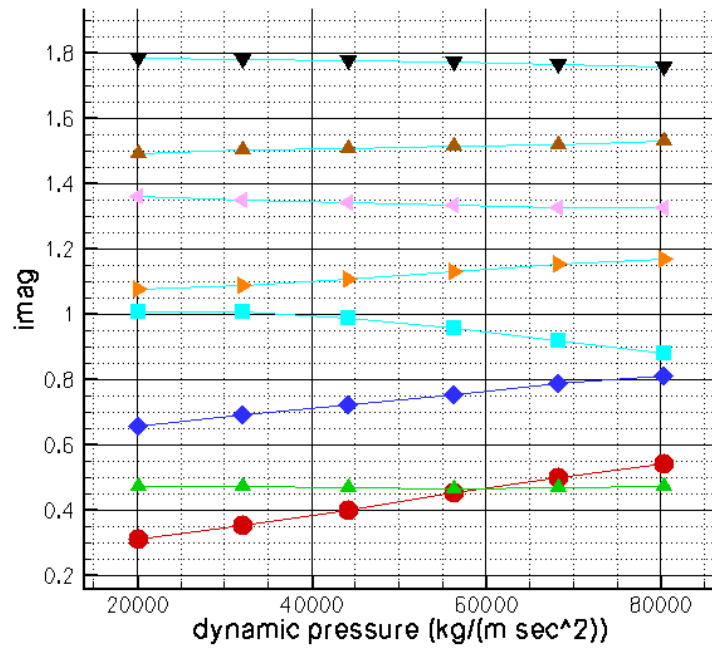


imaginary

FIGURE 5.10: Tracking of eigenvalues for AGARD wing at Mach 0.97. Each line corresponds to one aeroelastic mode and the symbols are consistent between the graphs for the real and imaginary parts

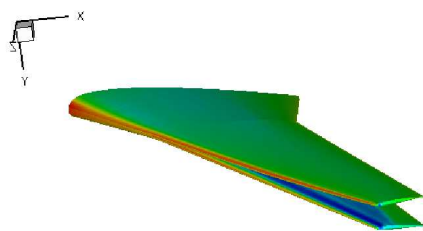


real

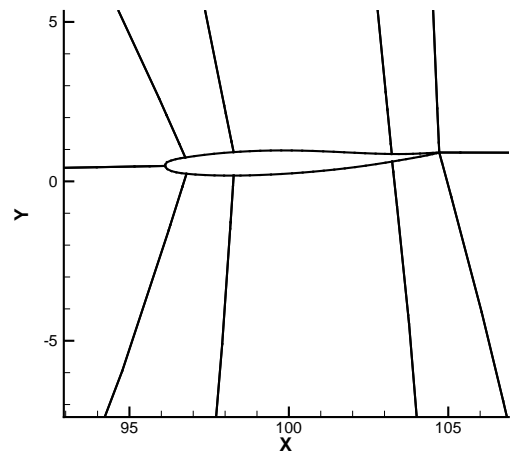


imaginary

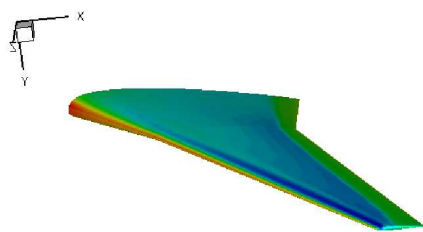
FIGURE 5.11: Tracking of eigenvalues for MDO wing with no initial aerostatic solution at Mach 0.85. Each line corresponds to one aeroelastic mode and the symbols are consistent between the graphs for the real and imaginary parts



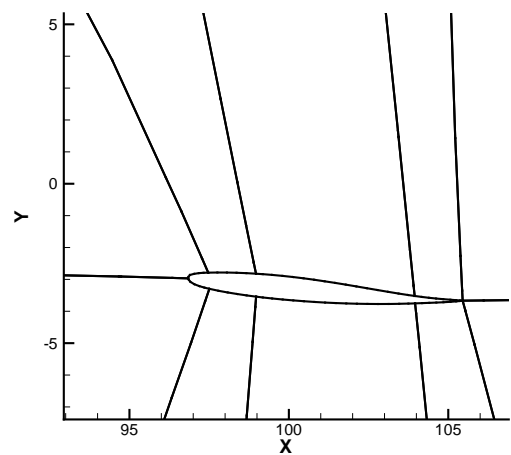
static deformed- surface C_p



static deformed - section near tip



rigid - surface C_p



rigid - section near tip

FIGURE 5.12: *Surface pressure distribution and tip aerofoil section for rigid and static deformed positions of MDO wing at Mach 0.85*

Chapter 6

Prediction of Aeroelastic Limit Cycle Oscillations

6.1 Introduction

Limit cycle oscillations (LCO)s have become one central focus in aircraft aeroelasticity. A major reason for this is the widely reported LCO experienced (and tolerated) on the F-16 in certain store configurations.^[130] The source of the LCO is still a matter of conjecture, with both nonlinear aerodynamics and structural dynamics being considered by the uncertainty study of Thomas *et al.*^[131] Predating the first report of an LCO on the F-16 was the residual pitch oscillation for the B2 bomber^[132] which was attributed to an interaction between the wing bending mode, a shock movement on the upper surface and the control system.

LCOs can be tolerated (as illustrated by the F-16 example) if the amplitude is sufficiently low. Detrimental effects may accrue to the pilot and the airframe, but the onset of LCO does not necessarily threaten the integrity of the airframe as an unbounded flutter would. It has been suggested that future aircraft may even tolerate regions of LCO in return for gains in performance.

To tolerate or eliminate LCOs requires reliable analysis tools to provide a physical insight into the underlying mechanisms, and quantitative predictions. If nonlinear aerodynamics is involved then a general purpose tool should exploit computational fluid dynamics (CFD). CFD simulations of aeroelastic behaviour in the time domain have reached an impressive level of maturity. Farhat and co-workers^[23] carried out fundamental work on the numerical methods underpinning such a sim-

ulation. Melville^[24] used high-fidelity CFD to reproduce LCO behaviour for the F-16. A similarly impressive effort was undertaken at NLR^[133].

Whilst time domain simulations are a powerful and general tool for analysis, they suffer from one practical disadvantage, namely computational cost. For an analysis of underlying mechanisms it is likely that a parametric search and sensitivity analysis will be required. If this must be done carrying the cost of time domain simulations, then the overall cost is likely to be prohibitive.

This has stimulated active research in reduced order modelling. The aim is to retain the predictive capability of full CFD aerodynamics, but with reduced computational cost. Two broad classes of method have appeared, namely data driven models and methods which work with the system residual. For data driven models a number of forced motion CFD calculations are computed. The aerodynamic response is then processed to provide a low order model. Examples include proper orthogonal decomposition^[45,134] and Volterra series^[135]. The disadvantages of these approaches is the lack of a general robust parameterisation of the model, and their inability to predict any physics which is not included in the training data. This class of method has met with some success.

The current chapter represents the final step in the basic tool development within this research effort. Based on the knowledge of the critical eigenvector of the aeroelastic system, and using Kuznetsov's^[87] method of projection for the computation of centre manifolds outlined in chapter 3 a method is formulated for the prediction of wing limit cycle oscillations.

6.2 Model Reduction for LCO Calculation

The response of the system after bifurcation may be required, particularly if it is a LCO. The semi-discrete form of the coupled CFD-FEM system is

$$\frac{d\mathbf{w}}{dt} = \mathbf{R}(\mathbf{w}, \mu) \quad (6.1)$$

where

$$\mathbf{w} = [\mathbf{w}_f, \mathbf{w}_s]^T \quad (6.2)$$

is a vector containing the fluid unknowns \mathbf{w}_f and the structural unknowns \mathbf{w}_s and

$$\mathbf{R} = [\mathbf{R}_f, \mathbf{R}_s]^T \quad (6.3)$$

is a vector containing the fluid residual \mathbf{R}_f from the three-dimensional Euler equations and \mathbf{R}_s is given by equation (5.7). The residual also depends on a parameter μ which is independent of \mathbf{w} . As in section 5.2.2 the bifurcation parameter $\mu = \rho_\infty/\rho_w$ so for a given Mach number and velocity it is possible to calculate the dynamic pressure q . An equilibrium of this system $\mathbf{w}_0(\mu)$ satisfies $\mathbf{R}(\mathbf{w}_0, \mu) = \mathbf{0}$.

Equation (6.1) is now expanded in a Taylor series so it is in a form where the method of projection shown in chapter 3 can be used to calculate the centre manifold.

$$\mathbf{R}(\mathbf{w}, \mu) = \mathbf{R}(\mathbf{w}_0, \mu) + A(\mathbf{w}_0) \cdot (\mathbf{w} - \mathbf{w}_0) + F(\mathbf{w} - \mathbf{w}_0, \mu)$$

For values of the bifurcation parameter below the Hopf bifurcation where all the real part of the eigenvalues are negative, it is possible to simplify equation (3.31) farther. For a small interval below the bifurcation point the eigenvalue of largest real part will be associated with the critical eigenvalue in S . All the eigenvalues associated with the noncritical space T are damped faster. Therefore the influence of \mathbf{y} can be neglected leading to the following damping model

$$\dot{z} = i\omega z + \langle \mathbf{q}, \mathbf{R}_\mu \mu \rangle + z\mu \langle \mathbf{q}, A_\mu \mathbf{p} \rangle + \bar{z}\mu \langle \mathbf{q}, A_\mu \bar{\mathbf{p}} \rangle$$

This model will not predict the transient behaviour of the system (6.1) but will have the correct behaviour as $t \rightarrow \infty$.

Restricting system of equations (3.31) on the centre manifold representation (3.25) gives

$$\begin{aligned} \dot{z} &= i\omega z + \frac{1}{2}G_{20}z^2 + G_{11}z\bar{z} + \frac{1}{2}G_{02}\bar{z}^2 \\ &+ \frac{1}{2}(G_{21} + 2\langle G_{10}, \mathbf{k}_{11} \rangle + \langle G_{01}, \mathbf{k}_{20} \rangle)z^2\bar{z} \\ &+ \langle \mathbf{q}, \mathbf{R}_\mu \mu \rangle + z\mu \langle \mathbf{q}, A_\mu \mathbf{p} \rangle + \bar{z}\mu \langle \mathbf{q}, A_\mu \bar{\mathbf{p}} \rangle \\ &+ \frac{\mu}{2}\langle \mathbf{q}, A_\mu \mathbf{k}_{20} \rangle z^2 + \mu \langle \mathbf{q}, A_\mu \mathbf{k}_{11} \rangle z\bar{z} + \frac{\mu}{2}\langle \mathbf{q}, A_\mu \mathbf{k}_{02} \rangle \bar{z}^2 \dots \end{aligned}$$

If we write the quadratic and higher part of \mathbf{R} (which is $F(\mathbf{w}, \mu)$), in terms of the bilinear function $B(x, y)$ as in equation (3.9) and the trilinear function $C(x, y, z)$ as in equation (3.10) then the restricted equation is in the form

$$\begin{aligned} \dot{z} &= i\omega z + \frac{1}{2}G_{20}z^2 + G_{11}z\bar{z} + \frac{1}{2}G_{02}\bar{z}^2 \\ &+ \frac{1}{2}(G_{21} - 2\langle \mathbf{q}, B(\mathbf{p}, A^{-1}\mathbf{H}_{11}) \rangle + \langle \mathbf{q}, B(\bar{\mathbf{p}}, (2i\omega I - A)^{-1}\mathbf{H}_{20}) \rangle)z^2\bar{z} \\ &+ \langle \mathbf{q}, \mathbf{R}_\mu \mu \rangle + z\mu \langle \mathbf{q}, A_\mu \mathbf{p} \rangle + \bar{z}\mu \langle \mathbf{q}, A_\mu \bar{\mathbf{p}} \rangle \\ &+ \frac{\mu}{2}\langle \mathbf{q}, A_\mu (2i\omega I - A)^{-1}\mathbf{H}_{20} \rangle z^2 + \mu \langle \mathbf{q}, A_\mu A^{-1}\mathbf{H}_{11} \rangle z\bar{z} \\ &- \frac{\mu}{2}\langle \mathbf{q}, A_\mu (2i\omega I + A)^{-1}\mathbf{H}_{02} \rangle \bar{z}^2 + \dots \end{aligned} \tag{6.4}$$

where G_{ij} are defined by equation (3.22) and \mathbf{H}_{ij} $i + j = 2$ by equation (3.23). This is a two degree of freedom system for the response of the full order system in the critical mode, eigenvalue with zero real part. The normal form of the Hopf bifurcation given by equation (3.29) shows the same cubic terms as those of the two degree of freedom model and hence contains enough information to be able to predict limit cycle behaviour after the bifurcation point. This model was successfully able predict LCOs in the model problem in chapter 3. The reduced model is calculated once and for all after the critical eigenvector, eigenvalue and equilibrium point are known. The model is parameterised through the Taylor expansion in the bifurcation parameter, and so can be used to explore the behaviour of the full system in the vicinity of the bifurcation. Analogous with chapter 3 the centre manifold that the restriction takes place on is not parameter dependent. The main challenge in forming the model is in the matrix vector products against the second and third Jacobians, and this will be discussed below. The linear systems that need to be solved to compute the coefficients in the centre manifold reduction are solved in the same manner as described in the previous chapter and represent the main computational cost in forming the model.

6.3 Calculation of First, Second and Third Jacobians

The Jacobian is calculated as described in detail in section 5.3. The second and third Jacobians required in the model reduction are represented by the bilinear and trilinear functionals

$$B_i(\mathbf{x}, \mathbf{y}) = \sum_{j,k=1}^n \left. \frac{\partial^2 F(\boldsymbol{\xi})}{\partial \xi_j \partial \xi_k} \right|_{\boldsymbol{\xi}=\mathbf{w}_0} x_j y_k, \quad i = 1, 2, \dots, n \quad (6.5)$$

and

$$C_i(\mathbf{x}, \mathbf{y}, \mathbf{z}) = \sum_{j,k,l=1}^n \left. \frac{\partial^3 F(\boldsymbol{\xi})}{\partial \xi_j \partial \xi_k \partial \xi_l} \right|_{\boldsymbol{\xi}=\mathbf{w}_0} x_j y_k z_l, \quad i = 1, 2, \dots, n \quad (6.6)$$

as described in section 3.3. For the model problem shown in chapter 3 these terms were analytical however for the aeroelastic case analytical expressions for the second and third Jacobians may not be available. It is possible to calculate all of the contributions to equations (6.5) and (6.6) without having to resort to complex arithmetic, or having to calculating all the second and third partial derivatives analytically. By the use of directional derivatives it is then possible to evaluate the bilinear

and trilinear functions $B(\mathbf{x}, \mathbf{y})$ and $C(\mathbf{x}, \mathbf{y}, \mathbf{z})$ on any set of coinciding real vectors. These derivatives can be approximated using finite differences,

$$B(\mathbf{v}, \mathbf{v}) = \frac{1}{h^2} [\mathbf{R}(\mathbf{w}_0 + h\mathbf{v}, \mu_0) - 2\mathbf{R}(\mathbf{w}_0, \mu_0) + \mathbf{R}(\mathbf{w}_0 - h\mathbf{v}, \mu_0)] + O(h^2) \quad (6.7)$$

and

$$C(\mathbf{v}, \mathbf{v}, \mathbf{v}) = \frac{1}{8h^3} [-\mathbf{R}_3 + 8\mathbf{R}_2 - 13\mathbf{R}_1 + 13\mathbf{R}_{-1} - 8\mathbf{R}_{-2} + \mathbf{R}_{-3}] + O(h^4) \quad (6.8)$$

where h is small, and $\mathbf{R}_l = \mathbf{R}(\mathbf{w}_0 + lh\mathbf{v}, \mu_0)$. Note at the equilibrium point $\mathbf{R}_0 = 0$. Using the polarisation identity^[136]

$$B(\mathbf{v}, \mathbf{u}) = \frac{1}{4} [B(\mathbf{v} + \mathbf{u}, \mathbf{v} + \mathbf{u}) - B(\mathbf{v} - \mathbf{u}, \mathbf{v} - \mathbf{u})]$$

and a similar identity for trilinear functionals

$$C(\mathbf{v}, \mathbf{v}, \mathbf{u}) = \frac{1}{6} [C(\mathbf{v} + \mathbf{u}, \mathbf{v} + \mathbf{u}, \mathbf{v} + \mathbf{u}) - C(\mathbf{v} - \mathbf{u}, \mathbf{v} - \mathbf{u}, \mathbf{v} - \mathbf{u}) - 2C(\mathbf{u}, \mathbf{u}, \mathbf{u})]$$

it is possible to work out all the constants in equation (6.4) i.e.

$$\begin{aligned} G_{11} = \langle \mathbf{q}, B(\mathbf{p}, \bar{\mathbf{p}}) \rangle &= \langle \mathbf{q}_r + i\mathbf{q}_i, B(\mathbf{p}_r, \mathbf{p}_r) + B(\mathbf{p}_i, \mathbf{p}_i) \rangle \\ &= \langle \mathbf{q}_r, B(\mathbf{p}_r, \mathbf{p}_r) + B(\mathbf{p}_i, \mathbf{p}_i) \rangle - i \langle \mathbf{q}_i, B(\mathbf{p}_r, \mathbf{p}_r) + B(\mathbf{p}_i, \mathbf{p}_i) \rangle \end{aligned}$$

And finally there is the choice of h , for clarity the example of the first order Jacobian is used. Consider the Jacobian-vector product

$$A\mathbf{v} \approx \frac{\mathbf{R}(\mathbf{w} + h\mathbf{v}, \mu_0) - \mathbf{R}(\mathbf{w}, \mu_0)}{h}$$

for some step size h . In finite precision, due to rounding errors, $\mathbf{R}(\mathbf{w}, \mu_0) + \varepsilon(\mathbf{w})$ is computed instead of $\mathbf{R}(\mathbf{w}, \mu_0)$. Assuming that the rounding error is less than $\bar{\varepsilon}$ for all \mathbf{w}

$$A\mathbf{v} - \frac{\mathbf{R}(\mathbf{w} + h\mathbf{v}, \mu_0) + \varepsilon(\mathbf{w} + h\mathbf{v}) - \mathbf{R}(\mathbf{w}, \mu_0) - \varepsilon(\mathbf{w})}{h} = O(h + \bar{\varepsilon}/h)$$

The error is minimised when

$$h = \sqrt{\bar{\varepsilon}} \frac{\|\mathbf{w}\|_2}{\|\mathbf{v}\|_2}.$$

For the general case the error is

$$O(h^j + \bar{\varepsilon}/h^k) \quad h \approx \sqrt[j+k]{\bar{\varepsilon}}$$

of a finite difference of j th order for the k th derivative. For the third Jacobian, even in the best case where the components w_i and v_i are of similar magnitude, the

corresponding expression for the optimal stepsize is $h \approx \sqrt[3]{\epsilon}$. For a standard double precision number there are 53 bits in the mantissa which leads to $\epsilon = 1/2^{53} \approx 1.11 \times 10^{-16}$. Hence $h = 0.0053$ and at best six significant figures can be obtained. However in general the answer is much less accurate the v_i vary by many orders of magnitude. One way to increase the accuracy is to increase the number of bits in the mantissa. This can be achieved by increasing the precision of the arithmetic for the residual evaluation. A high precision version of sqrt, log and exp functions are also be required, in this case because of the contributions of such functions in Osher's flux function. The QD library^[137] was used to obtain this functionality. This library allows extension of existing code to double-double precision (twice that of doubles) and quad-double precision (four times that of doubles) without major recoding, by using operator overloading. Operator overloading does slow down the calculation of the \mathbf{R} but it is a one time cost.

The convergence of the reduced model coefficients under h -refinement for the Goland wing example (discussed below) at Mach 0.92 is demonstrated in table 6.1. We would expect these coefficients to behave as follows. First, for large values of h there would be significant inaccuracy due to truncation error. At small values of h we would see inaccuracy due to rounding error. The latter effect would be more significant for the coefficient which includes a third Jacobian product, and also less significant using quad-double arithmetic. For a usable method we need to obtain consistent results over a significant range of h . The table conforms to all of these expectations and a reliable set of coefficients for the reduced model is obtained.

6.4 Results

The heavy version of the Goland wing is used to investigate the prediction of LCO behaviour. The Goland wing has a chord of 1.8288m and a span of 6.096m. It is a rectangular symmetric cantilevered wing with a 4% thick parabolic section. The structural model follows the description given in reference^[67]. The case used here has a tip store in the structural model, but not in the aerodynamic model. Four modes were extracted at frequencies (in Hertz) of 1.72 (first bending), 3.05 (first torsion), 9.18 (second bending) and 11.10 (second torsion). These modes are shown in figure 6.1. An interesting feature of this test case is the appearance of a region of limit cycle oscillation at a reduced value of dynamic pressure (a

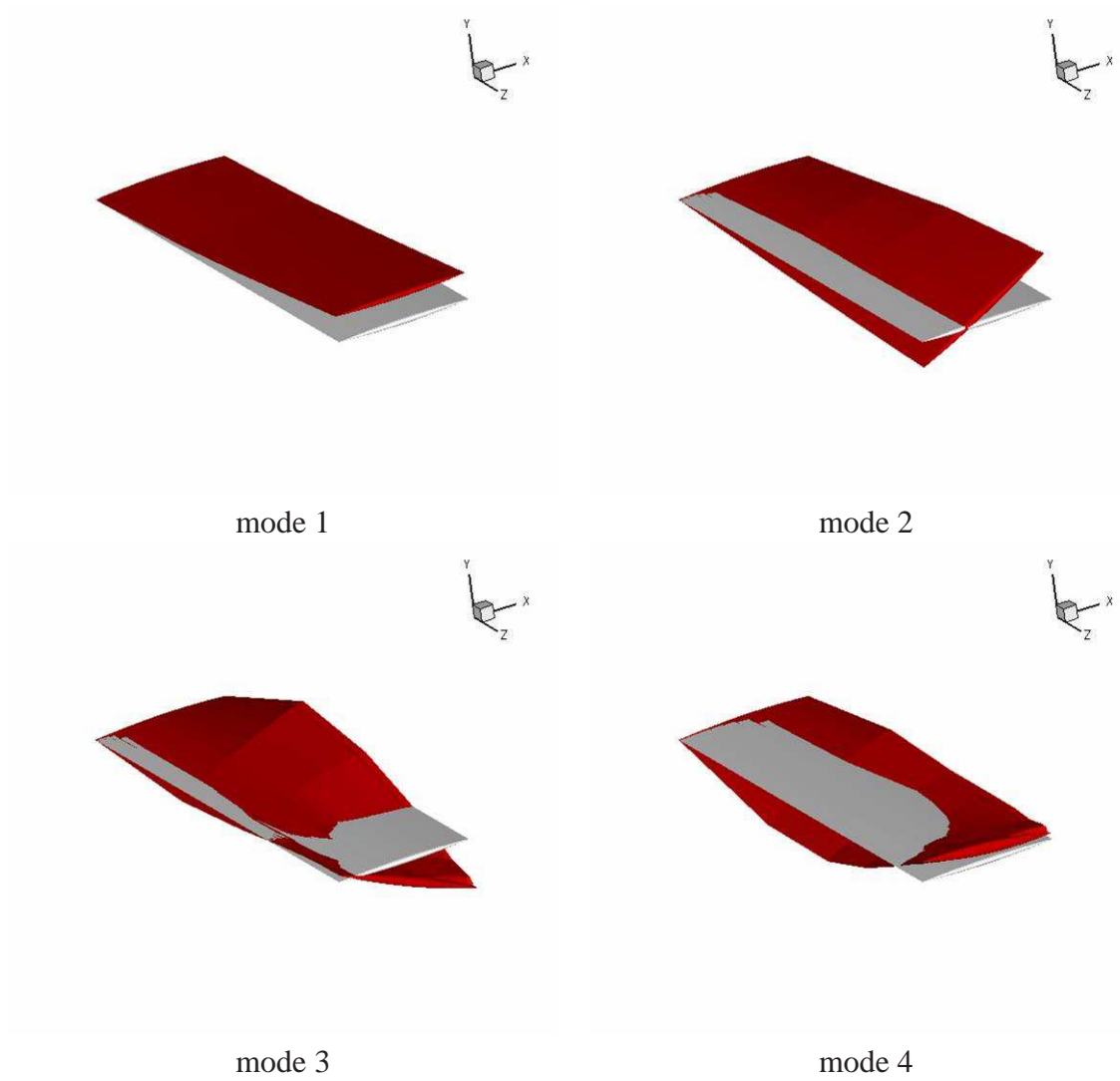


FIGURE 6.1: *Structural Modes for Golang wing.*

precision	h	G_{20}	G_{02}	G_{21}	k_{11}
d-d	10^{-2}	1.15941e-03	3.81780e-04	-6.31471e-01	-8.57054e-04
d-d	10^{-4}	3.83222e-04	3.04452e-03	5.28431e+00	-1.69352e-03
d-d	10^{-6}	1.19108e-03	4.41072e-04	-1.50604e-03	-8.36232e-04
d-d	10^{-8}	1.19108e-03	4.41072e-04	-1.91813e-03	-8.36232e-04
d-d	10^{-10}	1.19108e-03	4.41070e-04	3.67596e+02	-8.36229e-04
d-d	10^{-12}	1.12010e-03	4.57337e-04	-2.37683e+08	-8.66090e-04
q-d	10^{-2}	1.07216e-03	4.67501e-04	-5.96457e-01	-8.09330e-04
q-d	10^{-4}	3.83222e-04	3.04452e-03	5.28431e+00	-1.69352e-03
q-d	10^{-6}	1.19108e-03	4.41072e-04	-1.50604e-03	-8.36232e-04
q-d	10^{-8}	1.19108e-03	4.41072e-04	-1.50604e-03	-8.36232e-04
q-d	10^{-10}	1.19108e-03	4.41072e-04	-1.50604e-03	-8.36232e-04
q-d	10^{-12}	1.19108e-03	4.41072e-04	-1.50604e-03	-8.36232e-04
q-d	10^{-14}	1.19108e-03	4.41072e-04	-1.50604e-03	-8.36232e-04
q-d	10^{-16}	1.19108e-03	4.41072e-04	-1.50604e-03	-8.36232e-04
q-d	10^{-18}	1.19108e-03	4.41072e-04	-1.52353e-03	-8.36232e-04

TABLE 6.1: *Convergence of reduced order model coefficient real parts under h refinement. The behaviour of the real and imaginary parts not shown is identical. Note that all columns include 2nd Jacobian-vector products except the column for G_{21} which contains a 3rd Jacobian-vector product. The abbreviations d-d and q-d stand for double-double and quad-double respectively*

”bucket”) at a freestream Mach number of 0.92. This has been shown using the Euler equations^[138] and the transonic small disturbance equations^[67]. The influence of the tip store was examined in reference^[139] and the effect of including the store aerodynamics in reference^[34].

Following the experience gained with generating grids for the AGARD wing, a grid with 27 000 points (135 000 degrees of freedom) was generated using a block topology which concentrates points in the tip region. This grid reproduces the behaviour previously reported in the literature, namely a rising flutter speed around Mach 0.9, a significant bucket with LCO behaviour about $M=0.92$, and then a rise in flutter speed at the right-hand end of the bucket around 0.94. The values at which these different behaviours happen is similar in the current work, and it is concluded that the current grid for the Goland wing represents a proper test for the methods presented in chapters 5 and 6. The inverse power method is used to investigate the behaviour of the structural modes under the influence of transonic aerodynamics. Mach numbers of 0.90, 0.92 and 0.94 were investigated, these values being chosen because of prior knowledge of the system behaviour from the literature.

However, without prior knowledge of the aeroelastic behaviour this Mach number range would have been quickly identified by considering shock wave behaviour for the steady state solutions or by using the direct augmented solver. Starting with the structural frequency as a shift, the eigenvalue in the aeroelastic system was computed for six values within a range of dynamic pressure, chosen based on linear flutter analysis. The results show that at Mach 0.90 and 0.94, the third and fourth modes interact, and eventually the fourth mode crosses the imaginary axis. The behaviour of the real part of the fourth mode is shown in figure 6.2, where it is also seen that the behaviour of this mode at Mach 0.92 is very similar. However, at Mach 0.92 the second mode crosses the imaginary axis at a lower dynamic pressure, also shown in figure 6.2, and it is this mode which results in a limit cycle oscillation.

Having gained some insight into the behaviour of the eigenspectrum, the direct method was then used to find the bifurcation point at Mach 0.92. An estimate of the dynamic pressure, frequency and eigenvector was obtained from the inverse power results. The convergence of the dynamic pressure is shown in figure 6.3 and again shows quadratic convergence.

Finally, the behaviour of the limit cycle oscillation was investigated using the reduced model. The model coefficients were formed using the expressions described above, based on the critical eigenvectors, the equilibrium solution and first, second and third Jacobian - vector products. Time domain simulations were also run to provide a comparison for the predictions of the reduced model. The time domain simulations used a non dimensional time step of 0.5, giving about 70 time steps per period of response which provides time accuracy at a low computational cost.

First the reduced model predictions are compared with the full model for damped responses. The comparison of the response of the first mode is shown in figure 6.4 at 80% and 95% of the critical dynamic pressure. In both cases the damped response is predicted well by the reduced model.

The comparison of the reduced and full nonlinear predictions of the LCO response of the first and second structural modes at a value of dynamic pressure which is 25% above the bifurcation value is shown in figure 6.5. The two sets of results agree well. The rise in amplitude with increasing dynamic pressure is shown in figure 6.6 and it is seen that the reduced model predicts well the LCO amplitude for values of dynamic pressure up to 40% above the bifurcation value in this case.

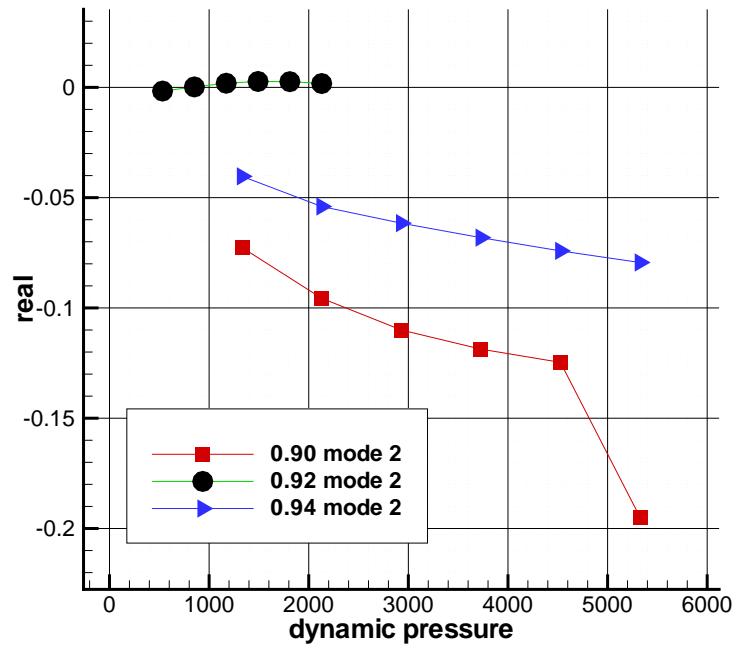
A set of visualisations of the wing location and the difference in pressure from the equilibrium solution is compared in figure 6.7. The wing motion is a combination of plunging and pitching towards the tip, and the fluid response is dominated by changes of pressure towards the leading edge and due to the shock motion. The predictions of the reduced order model and the full system are very similar qualitatively and quantitatively (note that these 2 sets of results are plotted on the same scale, with the extreme values being $\pm 4\%$ of the free-stream pressure).

6.4.1 Evaluation of Cost

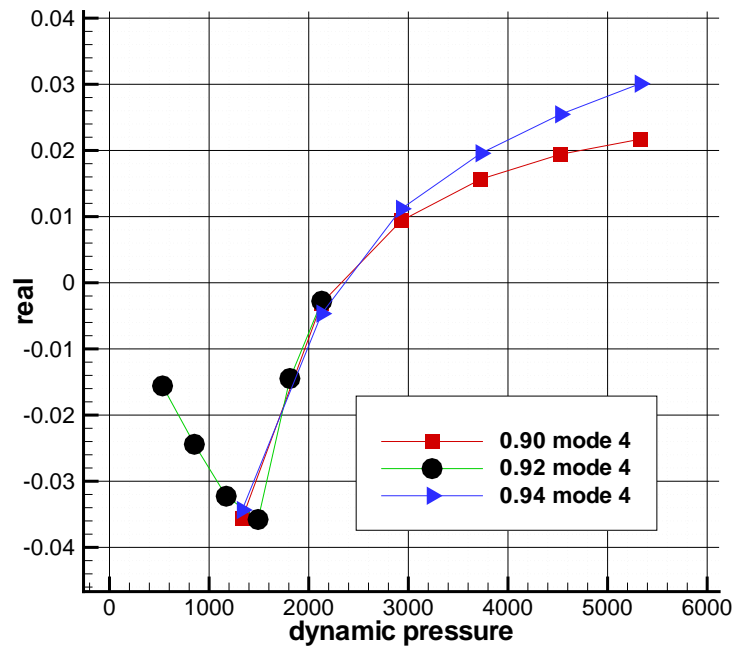
The performance of the methods is assessed in the current section. The benchmark adopted is the cost of a steady state calculation since this is generally quite modest on modern computers, and with modern algorithms, even for complex problems. The summary of the cost for the different methods is given in table 6.2.

It is noted that the steady solver used here has proved efficient on a wide variety of CFD and aeroelastic test cases. To illustrate the steady state performance the Goland wing used 100 explicit time steps to start the calculation, followed by no more than 100 implicit time steps at a CFL number of 50 to drive the residual down at least 6 orders of magnitude. The unsteady solver is similarly considered efficient in the sense that the time step was chosen for time accuracy considerations only, resulting in around 70 time steps per cycle of response for the Goland wing.

The cost of computing the LCO's of the Goland wing by the full order system is very significant. The full system time marching can take many hundreds of cycles to reach the limit cycle, especially close to the bifurcation point. The computation using the reduced model has several stages whose cost is summarised in table 6.2. First, the inverse power method is used to map out the behaviour of the eigenvalues. This requires multiple applications of the inverse power method with different shifts - for each of the four structural modes 6 dynamic pressures were computed, giving a cost of 130 steady state calculation. It was then quick to compute the bifurcation point using the direct method and to generate the two-degree-of-freedom model. Overall the cost of generating the reduced model is less than 170 steady state calculations. If the critical frequency is known in advance, then the inverse power part of the calculation can be skipped, substantially reducing the computational cost. Once the model is computed, it is parametrised, and so can be used to replace multiple unsteady full system calculations. The reduction in computational cost, even



mode 2



mode 4

FIGURE 6.2: Behaviour of the damping of modes 2 and 4 for Goland wing at Mach 0.92. Here dynamic pressure is in units of $\text{kg}/(\text{msec}^2)$.

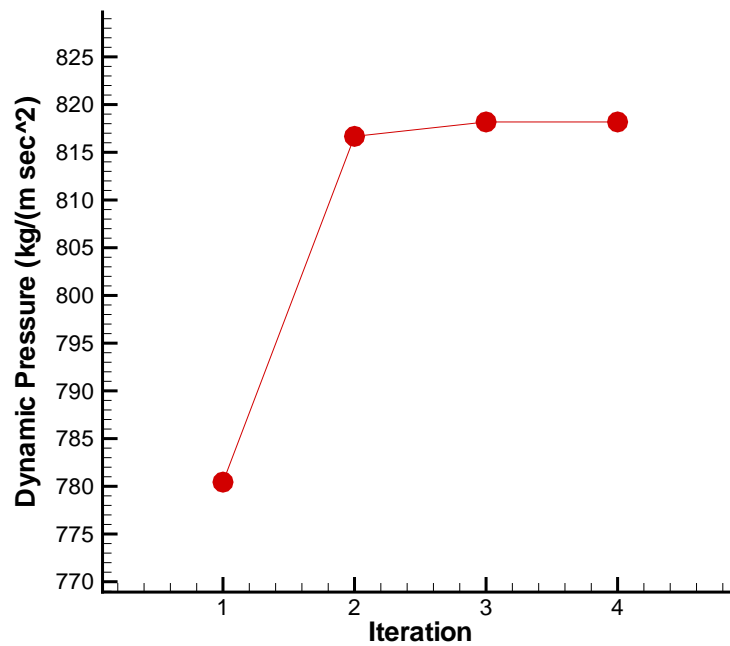


FIGURE 6.3: Convergence of bifurcation parameter for Goland wing at Mach 0.92.

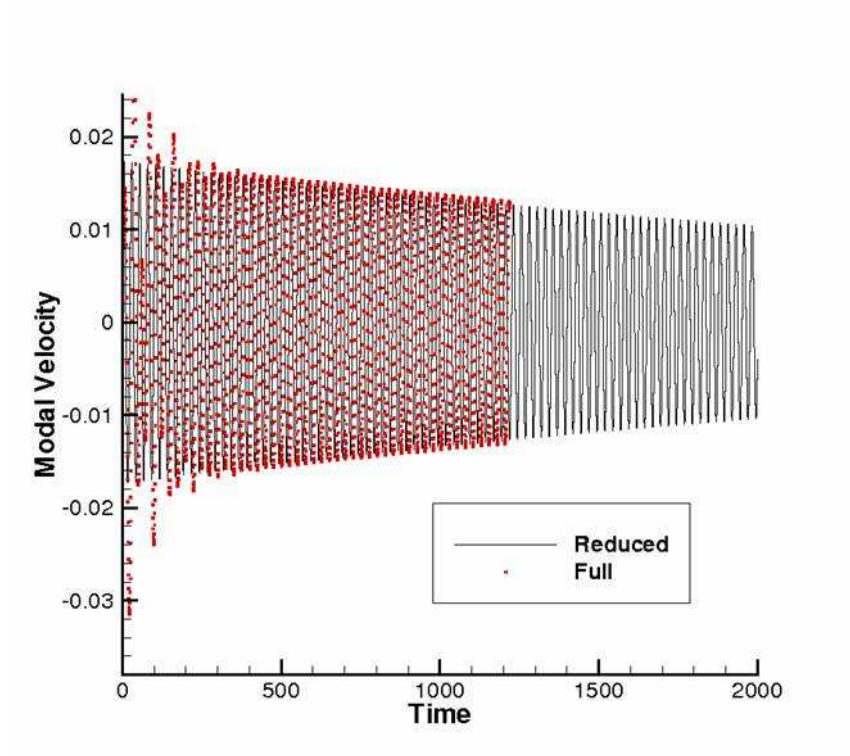
when the inverse power calculation is required, is by two orders of magnitude when several LCO calculations are required.

Case	Steady	IPM	Root Locus	Direct	Unsteady
Goland	1	5.4	130	9.2	1000

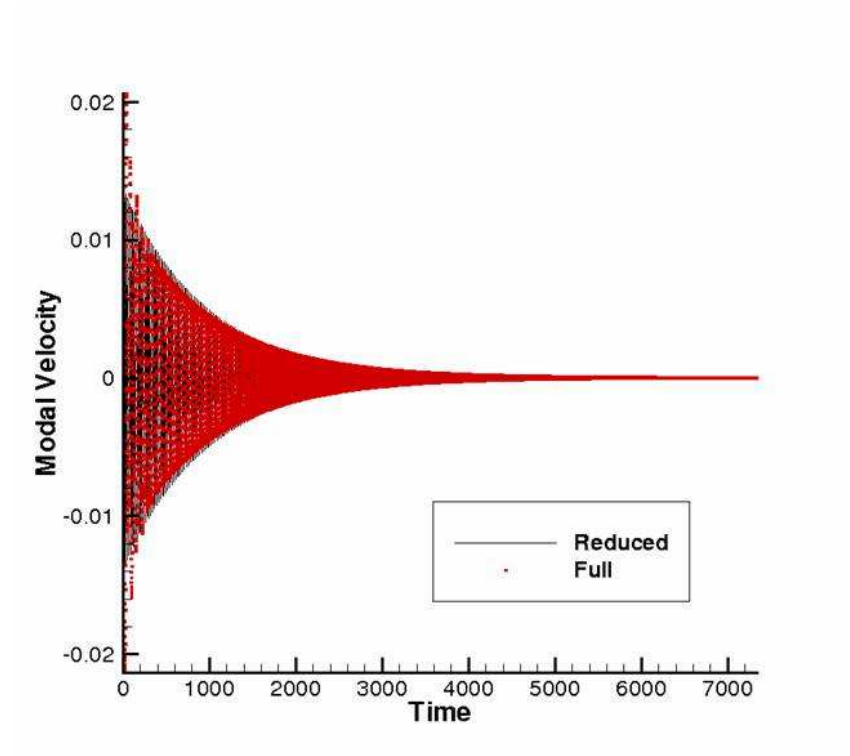
TABLE 6.2: Summary of the costs expressed in multiples of the steady state solution.

6.5 Conclusions

This chapter has provided a formulation to allow LCO predictions based on CFD generated aerodynamics. If little is known about the instability onset then the inverse power method can be used to map out the behaviour of the eigenvalues in the regions likely to be of interest. This information can then be used to setup an augmented solve for the flutter point, along with other information like the critical eigenvector and the frequency of the instability. In turn this information can then be used to compute a two degree of freedom model for the system dynamics around

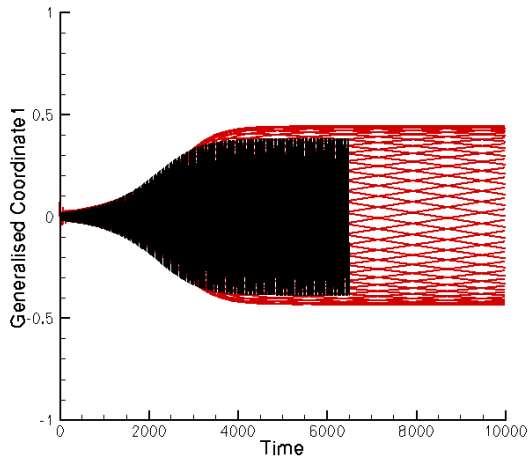


95% of the critical dynamic pressure

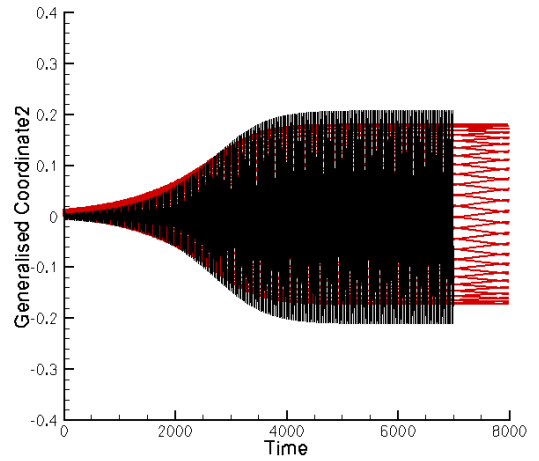


80% of the critical dynamic pressure

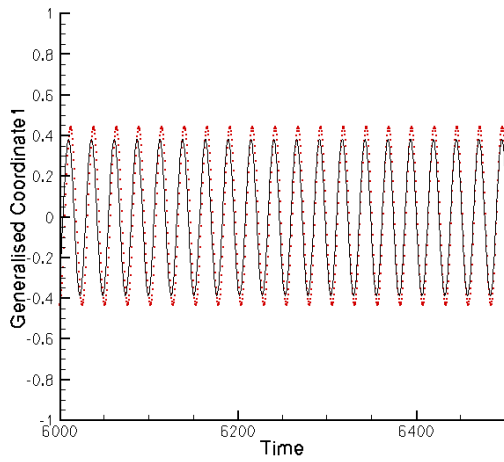
FIGURE 6.4: Comparison between the full and reduced predictions of damping for Goland wing at Mach 0.92.



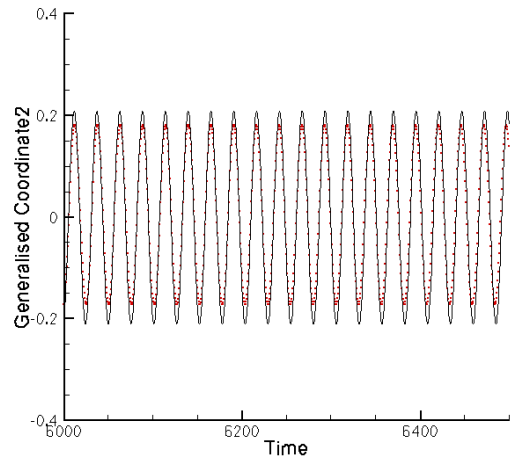
mode 1



mode 2



mode 1 - LCO region



mode 2 - LCO region

FIGURE 6.5: Comparison between the full and reduced predictions of LCO at 125% of the critical dynamic pressure for Goland wing at Mach 0.92. The symbols are from the simulation of the full system, and the lines are from the reduced model.

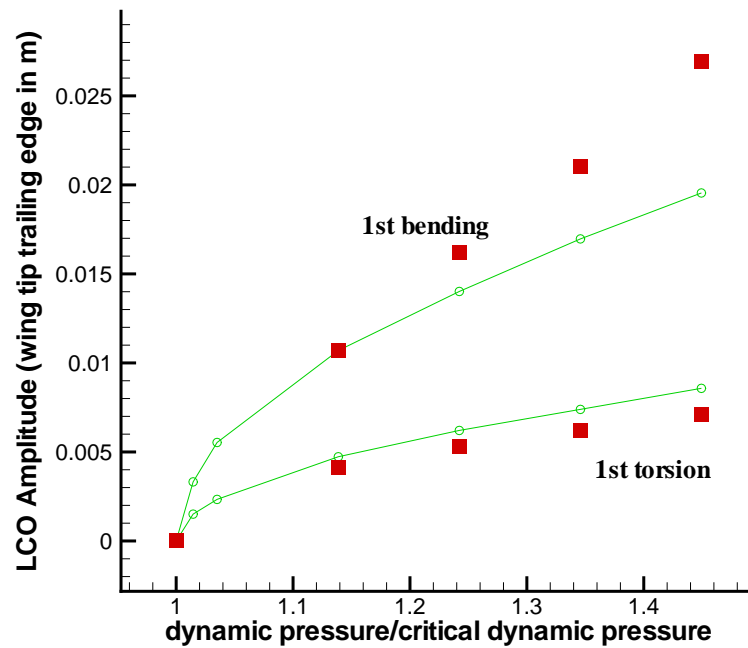


FIGURE 6.6: Growth of the LCO amplitude in the first and second modes at Mach 0.92 for the Goland wing. The filled squares are from the simulation of the full system, and the line is from the reduced model.

the bifurcation point, including limit cycle responses.

The model reduction requires the formation of matrix-vector products against the second and third Jacobians of the system. This is achieved through the use of matrix free products using extended order arithmetic.

The featured Goland wing test case showed that the 2 equation reduced order model provides very good predictions of the LCO amplitude even for very large increases in the dynamic pressure. The test case was computed on relatively coarse grids, but it was argued that the behaviour is representative for the Goland wing, and provides good test for the method.

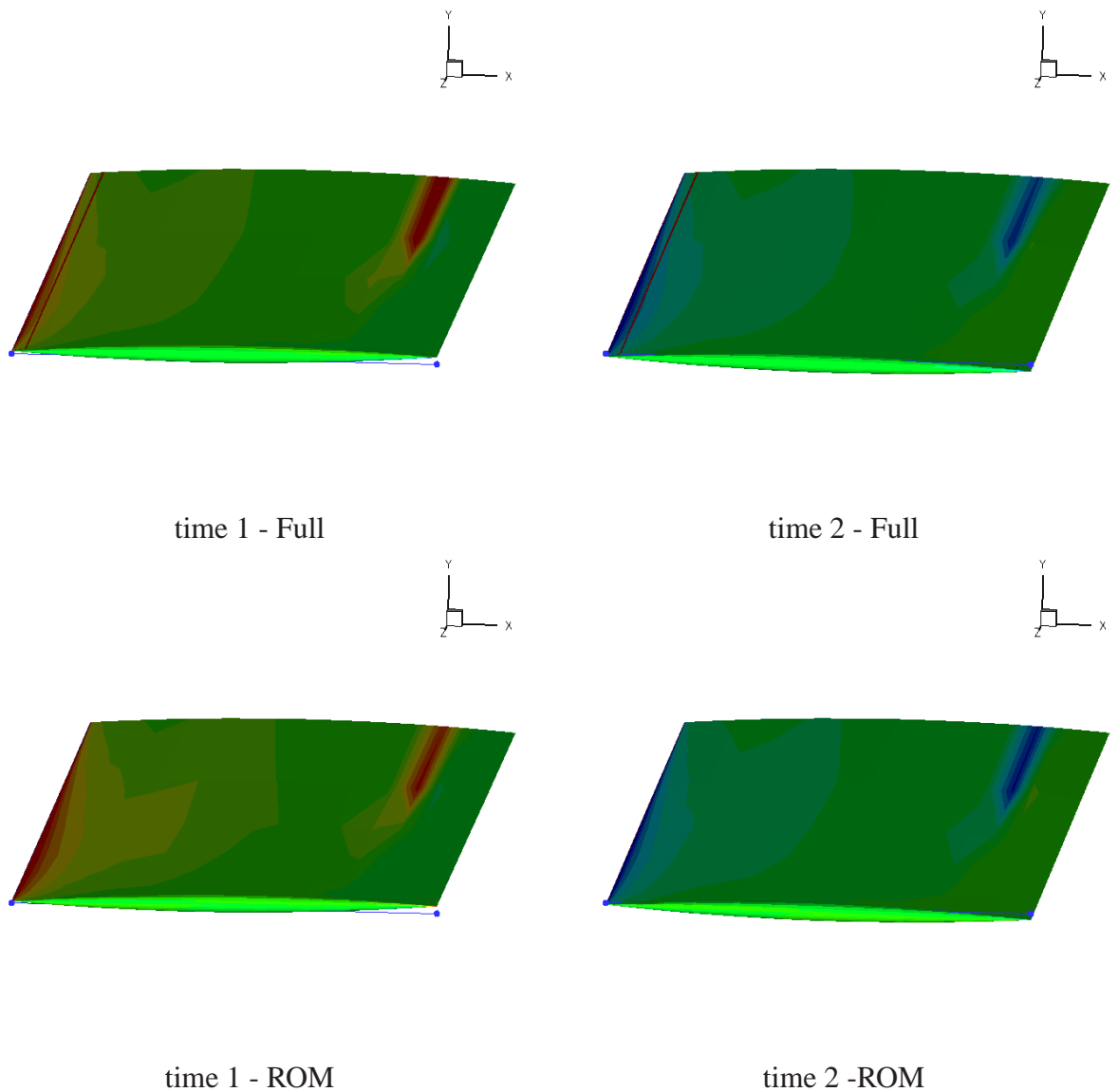


FIGURE 6.7: Response at extremes of the wing at 1.35 times the critical value of dynamic pressure using the reduced and full models. The undeflected tip position of the wing is indicated by the blue line joining 2 dots at the wing tip, and the surface contours shown are for change of pressure from the equilibrium value. These results are for the Goland wing at Mach 0.92.

Chapter 7

Conclusions

This thesis has demonstrated a number of methods for the calculation of transonic aeroelastic behaviour without having to resort to full order time domain analysis. If little is known about the instability onset the inverse power method can be used to map out the behaviour of the critical eigenvalues in the regions likely to be of interest. This information can then be used to setup an augmented system to solve for the flutter point along with information about the critical eigenvector and the frequency of the instability. In turn this information can then be used to compute a two degree of freedom model for the system dynamics around the bifurcation point, including limit cycle responses. The direct Hopf calculation is the method of choice for computing the flutter speed of a symmetric aerofoil/wing due to the decoupling of the system in equation (4.17).

A number of components were described to formulate these methods. The ability to calculate first Jacobians of the second-order spatial CFD discretisation makes it possible to use the inverse power method to compute eigenvalues and eigenvectors. The first Jacobians of the second-order spatial scheme are more ill-conditioned than the first Jacobians of the first-order spatial scheme due to the Jacobian having more off diagonal terms and hence less diagonally dominant. A robust Krylov solver was formulated to solve these sparse linear systems associated with the first Jacobian of the second-order spatial CFD discretisation. The means to calculate second and third Jacobians vector products via extended order arithmetic is crucial to the model reduction.

Starting with the method proposed by Griewank and Reddien^[71], used for aeroelastics by Morton and Beran^[85]. The use of analytical Jacobians and a Krylov

iterative solver has allowed the stability calculation to be applied in 2D and 3D. The method of projection proposed by Kuznetsov^[87] to enable model reduction for LCO calculation is unique for the full order aeroelastic application.

The methods were tested on a pitch-plunge aerofoil and three wing cases. The AGARD wing provided continuity with previous time marching work. The MDO wing exercised the inverse power method, and included the effect of a static deflection on the flutter point. The reduction in computational cost for the augmented solve of the flutter points is between one and two orders of magnitude from using unsteady time marching to find the flutter point depending on the wing used. The computational cost for computing LCOs depends on knowledge of the critical frequency. Both the damping and LCO amplitude predictions for the Goland wing provides good agreement with time-marching even when the reduced model is well above the flutter point. These represent the first 3D test results for these methods.

Future work should include the application of the methods to full aircraft test cases on fine grids as well as the inclusion of viscous terms. The major challenge for both of these steps will be forming an effective parallel preconditioned linear solver. The Jacobian matrix becomes more ill-conditioned with increasing in size of the problem as well as the addition of viscous terms. Any turbulence modelling will have to be fully coupled together for the eigenvalues of the first Jacobian matrix to be correct. The parallel implementation of a BILU preconditioner is non-trivial due to its sequential nature.^[140] This can be overcome by neglecting all terms that span processors at the expense of reducing the effectiveness of the preconditioner.

Due to the two orders of magnitude reduction in computational cost it is now possible to examine aeroelastic behaviour with respect to the uncertainty in the structure. The different flutter speeds can be computed with slight changes in the structural model to ascertain the effect of these changes on the flutter speed. It is possible to increase the number of parameters in the ROM to include these uncertainties and hence obtain a qualitative representation of the behaviour.

Creating multi-block grids for complex aircraft geometries is time consuming process. Unstructured, hybrid and polyhedral grids have all been employed to reduce the time to generate these grids. An extension of the current code to allow this functionality would allow for these complex cases to be examined more easily however the sparsity pattern of the Jacobian matrix could contain a large number of non zero blocks per row. Consider the flux between two tetrahedra which is based

on the cell centre value and its gradient. Then the stencil can have seventeen contributions to it. The addition of limiting the gradient farther increases the size of the stencil.

Bibliography

- [1] R. L. Bishlinghoff, H. Ashley, and H.L. Halfman, *Aeroelasticity*. New York: Dover Publications, 1955.
- [2] Y.C. Fung, *An Introduction to the Theory of Aeroelasticity*. John Wiley and Sons, Inc., New York, 1955.
- [3] E.H. Dowell, R. Clark, D. Cox, H. C. Curtiss Jr., J.W. Edwards, K.C. Hall, D.A. Peters, R. H. Scanlan, E. Simiu, F. Sisto, and T.W. Strganac, *A Modern Course in Aeroelasticity*. Kluwer Academic Publishers, 4th revised and enlarged edition, 2004.
- [4] M.W. Kehoe, A historical overview of flight flutter testing, Technical Report NASA Technical Memorandum 4720, NASA, 1995.
- [5] A. Collar, The first 50 years of aeroelasticity, *Aerospace*, 5(2):12–20, 1978.
- [6] I.E. Garrick and W.H. Read, Historical development of aircraft flutter, *Journal of Aircraft*, 18(11):897–912, 1981.
- [7] P.P. Friedmann, Renaissance of aeroelasticity and its future, *Journal of Aircraft*, 36(1):102–121, 1999.
- [8] K.G. Bhatia, Airplane aeroelasticity: Practice and potential, *Journal of Aircraft*, 40(6):1010–1018, 2003.
- [9] E. Livne, Future of airplane aeroelasticity, *Journal of Aircraft*, 40(6):1066–1092, 2003.
- [10] M.J. de C. Henshaw, K.J. Badcock, G.A. Vio, C.B. Allen, J. Chamberlain, I. Kaynes, G. Dimitriadis, J.E. Cooper, M.A. Woodgate, A.M. Rampurawala, D. Jones, C. Fenwick, A.L. Gaitonde, N.V. Taylor, D.S. Amor, T.A. Eccles, and C.J. Denley, Non-linear aeroelastic prediction for aircraft applications, *Progress in Aerospace Sciences*, 43:65–137, 2007.
- [11] P. Koks and J.B. Buijs, F-16 fighter aircraft flight testing in the Netherlands, Technical Report NLR-TP-2007-653, National Aerospace Laboratory, NLR, 2007.
- [12] C.M. Denegri, Limit cycle oscillation flight test results of a fighter with external stores, *Journal of Aircraft*, 37(5):761–769, 2000.

- [13] P.C. Chen, E. Sulaeman, D.D. Lui, and C.M. Denegri, Influence of external store aerodynamics on flutter/LCO of a fighter aircraft, In *43rd AIAA/ASME/ASCE/AHS/ASC Structures, Structural Dynamics, and Materials Conference*, Denver, Colorado, 22-25 April 2002. AIAA-2002-1410.
- [14] S.A. Dunn, P.A. Farrell, P.J. Budd, P.B. Arms, C.A. Hardie, and C.J. Rendo, F/A-18A flight flutter testing-limit cycle oscillation or flutter?, In *International Forum on Aeroelasticity and Structural Dynamics*, Madrid, Spain, June 2001.
- [15] E.C. Yates, Modified strip analysis method for predicting wing flutter at subsonic to hypersonic speeds, *Journal of Aircraft*, 3(1):25–29, 1966.
- [16] J. Katz and A. Plotkin, *Low Speed Aerodynamics*. Cambridge University Press, 2nd edition, 2001.
- [17] P.C. Chen, D. Sarhaddi, and D.D. Liu, Transonic-aerodynamic-influence-coefficient approach for aeroelastic and MDO applications, *Journal of Aircraft*, 37(1):85–94, 2000.
- [18] J.S. Shang, Three decades of accomplishments in computational fluid dynamics, *Progress in Aerospace Sciences*, 40(3):173–197, 2004.
- [19] R.D. Rausch, J.T. Batina, and H.T.Y. Yang, Three-dimensional time-marching aeroelastic analyses using an unstructured-grid Euler method, *AIAA Journal*, 31(9):1626–1633, 1993.
- [20] E.M. Lee-Rausch and J.T. Batina, Wing flutter boundary prediction using unsteady Euler aerodynamic method, *Journal of Aircraft*, 32(2):416–422, 1995.
- [21] E.M. Lee-Rausch and J.T. Batina, Wing flutter computations using an aerodynamic model based on the Navier-Stokes equations, *Journal of Aircraft*, 33(6):1139–1147, 1996.
- [22] F. Liu, M. Sadeghi, S. Yang, and H. Tsai, Parallel computation of wing flutter with a coupled Navier-Stokes/CSD method, In *41st Aerospace Sciences Meeting and Exhibit*, Reno, Nevada, 6-9 January 2003. AIAA-2003-1347.
- [23] C. Farhat, P. Geuzaine, and Brown. G., Application of a three-field nonlinear fluid-structure formulation to the prediction of the aeroelastic parameters of an F-16 fighter, *Computers and Fluids*, 32(1):3–29, 2003.
- [24] R. Melville, Nonlinear simulation of F-16 aeroelastic instability, In *39th Aerospace Sciences Meeting and Exhibit*, Reno, NV, 8-11 January 2001. AIAA-2001-0570.
- [25] B.H.K. Lee, Vertical tail buffeting of fighter aircraft, *Progress in Aerospace Sciences*, 36(3-4):193–279, 2000.

- [26] K. Gee, S.M. Murman, and L.B. Schiff, Computation of F/A-18 tail buffet, *Journal of Aircraft*, 33(6):1181–1189, 1996.
- [27] S.A. Morton, R.M. Cummings, and D.B Kholodar, High resolution turbulence treatment F/A-18 tail buffet, *Journal of Aircraft*, 44(6):1769–1775, 2007.
- [28] E.F. Sheta, Alleviation of vertical tail buffeting of F/A-18 aircraft, *Journal of Aircraft*, 41(2):322–330, 2004.
- [29] D.F. Fulsang, L.O. Brase, and Agrawal S., A numerical study of control surface buzz using computational fluid dynamic methods, In 10th *Applied Aerodynamics Conference*, Palo Alto, California, 22-24 June 1992. AIAA-1992-2654.
- [30] A.M. Rampurawala, *Aeroelastic analysis of aircraft with control surfaces using CFD*, PhD thesis, University of Glasgow, November 2005.
- [31] S.J. Hollowell and J. Dugundji, Aeroelastic flutter and divergence of stiffness coupled, graphite/epoxy cantilevered plates, *Journal of Aircraft*, 21(1):69–76, 1984.
- [32] A.V. Balakrishnan, Transonic small disturbance potential equation, *AIAA Journal*, 42(6):1081–1088, 2004.
- [33] A. Datta and I. Chopra, Prediction of uh-60a dynamic stall loads in high altitude level flight using CFD/CSD coupling, In *American Helicopter Society 61st Annual forum*, Grapevine, Texas, 1–3 June 2005. AIAA-1992-2654.
- [34] G.H. Parker, R.C. Maple, and P.S. Beran, Analysis of store effects on limit cycle oscillation, In 47th *AIAA/ASME/ASCE/AHS/ASC Structures, Structural Dynamics, and Materials Conference*, Newport, Rhode Island, 1- 4 May 2006. AIAA-2006-1846.
- [35] G.H. Parker, R.C. Maple, and P.S. Beran, Computational aeroelastic analysis of store-induced limit-cycle oscillation, *Journal of Aircraft*, 44(1):48–59, 2007.
- [36] K.J. Badcock, B.E. Richards, and M.A. Woodgate, Elements of computational fluid dynamics on block structured grids using implicit solvers, *Progress in Aerospace Sciences*, 36:351–392, 2000.
- [37] H.M. Tsai, A. S. F. Wong, J. Cai, Y. Zhu, and F. Liu, Unsteady flow calculations with a parallel multiblock moving mesh algorithm, *AIAA Journal*, 39(6):1021–1029, 2001.
- [38] M. Lesoinne and C Farhat, High order subiteration-free staggered algorithm for nonlinear transient aeroelastic problems, *AIAA Journal*, 36(9):1754–1757, 1998.

- [39] C. Farhat and M. Lesoinne, Two efficient staggered algorithms for the serial and parallel solution of three-dimensional nonlinear transient aeroelastic problems, *Computer Methods in Applied Mechanics and Engineering*, 182(3-4):499–515, 2000.
- [40] S.A Brown, Displacement extrapolation for CFD and CSM analysis, In 38th AIAA/ASME/ASCE/AHS/ASC Structures, Structural Dynamics, and Materials Conference and Exhibit, Kissimmee, FL, 7-10 April 1997. AIAA-1997-1090.
- [41] G.S.L. Goura, K.J. Badcock, M.A. Woodgate, and B.E. Richards, A data-exchange method for fluid-structure interaction problems, *Aeronautical Journal*, 105:215–221, 2001.
- [42] K.J. Badcock, M.A. Woodgate, and B.E. Richards, Direct aeroelastic bifurcation analysis of a symmetric wing based on the Euler equations, *Journal of Aircraft*, 42(3):731–737, 2005.
- [43] M.A. Woodgate, K.J. Badcock, A.M. Rampurawala, B.E. Richards, D. Nardini, and M.J. Henshaw, Aeroelastic calculations for the Hawk aircraft using the Euler equations, *Journal of Aircraft*, 42(4):1005–1012, 2005.
- [44] E.H. Dowell and K.C. Hall, Modeling of fluid-structure interaction, *Annual Review of Fluid Mechanics*, 33:445–490, 2001.
- [45] D.J. Lucia, P.S. Beran, and W.A. Silva, Reduced-order modeling: New approaches for computational physics, *Progress in Aerospace Sciences*, 40:51–117, 2004.
- [46] K.C. Hall, Eigenanalysis of unsteady flows about airfoils, cascades, and wings, *AIAA Journal*, 32(12):2426–2432, 1994.
- [47] E.H. Dowell, Eigenmode analysis in unsteady aerodynamics: Reduced order models, *AIAA Journal*, 34(8):1578–1583, 1996.
- [48] M.C. Romanowski and E.H. Dowell, Reduced order Euler equations for unsteady aerodynamic flows: numerical techniques, In 34th Aerospace Sciences Meeting and Exhibit, Reno, NV, 15-18 January 1996. AIAA-1996-528.
- [49] G.H. Golub and C.F. Van Loan, *Matrix Computations*. The John Hopkins University Press, 3rd edition, 1996.
- [50] H. Shahverdi, A.S. Nobari, M. Behbahani-Nejad, and H. Haddadpour, An efficient reduced-order modelling approach based on fluid eigenmodes and boundary element method, *Journal of Fluids and Structures*, 23(1):143–153, 2007.
- [51] P. Holmes, J.L. Lumley, and G. Berkooz, *Turbulence, Coherent Structures, Dynamical Systems and Symmetry*. Cambridge University Press, new edition, 1998.

- [52] M.C. Romanowski, Reduced order unsteady aerodynamic and aeroelastic models using Karhunen-Loeve eigenmodes, In *6th NASA/ISSMO Symposium on Multidisciplinary Analysis and Optimization*, Bellevue, WA, 4-6 September 1996. AIAA-1996-3981.
- [53] M.S. Hong, K.G. Bhatia, G. SenGupta, T. Kim, W.A. Silva, R.E. Bartels, and R.T. Biedron, Simulations of a twin-engine transport flutter model in the transonic dynamics tunnel, In *International Forum on Aeroelasticity and Structural Dynamics*, Amsterdam, 4-6 June 2003. Paper 2003-US-44.
- [54] T. Lieu, C. Farhat, and M. Lesoinne, Reduced-order fluid/structure modeling of a complete aircraft configuration, *Computer Methods in Applied Mechanics and Engineering*, 195(41-43):5730–5742, 2006.
- [55] B.I. Epureanu, A parametric analysis of reduced order models of viscous flows in turbomachinery, *Journal of Fluids and Structures*, 17(7):971–982, 2003.
- [56] R.F. Schmit and M.N. Glauser, Improvements in low dimensional tools for flow-structure interaction problems: Using global POD, In *42nd AIAA Aerospace Sciences Meeting and Exhibit*, Reno, NV, 5-8 January 2004. AIAA-2004-0889.
- [57] T. Lieu and M Lesoinne, Parameter adaptation of reduced order models for three-dimensional flutter analysis, In *42nd AIAA Aerospace Sciences Meeting and Exhibit*, Reno, NV, 5-8 January 2004. AIAA-2004-0888.
- [58] T. Lieu and C. Farhat, Adapation of aeroelastic reduced-order models and application to an F-16 configuration, *AIAA Journal*, 45(6):1244–1257, 2007.
- [59] D. Amsallem and C. Farhat, Interpolation method for adapting reduced-order models and application to aeroelasticity, *AIAA Journal*, 46(7):1803–1813, 2008.
- [60] K.C. Hall, J.P. Thomas, and W.S. Clark, Computation of unsteady nonlinear flows in cascades using a harmonic balance technique, *AIAA Journal*, 40(5):879–886, 2002.
- [61] J.P. Thomas, E.H. Dowell, K.C. Hall, and C.M. Denegri Jr., Further investigation of modeling limit cycle oscillation behavior of the F-16 fighter using a harmonic balance approach, In *46th AIAA/ASME/ASCE/AHS/ASC Structures, Structural Dynamics and Materials Conference*, Austin, Texas, 18-21 April 2005. AIAA-2005-1917.
- [62] M. McMullen, A. Jameson, and J.J. Alonso, Application of a non-linear frequency domain solver to the Euler and Navier-Stokes equations, In *40th Aerospace Sciences Meeting and Exhibit*, Reno, NV, 14-17 January 2002. AIAA-2002-0120.

- [63] M. McMullen, A. Jameson, and J.J. Alonso, Demonstration of nonlinear frequency domain methods, *AIAA Journal*, 44(7):1428–1435, 2006.
- [64] L. Liu, J.P. Thomas, E.H. Dowell, P. Attar, and K.C. Hall, A comparison of classical and high dimensional harmonic balance approaches for a Duffing oscillator, *Journal of Computational Physics*, 215(1):298–320, 2006.
- [65] R.C. Maple, P.I. King, P.D. Orkwis, and J.M. Wolff, Adaptive harmonic balance method for nonlinear time-periodic flows, *Journal of Computational Physics*, 193(2):620–641, 2004.
- [66] R.C. Maple, P.I. King, and M.E Oxley, Adaptive harmonic balance solutions to Euler’s equation, *AIAA Journal*, 41(9):1705–1714, 2003.
- [67] P.S. Beran, N.S. Knot, F.E. Eastep, R.D. Synder, and J.V. Zweber, Numerical analysis of store-induced limit cycle oscillation, *Journal of Aircraft*, 41(6):1315–1326, 2004.
- [68] R. U. Seydel, *Practical Bifurcation Analysis and Stability Analysis: From Equilibrium to Chaos*. Springer-Verlag, 2nd edition, 1994.
- [69] E.J. Doedel, Auto: A program for the automatic bifurcation analysis of autonomous systems, *Congressus Numerantium*, 30:265–284, 1981.
- [70] D. Roose, An algorithm for the computation of hopf bifurcation points in comparison with other methods, *Journal of Computational and Applied Mathematics*, 12:517–529, 1985.
- [71] A. Griewank and G. Reddien, The calculation of hopf points by a direct method, *IMA Journal of Numerical Analysis*, 3:295–303, 1983.
- [72] M. Holodniok and M. Kubiček, New algorithms for the evaluation of complex bifurcation points in ordinary differential equations. a comparative numerical study, *Applied Mathematics and Computation*, 15:261–274, 1984.
- [73] J. Carr, *Applications of centre manifold theory*, volume 35 of *Applied Mathematical Sciences*. Springer-Verlag, 1981.
- [74] N. Sidorov, B. Loginov, A. Sinitsyn, and M. Falaleev, *Lyapunov-Schmidt Methods in Nonlinear Analysis and Applications*. Kluwer Academic Publishers, 2002.
- [75] A.H. Nayfeh, *Perturbation Methods*. Wiley-Interscience, New York, 1973.
- [76] J. Kevorkian and J.D. Cole, *Multiple Scale and Singular Perturbation Methods*, volume 114 of *Applied Mathematical Sciences*. Springer-Verlag, 1996.
- [77] A.H. Nayfeh and B. Balachandran, *Applied nonlinear dynamics: Analytical, computational, and Experimental Methods*. John Wiley and Sons, Inc., New York, 1995.

- [78] D. Dessi and F. Mastroddi, Limit-cycle stability reversal via singular perturbation and wing-flap flutter, *Journal of Fluids and Structures*, 19(6):765–783, 2004.
- [79] G. Vio, G.A. Dimitriadis and J.E. Cooper, Bifurcation analysis and limit cycle oscillation amplitude prediction methods applied to the aeroelastic galloping problem, *Journal of Fluids and Structures*, 23(7):983–1011, 2007.
- [80] F. Verhulst, *Nonlinear Differential Equations and Dynamical Systems*. Springer, Berlin, 2nd edition, 1996.
- [81] A.Y.T. Leung and Q.C. Zhang, Higher order normal form and period averaging, *Journal of Sound and Vibration*, 217(5):795–806, 1998.
- [82] E.L. Allgower and K. Georg, *Numerical Continuation Methods: An Introduction*. Springer, New York, 1990.
- [83] H. Hamura, Y. Tsuda, and A. Sueoka, Higher approximation of steady oscillations in nonlinear systems with single degree of freedom, *Bulletin of the JSME*, 24(195):1616–1625, 1981.
- [84] P.S. Beran and S.A. Morton, Continuation method for the calculation of transonic airfoil flutter boundaries, *Journal of Guidance, Control and Dynamics*, 20(6):1165–1171, 1997.
- [85] S.A. Morton and P.S. Beran, Hopf-bifurcation analysis of airfoil flutter at transonic speeds, *Journal of Aircraft*, 36(2):421–429, 1999.
- [86] J. Anderson, Identification of hereditary aeroelastic behaviour by generic modelling, Technical Report Aerospace Engineering report 9422, University of Glasgow, 1994.
- [87] Y.A. Kuknetsov, *Elements of Applied Bifurcation Theory*, volume 112 of *Applied Mathematical Sciences*. Springer, 3rd edition, 2004.
- [88] V. Gattulli, F. Di Fabio, and A. Luongo, Simple and double hopf bifurcations in aeroelastic oscillators with tuned mass dampers, *Journal of the Franklin Institute*, 338(2-3):187–201, 2001.
- [89] K. Badcock, M. Woodgate, F. Cantariti, and B. Richards, Solution of the unsteady Euler equations in three dimensions using a fully unfactored method, In *38th Aerospace Sciences Meeting and Exhibit*, Reno, NV, 10-13 January 2000. AIAA-2000-0919.
- [90] J.F. Epperson, *An introduction to numerical methods and analysis*. John Wiley and Sons, Inc., New York, 2002.
- [91] C.G. Broyden, A class of methods for solving nonlinear simultaneous equations, *Mathematics of Computation*, 19(92):577–593, 1965.

- [92] C.G. Broyden, J.E. Dennis, and J.J. Moré, On the local and superlinear convergence of quasi-newton methods, *IMA Journal of Applied Mathematics*, 12(3):223–245, 1973.
- [93] J.E. Marsden and M. McCracken, *The Hopf Bifurcation and its Applications*, volume 19 of *Applied Mathematical Sciences*. Springer, 1976.
- [94] B.D. Hassard, N.D. Kazarinoff, and Y.H. Wan, *Theory and applications of Hopf bifurcation*. Cambridge University Press, Cambridge, Massachusetts, 1981.
- [95] R.F. Heinemann and A.B. Poore, Multiplicity, stability, and oscillatory dynamics of the tubular reactor, *Chemical Engineering Science*, 36(8):1411–1419, 1981.
- [96] E.L. Ortiz, Step by step tau method: Part I piecewise polynomial approximations, *Computers and Mathematics with Applications*, 1:381–392, 1975.
- [97] P.S. Beran and C.D. Carlson, Domain-decomposition methods for bifurcation analysis, In *35th Aerospace Sciences Meeting and Exhibit*, Reno, NV, 6-9 January 1997. AIAA-1997-0518.
- [98] A.Y.T. Leung and T. Ge, An algorithm for higher order Hopf normal forms, *Shock and Vibration*, 2(4):307–319, 1995.
- [99] Y.A. Kuznetsov, Numerical normalization techniques for all codim 2 bifurcations of equilibria in ODEs, *SIAM Journal of Numerical Analysis*, 36(4):1104–1124, 1999.
- [100] P. Couillet and E. Spiegel, Amplitude equations for systems with competing instabilities, *SIAM Journal of Applied Mathematics*, 43(4):776–821, 1983.
- [101] A.H. Nayfeh, *Method of Normal Forms*. Wiley-Interscience, New York, 1993.
- [102] H. Blasius, Grenzsichten in Flüssigkeiten mit kleiner Reibung, *Zeitschrift für Mathematik und Physik*, 56:1–37, 1908. English translation in NACA-TM-1256 (1950).
- [103] C. Chicone, *Ordinary Differential Equations with Applications*, volume 34 of *Texts in Applied Mathematics*. Springer, 2nd edition, 2006.
- [104] A.N. Shoshitaishvili, Bifurcations of topological type of a vector field near a singular point, In *Proceedings of Petrovskii Seminar, Vol 1*, pages 279–309, Moscow State University, Moscow, 1975.
- [105] L. Reiziņš, Local topological equivalence of systems of differential equations, *Differential Equations*, 4:99–107, 1968.
- [106] K.J. Palmer, Topological equivalence and the hopf bifurcation, *Journal of Mathematical Analysis and Applications*, 66(3):586–598, 1978.

- [107] L. Kantorovich and G. Akilov, *Functional Analysis in normed spaces*. Macmillan, New York, 1964.
- [108] P.S. Beran, A domain-decomposition method for airfoil flutter analysis, In *36th Aerospace Sciences Meeting and Exhibit*, Reno, NV, 12-15 January 1998. AIAA-1998-0098.
- [109] J.L. Steger, Implicit finite-difference simulation of flow about arbitrary two-dimensional geometries, *AIAA Journal*, 16(7):679–686, 1978.
- [110] S. Osher and S.R. Chakravarthy, Upwind schemes and boundary conditions with applications to Euler equations in general coordinates, *Journal Computational Physics*, 50:447–481, 1983.
- [111] B. Van Leer, Towards the ultimate conservative conservative difference scheme II: Monotonicity and conservation combined in a second order scheme, *Journal Computational Physics*, 14:361–374, 1974.
- [112] A. Jameson, Time dependent calculations using multigrid, with applications to unsteady flows past airfoils and wings, In *10th Computational Fluid Dynamics Conference*, Honolulu, HI, 24-26 June 1991. AIAA-1991-1596.
- [113] G.S.L. Goura, K.J. Badcock, M.A. Woodgate, and B.E. Richards, Implicit analysis for the time marching analysis of flutter, *Aeronautical Journal*, 105:199–214, 2001.
- [114] C. Bischof, A. Carle, G. Corliss, A. Griewank, and P. Hovland, ADIFOR: Generating derivative codes from fortran programs, *Scientific Programming*, 1(1):11–29, 1992.
- [115] A. Griewank, *Evaluating Derivatives: Principles and Techniques of Algorithmic Differentiation*, volume 19 of *Frontiers in Applied Mathematics*. SIAM, 2000.
- [116] K.J. Badcock, X. Xu, L. Dubuc, and B.E. Richards, Preconditioners for high speed flows in aerospace engineering, In *Numerical Methods for Fluid Dynamics V*, pages 287–294. Oxford University Press, 1996.
- [117] O. Axelsson, *Iterative Solution Methods*. Cambridge University Press, 1994.
- [118] R.S. Tuminaro, M. Heroux, S.A. Hutchinson, and J.N. Shahid, *Official Aztec User's Guide Version 2.1*, Sandia Laboratory, 1999, SAND99-8801J.
- [119] R.L. Burden and J.D. Faires, *Numerical Analysis*. Brooks Cole, 7th edition, 2000.
- [120] E.C. Yates, AGARD standard aeroelastic configurations for dynamic response I: Wing 445.6, Technical Report AGARD Report 765, North Atlantic Treaty Organization, 1988.

- [121] T.H. Pulliam and J.L. Steger, Implicit finite-difference simulations of three-dimensional compressible flow, *AIAA Journal*, 18(2):159–167, 1980.
- [122] G.S.L. Goura, *Time Marching Analysis of Flutter using Computational Fluid Dynamics*, PhD thesis, University of Glasgow, November 2001.
- [123] G.S.L. Goura, K.J. Badcock, M.A. Woodgate, and B.E. Richards, Extrapolation effects on coupled CFD-CSD simulations, *AIAA Journal*, 41(2):312–314, 2003.
- [124] W.J. Gordon and C.A. Hall, Construction of curvilinear coordinate systems and applications to mesh generation, *International Journal for Numerical Methods in Engineering*, 7(4):461–477, 1973.
- [125] R.E. Gordnier and R.B. Melville, Transonic flutter simulations using an implicit aeroelastic solver, *Journal of Aircraft*, 37(5):872–879, 2000.
- [126] S.C. Eisenstat, H.C. Elman, and M. Schultz, Variational iterative methods for nonsymmetric systems of linear equations, *SIAM Journal of Numerical Analysis*, 20(2):345–357, 1983.
- [127] A. Chapman and Y. Saad, Deflated and augmented Krylov subspace techniques, *Numerical Linear Algebra with Applications*, 4(1):43–66, 1997.
- [128] P. Girodroux-Lavigne, J. P. Grisval, S. Guillemot, M. Henshaw, A. Karlsson, V. Selmin, J. Smith, E. Teupootahiti, and B. Winzell, Comparative study of advanced fluid-structure interaction methods in the case of a highly flexible wing(results from the unsi program), In *International Forum aeroelasticity and structural dynamics*, Madrid, Spain, June 2001.
- [129] N.V. Taylor, C.B. Allen, A.L. Gaitonde, D.P. Jones, G.A. Vio, J.E. Cooper, A.M. Rampurawala, K.J. Badcock, M.A. Woodgate, and M.J. de C. Henshaw, Aeroelastic analysis through linear and non-linear methods: a summary of flutter prediction in the PUMA DARP, *Aeronautical Journal*, 110(1107):333–343, 2006.
- [130] C.M. Denegri, J.A. Dubben, and D.L. Maxwell, In-flight wing deformation characteristics during limit cycle oscillations, *Journal of Aircraft*, 42(2):500–508, 2005.
- [131] J.P. Thomas, E.H. Dowell, K.C. Hall, and C.M. Denegri, An investigation of the sensitivity of F-16 fighter flutter onset and limit cycle oscillations to uncertainties, In *47th AIAA/ASME/ASCE/AHS/ASC Structures, Structural Dynamics, and Materials Conference*, Newport, Rhode Island, 1 - 4 May 2006. AIAA-2006-1847.
- [132] D.R. Dreim, S.B. Jacobsen, and R.T. Britt, Simulation of non-linear transonic aeroelastic behaviour on the B2, In *CEAS/AIAA/ICASE/NASA Langley International Forum on in Aeroelasticity and Structural Dynamics*, pages 511–521, Williamsburg, VA, 22-25 June 1999. NASA/CP-1999-209136.

- [133] B.B. Pranata, J.C. Kok, S.P. Spekreijse, M.H.L. Hounjet, and J.J. Meijer, Simulation of limit cycle oscillation of fighter aircraft at moderate angle of attack, In *CEAS/AIAA/ICASE/NASA Langley International Forum on in Aeroelasticity and Structural Dynamics*, Amsterdam, 4-6 June 2003.
- [134] J.P. Thomas, E.H. Dowell, and K.C. Hall, Three-dimensional transonic aeroelasticity using proper orthogonal decomposition-based reduced-order models, *Journal of Aircraft*, 40(3):544–551, 2003.
- [135] D. Lucia, P.S. Beran, and W. Silva, Aeroelastic system development using proper orthogonal decomposition and volterra theory, In *44th AIAA/ASME/ASCE/AHS/ASC Structures, Structural Dynamics, and Materials Conference*, Norfolk, Virginia, 7-10 April 2003. AIAA-2003-1922.
- [136] P.K. Jain, O.P. Ahuja, and K Ahmed, *Functional Analysis*. Wiley-Interscience, 1996.
- [137] Y. Hida, X.S. Li, and D.H Bailey, *Library for Double-Double and Quad-Double Arithmetic*, Lawrence Berkeley National Laboratory, 2008, crd.lbl.gov/dhbailey/mpdist/index.html.
- [138] R.D. Synder, J.N. Scott, N.S. Knot, P.S. Beran, and J.V. Zweber, Predictions of store-induced limit cycle oscillations using Euler and Navier-Stokes fluid dynamics, In *44th AIAA/ASME/ASCE/AHS/ASC Structures, Structural Dynamics, and Materials Conference*, Norfolk, Virginia, 7 - 10 April 2003. AIAA-2003-1727.
- [139] N.S. Knot, P.S. Beran, J.V. Zweber, and F.E. Eatsep, Influence of tip store mass location on wing limit-cycle oscillation, In *44th AIAA/ASME/ASCE/AHS/ASC Structures, Structural Dynamics, and Materials Conference*, Norfolk, Virginia, 7 - 10 April 2003. AIAA-2003-1731.
- [140] I.S. Duff and H.A. van der Vorst, Developments and trends in the parallel solution of linear systems, *Parallel Computing*, 25:1931–1970, 1999.